Identifizierung, Genkartierung, und Charakterisierung von ENU-induzierten mutanten Mauslinien für Knochenkrankheiten des Menschen

Von der Fakultät Geo- und Biowissenschaften
der Universität Stuttgart zur Erlangung der Würde
eines Doktors Naturwissenschaften
(Dr. rer. nat.)

vorgelegt von
Thomas Stephen Lisse
aus New York City, NY USA

Vorsitzender des Prüfungsausschusses: Prof. Dr. G. Sprenger
Hauptberichter: Prof. Dr. K. Pfizenmaier
Mitberichter: Prof. Dr. M. Hrabé de Angelis (Neuherberg)

Tag der mündlichen Prüfung: 6. März 2008

Institut für Zellbiologie und Immunologie
Universität Stuttgart

2007

Ich erkläre hiermit an Eides statt, dass ich die vorliegende Arbeit selbständig ohne unzulässige fremde Hilfe angefertigt habe.

Die verwendeten Literaturquellen sind im Literaturverzeichnis vollständig zitiert.

München, den 04, Juli 2007

_____

Thomas Lisse

Table of Content

For Amanda, Cordrey, Norman,

Kathy and Karen

I   Rationale: Aim of the research

Ziel dieser Doktorarbeit war es, zwei ENU-induzierte Mausmodelle für Bindegewebserkrankungen im Menschen zu untersuchen. Zur Charakterisierung der beiden Mausmodelle wurden zuerst die dem jeweiligen Phänotyp zugrunde liegenden Gene genetisch kartiert und anschließend positionell kloniert. Weiterhin wurden systemische Untersuchungen, sowie Analysen der Knochen- und Knorpelphänotypen durchgeführt, wozu spezifische Methoden entwickelt wurden.

Die Ergebnisse dieser Doktorarbeit sollen neue Fragestellungen aus genetischer, klinischer und biologischer Sicht erwecken. Die neu aufgeworfenen Fragen und Interpretationen dieser Arbeit werden weiterhin nicht nur für die beiden untersuchten Krankheitsmodelle von Bedeutung sein, sondern darüber hinaus auch auf andere regulatorische Signalwege im Organismus übertragbar sein. Obwohl bisher große Fortschritte im Hinblick auf die Identifizierung von genetischen Faktoren gemacht wurden, die Knochenskelettfehlbildungen zugrunde liegen, sind trotz alledem viele Gene sowie deren Funktionen noch nicht untersucht worden und hoffen daher auf baldige Aufklärung.

Genes affecting skeletal development and physiology in mouse and human has lead to our interest and potential to generate genetically modified mice which has profoundly transformed our knowledge of the mechanisms regulating skeletal biology (1). The skeletal system is complex and vital to life because it plays an essential role in mineral homeostasis, maintains hematopoietic elements, provides mechanical support for development, breathing and locomotion, protects organs, and determines features of body composition (2).

Since the time of Grüneberg, i.e. a period in which the underlying molecular mechanisms and causal genetic relations of systemic and local disorders of the skeleton remained unknown, much progress has been made in experimental genetics and skeletal biology (3). The identification of genes in mouse involved in genetic diseases is no longer the challenge of those who once made careers of not finding a gene. For example, despite its discovery in 1927 as a mutant mouse strain with a short blunted tail, the mouse *T* (Brachyury) locus was largely implicated during nascent mesoderm development and notochord differentiation only from an inheritance and anatomical point of view until it was finally positionally cloned over 60 years later (4). Major advancements have only recently been made (i.e. 80 years after its first report) about how the T box product selects and regulates its

downstream targets (4-9). Developments from the human and mouse genome initiatives have vastly facilitated the process of localizing segregating mutations, obtaining the physical regents necessary for characterizing the candidate region, and making phenotype-genotype associations in the search for candidate genes involved in the disease of interest. The search for genes that control susceptibility towards multifactorial and debilitating skeletal disorders such as osteoporosis, which is responsible for millions of fractures annually and affects an estimated 30 % of women and 12 % of men over the age of 50 worldwide, is ongoing (10). The search entails systematic genetic approaches in Man and animal models such as twin studies, meta and quantitative trait loci (QTL) analyses of genetic associations, and mutagenesis screens in identifying the causal defects in bone matrix components and degradative enzymes, hormones and receptors, cytokines, osteoblast regulatory factors, osteoclastogenesis and musculoskeletal development.

The objective of this doctoral research project was the continued identification and elucidation of the genes and underlying molecular-pathogenetic disease mechanisms, respectively, of two mouse models for human connective tissue disorders using the forward-genetic approach of *N*-ethyl-*N*-nitrosourea (ENU) chemical mutagenesis within a few years time. This entailed the rapid cloning of the causative mutations via genetic linkage analysis, characterization of the bone, cartilage and syndromic phenotypes, and development of the bone/cartilage-related methodologies necessary for analysis of the uncharacterized mutant mouse lines. Ideally, the expectations were to investigate the functions of novel skeletal genes, although the ENU strategy is largely based on random variation in the choice of target genes, yet apt in affecting crucial processes and functional domains of known genes, transcripts and proteins all causative for unique and unforeseen skeletal phenotypes. The results obtained from this project hope to raise important questions concerning the determinants of functional diversity from the mutational, genetic, clinical and biological points of views of the disease models. Furthermore, the questions and interpretations are relevant not only to the classes of mutated molecules reported here within, but also to other groups of critical factors known to reside within cognate regulatory networks. Although there has been extensive progress in identifying the genetic factors which regulate susceptibility to skeletal disorders, most of the determinants and molecular mechanisms which regulate skeletogenesis and homeostasis remain to be discovered.

Scientist G. Karsenty wrote, "Probably no other organ in vertebrate biology has benefited as much from our ability to generate, at will, mutant mouse strains." (1) The organ

spoken of was the skeleton, and admittedly, the work presented in this dissertation was a reductive response to one of humanity's destinies.

T.S.L

GSF, München-Neuherberg

Universität Stuttgart

2007

II	Abstracts

INTRACELLULAR ACCUMULATION OF ABNORMAL PRO-α1(I) CAUSES ER STRESS AND OSTEOBLAST APOPTOSIS IN A NEW MOUSE MODEL FOR TYPE II/III/IV OSTEOGENESIS IMPERFECTA

Osteogenesis imperfecta is an inherited disorder characterized by increased bone fragility, fractures and osteoporosis, and most cases are caused by mutations affecting the type I collagen genes. Here we describe a new mouse model for osteogenesis imperfecta termed *Aga2* (<u>a</u>bnormal <u>ga</u>it 2) which was isolated from the Munich N-ethyl-N-nitrosourea mutagenesis program and exhibited phenotypic variability including reduced bone mass, multiple fractures and early lethality. The causal gene was mapped to chromosome 11 by linkage analysis, and a C-terminal frameshift mutation was identified in the *Col1a1* (procollagen type I, alpha 1) gene as the cause of the disorder. Heterozygous animals had markedly increased bone turnover and a disrupted native collagen network associated with microfractures *in vivo*. Further studies showed that abnormal pro-α1(I) chains accumulated intracellularly in *Aga2*/+ dermal fibroblasts and were poorly secreted extracellularly. This was associated with the induction of an ER stress-specific unfolded protein response (UPR) involving upregulation of BiP, Hsp47 and Gadd153 with caspases 12 and 3 activation and apoptosis of osteoblasts both *in vitro* and *in vivo*. These studies resulted in the identification of a new model for osteogenesis imperfecta, and identified a role for intracellular modulation of the ER stress-associated UPR machinery towards osteoblast apoptosis during the pathogenesis of disease.

CHARACTERIZATION AND MAPPING OF *ALI34*: A ENU-DERIVED MURINE MODEL DEPICTING FEATURES OF OSTEOARTHRITIS AND OSTEOCHONDRODYSPLASIA

The Munich *N*-ethyl-*N*-nitrosourea (ENU) mutagenesis program was recently utilized to identify and characterize new genes and alleles that regulate skeletal development and homeostasis in mouse. Subsequently, the *Ali34* autosomal dominant mutant line was isolated depicting several features of osteoarthritis (OA) and osteochondrodysplasia. OA is the most common type of arthritis affecting up to 30 % of people over age 55. *Ali34*/+ and *Ali34*/*Ali34* skeletal phenotypes were characterized, and the genetic mapping of the *Ali34* locus was reported. Skeletal morphology was assessed via μCT and alizarin red/alcian blue staining. Dynamic histomorphometry was performed via tetracycline/calcin double-labeling. Proteoglycans were assessed using safranin O. Chondromodulin I (ChM-I), an inhibitor of angiogenesis marker, was detected via immunohistochemistry. Bone and body composition parameters were measured via pDXA and pQCT. Linkage analysis was conducted via the outcross-backcross (F_1 X P) breeding strategy utilizing a high throughput SNP haplotyping platform. 12-week-old *Ali34*/+ animals exhibit shortened tibiae and femora, and anklyosis and osteophytes affecting the knee joint region. Both periarticular and epiphysial bones displayed subchondral sclerosis, and mineral components were evident within the articular space. A decrease in the rate of new trabecular bone formation was accompanied by a ~13 % reduction in vBMD (295.4 ± 15.4 mg/cm^3 control [$n = 10$] and 258.3 ± 30.5 mg/cm^3 *Ali34*/+ [$n = 8$]; $p = 0.001$) at the femoral metaphysis. Abnormalities of the growth plate were apparent as absence of the resting zone of chondrocytes, and disorganization of the avascular zone as shown by ChM-I reactivity. In *Ali34* articular cartilage, the transitional zone was absent, and erosion of matrix was evident without fibrillation. The articular capsule contained increased mesenchyme cells, and tendon metaplasia was obvious. pDXA results depicted increased lean mass (~21 %, $p = 0.001$, $n = 6$) and lowered fat mass (~37.5 %, $p = 0.001$, $n = 6$) in *Ali34* males. *Ali34*/*Ali34* animals died embryonically between E16 - 19, and displayed both caudal calvarial agenesis and deviated vertebral disks. Chromosomal mapping studies revealed *Ali34* linkage on mouse chromosome 6, and subsequently fine mapping and candidate gene sequencing investigations identified a mutation in the *Plxnd1* (plexin D1) gene crucial for vasculogenesis and angiogenesis maintenance. Our observations demonstrated that the *Ali3 4* locus played a key role in regulating the development of the epiphysial growth plate and knee joints, and proper development of skeletal elements derived from the (paraxial) mesoderm and neural crest . Lastly, based on the *Ali34* phenotype and causal gene product, the hereditary

congenital facial paresis (HCFP; OMIM 601471) susceptibility locus may reflect anomalies in the plexin family of genes. The *Ali34* line represents a valuable animal model with which to investigate the (early) pathogenesis of OA and osteochondrodysplasia.

III   Abbreviations

Aga2	Abnormal gait 2	MS	Microsatellite
Ali34	Abnormal limb 34	MSC	Mesenchyme stem cell
ALP	Alkaline phosphatase	OA	Osteoarthritis
ANCOVA	Analysis of co-variance	OB	Osteoblast
ANOVA	Analysis of variance	OC	Osteoclast
BFR	Bone formation rate	OI	Osteogenesis imperfecta
BMC	Bone mineral content	Oim	Osteogenesis imperfecta
BMD	Bone mineral density		murine
BMP	Bone morphogenic protein	OMIM	Online Mendelian
BW	Body weight		inheritance in Man
C	COOH (carboxyl)	PCD	Programmed cell death
CSF-1	macrophage colony-	pQCT	Peripheral quantitative
	stimulating factor 1		computed tomography
Df	Degree of freedom	PTH	Parathyroid hormone
DXA	Dual energy X-ray	PTHrP	Parathyroid hormone-related
	absorptiometry		peptide
ECG	Electrocardiogram	RANKL	ligand to receptor activator
ECM	Extracellular matrix		of NFκB
ENU	*N*-ethyl-*N*-nitrosourea	s.c.	subcutaneous
ER	Endoplasmic reticulum	SEM	Scanning electron
ERSS	ER stress signaling		microscopy
GAG	Glycosaminoglycan	SNP	Single nucleotide
GMC	German Mouse Clinic		polymorphism
GSF	GSF National Research	TEM	Transmission electron
	Center		microscopy
HAP	Hydroxyapatite	TGFß	Transforming growth factor
i.p.	interperitoneal		beta
LM	Littermate	TRAP	Tartrate-resistant acid
MAR	Mineral apposition rate		phosphatase
MGI	Mouse Genome Informatics	UPR	Unfolded protein response
MIM	Mendelian inheritance in	VEGF	Vascular endothelial growth
	Man		factor

Figures

Tables

V   Acknowledgments

1.   Introduction

1.1   Skeletal development and morphogenesis

The vertebrate skeleton evolves from three embryonic cellular lineages (Fig. 1). Neural crest cells give rise to the craniofacial skeleton (parts of the skull, brachial arch), and cells from the paraxial mesoderm and the lateral plate mesoderm develop the axial (somites, and caudal parts of the skull) and limb (bud) skeleton respectively (11, 12). Mesenchyme stem cells (MSCs) have the potential to initiate osteogenesis, chondrogenesis, tendogenesis/ligamentagenesis, myogenesis, marrow stromagenesis, adipogenesis, and dermal fibroblastogenesis toward connective tissue commitment. The major stages of skeletogenesis entail: 1.) MSC migration and outgrowth, 2.) aggregation, 3.) differentiation, and then 4.) morphogenesis. A complex set of genes govern the proper assembly and direction of MSCs toward presumptive locations and subsequent maturation (Fig. S1). These genes codify transcription factors and other proteins involved in cell-to-cell interactions and intracellular signaling pathways. In time, regulatory circuits are formed which provide information about identity and spatial position among migrating cells, and these circuits regulate processes such as segmentation of embryonic structures.

Figure 1. Derivation of the skeleton
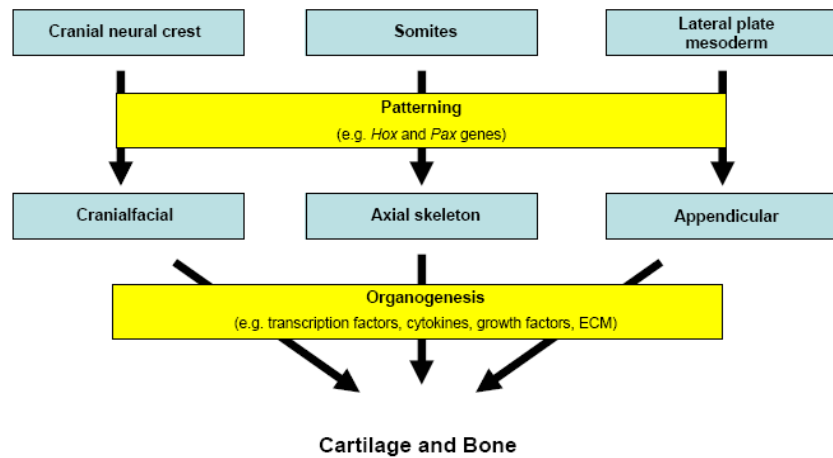
Within skeletal elements, mesenchymal condensations are either *osteogenic* (bone-like) or *chondrogenic* (cartilage-like) propagations (Fig. 2; (13)). Both types of condensations entail expression of specific genes in a spatial-temporal fashion encoding receptors, adhesion molecules, matrix proteins, and transcription factors promoting cell adhesion, boundaries, and the capacity of aggregation toward future tissues (14). Chondrogenic condensations give rise to the axial and limb skeletons, and to the base of the skull. Osteogenesis is the transition of MSCs directly into bone forming osteoblastic cells. During osteogenesis, epithelial–mesenchymal interaction initiates preosteoblastic differentiation before condensation. Preosteoblasts then condense, become functional osteoblasts (OBs), and finally deposit bone matrix. Bone morphogenic proteins (BMPs) and their antagonists (e.g. Noggin), as examples, mediate the recruitment of neighboring mesenchymal precursor cells into the condensations, and thus establishing their final morphological dimension and capacity.

Figure 2. Epithelia-mesenchymal interaction, condensation and differentiation
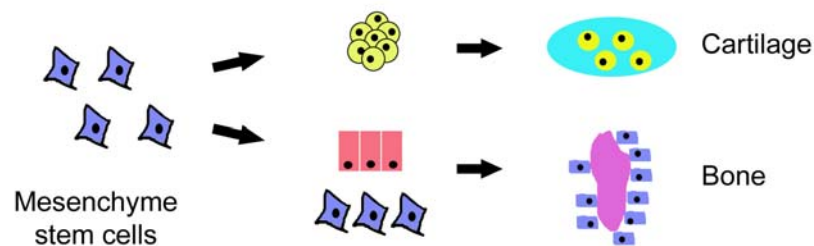
(Fig. 2) Stelate-shaped mesenchymal cells condense and differentiate into either pre-chondrogenic (upper) or pre-osteoblastic (lower) groups depending on epithelial (pink)-mesenchymal interactions. Cartilage (cyan) is formed from differentiated chondrocytes, while during intramembranous ossification (see later), calcified bone matrix (dark pink) is surrounded by cubical OBs. The epithelial-mesenchymal interaction is closely involved during craniofacial development, and less during limb development.

1.1.1 Cartilage

Cartilage is a resilient connective tissue that plays a variety of mechanical and regulatory roles in the body (15). There are specialized forms of cartilage, whereby hyaline cartilage provides mechanical support for the respiratory tree and airway, nose, articular surfaces and developing bone. Elastic cartilage contains a large amount of elastic fibers and collagen, and is more versatile in supporting structures such as the larynx, epiglottis, and external ear. Fibrocartilage resembles both dense connective tissue (i.e. containing thick collagen fibers) and cartilage, and is both tough and deformable, found within intervertebral disks and tendon insertions.

Chondrocytes synthesize and deposit macromolecules for the matrix that forms the surrounding environment. Chondrocytes also produce some of the growth factors for proliferation, differentiation and growth, while adjacent tissue during development secret other specific factors. Cartilage growth occurs by expansion of the ECM either from within (i.e. interstitial growth via dividing isogenic groups) or on the surface (i.e. appositional growth). As the macromolecules are slowly turned over, chondrocytes replenish components of the matrix (Fig. S1). The ability to remodel and repair the matrix is limited as no blood vessels and vascular channels penetrate cartilage due to the expression of several inhibitors of endothelial cell growth by differentiating chondrocytes. All nutrients diffuse into cartilage from the nearest blood vessels in the *perichondrium*, a dense renewing fibrous connective *peri-chondrium* tissue encapsulating the surface of cartilage. The attributes of cartilage are due to an abundance of ECM proteins consisting of fine collagen fibrils and high concentrations of glycosaminoglycans (GAGs) and proteoglycans. Minor cartilage collagen types IX and XI bind to the surface of major type II fibrils creating the macromolecular structure of the cartilage matrix. Expression of type X collagen is restricted to the degrading cartilage undergoing conversion to bone at the epiphysial hypertrophic zone. Hyaluronic acid (i.e. a GAG) constitutes a major matrix macromolecule in cartilage and is highly charged leading to the attraction of water for resistance to deformation. Aggrecan (i.e. a proteoglycan) attaches to both the hyaluronic acid backbone and type II collagen forming a megacomplex, whereby the collagen fibrils provide tensile strength, but do not resist compression or bending.

1.1.2   Bone

There are over 200 bones varying in size and shape that compose the human and mouse skeleton that reflect function. Mature bone is a unique type of connective tissue due to mineralization. It is a composite of organic matrix (~35 %) and inorganic elements (~65 %) consisting mainly of type I collagen and calcium hydroxyapatite (HAP) providing both rigidity and hardness respectively. HAP ($Ca_{10}[PO_4]_6[OH]_2$) is a calcium phosphate nanocrystal embedded into collagen fibrils. The bone-forming cells consist of osteoprogenitors (i.e. pluripotential MSCs located mostly in the marrow region), OBs

Figure 3. Major cells of the bone environment
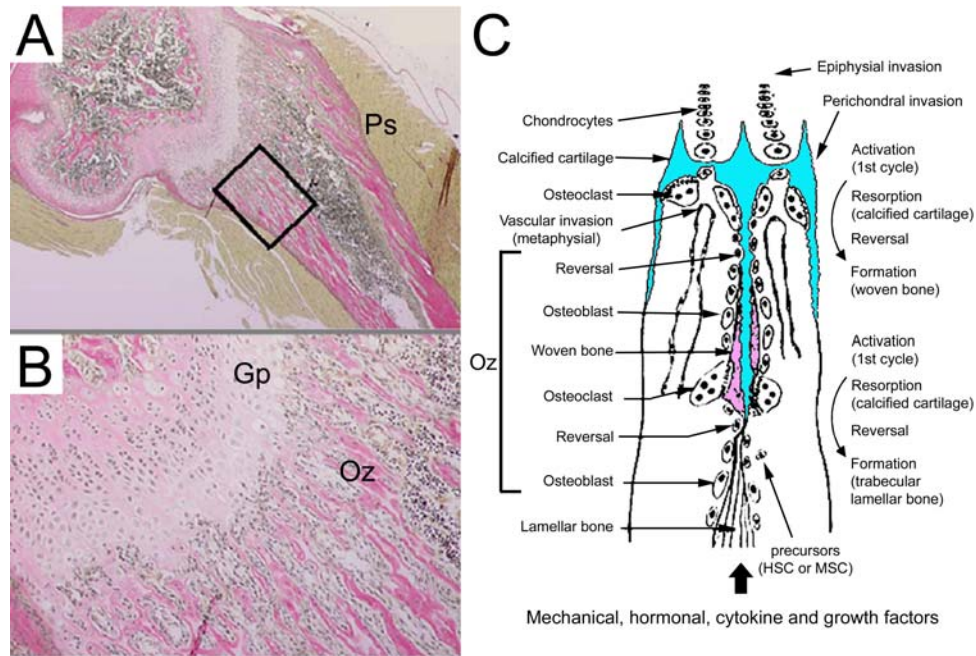
(Fig. 3) Decalcified section of 3-week-old mouse femur. In *A*, macro view of a mouse femur stained with Von Kossa (i.e. black mineral staining not present). Appositional growth occurs at the femoral periosteum (PS). In *B*, zoom of the subchondral and growth plate regions. In *C*, scheme of endochondral bone formation at the epiphysial plate and metaphysis. Growth plate (Gp), osteogenic zone (Oz), hematopoetic stem cell (HSC), mesenchymal stem cell (MSC)

(i.e. resting and active cells located on bone surfaces) and osteocytes (i.e. terminally differentiated OBs encased in bone; Fig. 3). The production, stimulation and maturation of these cells are mediate by cell-matrix/cell communication, cytokines, and growth and stress factors (Table S1). External surfaces of bones are covered either by a dense connective tissue called the *periosteum* or by cartilage at joint surfaces. Blood vessels supply the medullary cavity with nutrients and MSCs, and penetrate cortical bone through a network of channels.

periosteum

Osteoclasts (i.e. derived from hematopoietic progenitor cells) are also a part of the bone environment located at bone surfaces, and responsible for bone resorption. Osteoclasts (OCs) are multinucleated giant cells distinct from monocytes and macrophages which are also derived from the same progenitor cells. CSF1 (macrophage colony-stimulating factor-1) conveys the proliferation, fusion, differentiation and survival of blood monocytes (macrophages) into multinucleated OCs (16). The differentiation of OCs from preosteoclasts is mediated by the ligand to receptor activator of NFκB (RANKL; otherwise called osteoprotegerin), c-Fos and NFκB. OCs attach to bone surfaces via interactions of plasma membrane integrin receptors with bone matrix proteins. This interaction creates a leak-proof compartment containing a 'ruffled border' composed of microvilli enriched with V-type H$^+$

transporting adenosine triphosphatases (ATPases) and chloride channels to secret hydrochloric acid to dissolve calcium phosphate crystals. Additionally, OC secret proteolytic enzymes (e.g. cathepsin K) that digest collagen and other organic components. As bone is resorbed and broken down to its elemental units, key substances are released (e.g. TGFß) which initiate its renewal for proper homeostatic counterbalance.

Many transcription and growth factors mediate commitment, proliferation and differentiation of OBs (17, 18). Cbfa1 (runt related transcription factor 2, or Runx2) is a key transcription factor that (positively and negatively) mediates the expression of genes necessary for bone matrix formation during OB and chondrocyte differentiation. Upstream are homeobox transcription factors (e.g. Dlx5/6, Msx2, Bapx1) which upregulate Cbfa1, whereas Hoxa-2 suppresses Cbfa1. BMPs are known to stimulate Cbfa1 expression, while TGFß suppresses its expression. Type I collagen and tissue-specific alkaline phosphatase (ALP) are molecular markers for early osteoblastic differentiation. Osteocalcin expression and mineralization of the ECM are molecular events that occur at later stages of osteoblastic cell differentiation.

The proteins of bone include type I collagen and a family of non-collagenous proteins mostly derived from OBs (Fig. S2). Non-collagenous proteins of bone adhere to the matrix, and are categorized according to their function as adhesion, calcium-binding, or mineralization proteins, enzymes, cytokines or growth factors. A monolayer of OBs on the surface of growing bone uses a well-established and regulated secretory pathway to synthesis and deposit organic components of the matrix. Upon new bone formation (see later), OBs lay down osteoid (i.e. non-mineralized organic matrix in which immature type I collagen, lamina and fibronectin are the major components), whereby non-collagenous proteins fibromodulin, biglycan and decorin directly bind to gaps between type I collagen fibers regulating proper fibril formation and mineral deposition. OBs deposit collagen either in a random mesh known *woven bone* as *woven bone* or in an orderly striated pattern termed *lamellar bone*. Typically, woven bone *lamellar* is observed in fetal skeleton and formed at distinct regions of the growth plates. The presence *bone* of woven bone in the adult is always indicative of a pathologic state. Lamellar bone gradually replaces woven bone during maturation and growth, and is deposited slower, and is more versatile.

Once an OB becomes encased within the bone matrix it is termed an *osteocyte*. *osteocyte* Osteocytes are connected to each other by long filopodia that migrate through narrow channels in the matrix. The establishment of gap junctions between the osteocytic processes provides a continuous network of intercellular communication to adjacent cells, blood vessels

and to the innermost embedded osteocytes themselves. Osteocytes also make connections with active and resting OBs, and are less active than OBs, but deposit and resorbe matrix in their immediate vicinity.

1.1.2.1 Intramembranous and endochondral bone formation

Intramembranous ossification entails bone being first laid down as an arrangement of mesenchymal osteogenic condensations without the cartilage intermediate model, and generates the clavicle, calvaria and flat bones of the face. For example in the skull, the primitive membrane that enshrouds the cranial vault forms ossification centers derived from MSCs that become OB progenitor cells. The progenitor cells specialize to become OBs and then begin synthesis of bone matrix to develop trabeculae of the plates separated by unossified sutures. Cells encasing the developing bone will form the periosteum to produce compact bone for proper organogenesis. Maintenance of appositional growth and the medullary space of the membranous skull plate results via proliferation of OB lineage precursor cells recruited via vascularization.

Long-bone formation in the limb has been studied in great detail and provides the basis for understanding the cellular and molecular processes of intracartilagenous (endochondral) bone formation (Fig. 4). Growth takes place at the epiphysial growth plate of long bones by a finely balanced and complex cycle of cartilage production, matrix formation, calcification and degradation of cartilage which acts as a scaffold for new bone formation. The replacement of cartilage is presumed to occur during embryonic development, growth, fracture repair, and at ectopic locations.

The embryonic primordiae of the appendicular skeleton are the limb buds, which are mesodermal structures covered by ectoderm. The first visible outline of the embryonic limb signifies a condensation of MSCs that subsequently differentiate into chondroblasts that produce a hyaline cartilage model. In mice, the cartilage anlage primordia can been observed at approximately 11.5 days of gestation (19). Around this model is the perichondrium, an outer layer that later becomes a connective tissue sheath, whereas the inner cells remain pluripotent. The conversion from chondrogenic condensations to cartilage anlage for future skeleton accompanies changes in bifurcation and segmentation of the forming structures. As the chondrocytic front approaches the ends of bones, chondrocytes proliferate as stacks of flattened newborn cells. Chondrocytes in the center of the anlage start to

Figure 4. Long bone formation
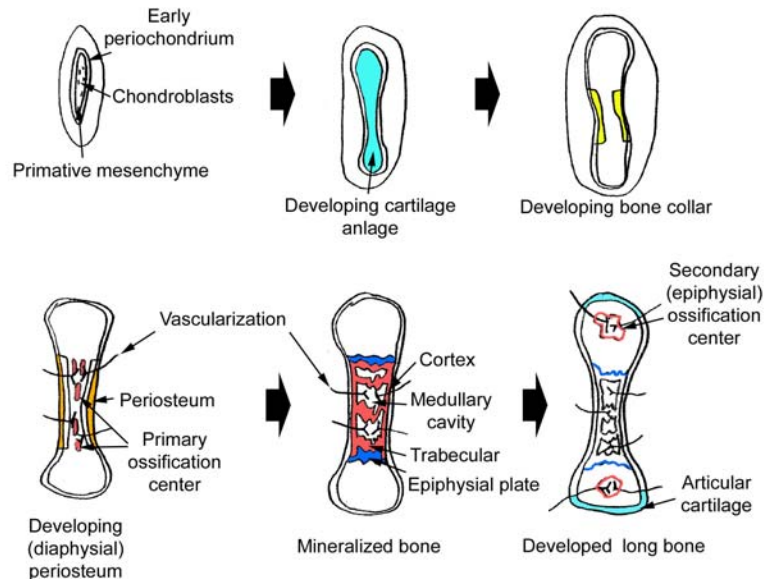
(Fig. 4) Formation of bone by replacement of the cartilage model (light blue). The shaft expands in diameter as OBs lay down bone on the outer surface of the primary bone collar (yellow). The primary ossification center (red) soon develops, and OCs remove bone from the inner surface to form and maintain the medullar spongy cavity. The long bone grows in length by interstitial expansion of the cartilage in the growth plate (dark blue) and its replacement by bone.

terminally differentiate and cease to express chondrocyte-specific genes (e.g. Sox9), upon which they start taking the cellular phenotype of pre- and hypertrophic chondrocytes expressing Indian Hedgehog (Ihh), type X collagen, VEGF, hypoxia-inducible factor 1α (HIF-1α) and ALP. Concomitant to these changes, MSCs of the perichondrium near the future-shaft begin to differentiate toward OBs creating a perichondrial collar of membranous bone. Meanwhile, chondrocytes enlarge and the hypertrophic cartilage matrix begins to mineralize as the primary ossification center. VEGF and other angiogenic factors in the central anlage induce angiogenesis, and vascular invasion recruits OCs, OBs and hematopoietic cells into the anlage as the most terminally differentiated chondrocytes finally die via apoptosis. The OCs begin to proteolyse the hypertrophic cartilage matrix which also serve as a scaffold for deposition of osteoid by OBs, and further facilitating the invasion process via VEGF release. The secondary ossification center emerges at the ends of long bones. Periosteal buds carry MSCs and blood vessels similar to that which occurred at the primary ossification center. A thin cap of articular cartilage remains at the joint cavity, which is not replaced by the secondary ossification center. The cartilage between the primary and secondary ossification centers becomes the growth plate, and continues to form new cartilage leading to centripetal bone lengthening. After the growth period, the plate cartilage is replaced by bone, and then

called the epiphysial line. Thus, long bone endochondral development commences via vascular invasion of the cartilaginous model.

During development and late-stage endochondral bone formation and maintenance, there are three crucial signaling molecules involved at the growth plate. The first is PTHrP (parathyroid hormone-related peptide) which is expressed at the periarticular regions of the growth plate and inhibits the rate of columnar chondrocytic proliferation exiting the cell cycle towards hypertrophy, thus maintaining chondrocytes in a proliferative state. The second is Ihh which controls the expression of PTHrP and its receptor (PPR) located predominantly on prehypertrophic chondrocytes and early chondrocytic cells. These two molecules form a negative feedback loop to synchronize chondrocyte differentiation in which Ihh expression at the prehypertrophic-hypertrophic boundary functions to keep the chondrocytes in the proliferative compartment via the production of PTHrP. The third molecule is FGFR3 (fibroblast growth factor receptor 3) which inhibits chondrocyte proliferation via a Stat1 and p21 (cell cycle inhibitor) pathway.

1.2   Modeling and homeostasis

A key feature of bone growth is the process of *modeling*, where bone is continuously resorbed and replaced with net new bone formation. Modeling is most active during childhood and adolescence, and enables long bones to increase in diameter, to change shape and develop a marrow cavity. Modeling continues throughout the growth period until peak bone mass acquisition. In the adult, the process of maintenance of existing bone is referred to as *remodeling* or *homeostasis*, where bone resorption is equally and optimally balanced by bone formation in a healthy skeleton. An individual's skeletal growth rates and bone lengths have important genetic determinants, but are influenced by many other factors including circulating (sex) hormones, nutritional intake, mechanical forces and disease. For example, Wolff's Law states that the optimal organization of bone reflects its resistance to load imposed by functional activity (20). In another word, remodeling is normally matched to the stresses on the bone, and therefore bone exists in a continuous remodeling state.

modeling

remodeling/ homeostasis

Bone cells are functionally linked during bone re/modeling via complex regulatory networks. A coupling cycle exists between OBs, osteocytes, OCs, bone-lining cells, hematopoetic cells and all their precursors through complex cellular interactions with the intent of removing aged or compromised bone with freshly organized osteoid in a regulated fashion (21-23). For example, involvement of osteocytes and osteoblastic stromal cells in the

release of RANKL, a member of the tumor necrosis factor (TNF) superfamily, and CSF1 presumably keep OCs in coupling balance.

Bone homeostasis also partly involves the physiological regulation of extracellular Ca^{2+} levels via circulating parathyroid (PTH) and calcitonin (CT) peptide hormones through their influences on OBs and OCs respectively (24, 25). CT secretion is regulated by thyroid membrane-associate Ca^{2+}-sensing receptors (CaRs) and transcriptional activation, and counters the effects of PTH. CT decreases blood Ca^{2+} levels via limiting intestinal and kidney tubule Ca^{2+} absorption and OC activity. The parathyroid gland secrets PTH in order to regulate the calcium concentration in blood. The PTH axis induces osteocytes to mobilize calcium from the surrounding matrix. In addition, the hormone leptin (secreted by adipocytes in connective tissues) acts on the hypothalamic nuclei (i.e. the satiety center) in the brain to regulate appetite and energy metabolism that affect bones. Bone homeostasis is also under the control of many other preresorptive and calciotropic factors including: $1,25(OH)_2$ vitamin D_3 (i.e. via calcium absorption form diet and blockage of urinary excretion), PGE2 (prostaglandin e2), IL-1, IL-6, TNF, prolactin, corticosteroids, oncostatin M, and LIF (leukemia inhibitory factor). Anabolic or anti-resorptive factors include estrogens, BMP2, BMP4, TGFß, TPO (thrombopoietin), IL-17, PDGF (platelet-derived growth factor), and calcium itself. Disturbances in the aforementioned factors can lead to debilitating disorders such as osteoporosis and osteomalacia (Table S1).

1.3   The collagens: Major structural and regulatory components of the ECM

Over the past decade collagens have been extensively investigated to provide enriching details about their functions (26-36). The collagens are the major *extracellular matrix* (ECM)   *ECM* proteins of vertebrate connective tissues and play important roles in development and homeostasis (27, 37). Many collagens have restricted tissue and cellular expression, while others are ubiquitously expressed in the ECM. As of date, 28 collagen types with 43 distinct polypeptide chains are known to exist in vertebrates (37). The major collagen families comprise of molecules that assemble into higher-order (micro) fibrillar, sheet-forming, transmembrane, FACIT (fibril-associated collagens with interrupted triple helices) and anchoring structures (Table S3; (38)). Collagens require specific molecular interactions with other matricellular proteins in providing proper overall tissue integrity (39). Besides providing an ECM and basement membrane scaffold for various tissues, collagens are also involved in dynamic processes such as chemotaxis and migration (40), cell adhesion (41), growth plate

matrix vesicle and bone mineralization (42), remodeling (43, 44), differentiation (45), wound healing (46), gene regulation of hematopoietic stem/progenitor cells (47) and cancer progression (48-51).

1.3.1   Type I collagen: Biosynthesis, processing, structure and regulation

Type I fibrillar collagen is constitutively expressed in many tissue settings such as bone, tendon, ligaments, dermis, bone marrow stroma, heart, lung parenchyma, mesenchyme, mammary gland, fascia, dentin, testis, granulation tissue, cornea, sclera, and the endomysium of myofibrils (UniGene Mm.277735; (30, 38, 52-60)). Fibrillar collagens (i.e. I, II, III, V, XI, XXIV, XXVII) are organized into highly-ordered, quarter-staggered fibrils covalently cross-linked to increase tensile strength and rigidity. Type I collagen is a heterotrimeric complex constructed of two α1 and one α2 precursor procollagen chains transcribed from two separate genes (*COL1A1* and *COL1A2*; MIM 120150 and 120160 respectively) that self-associate into trimers in the endoplasmic reticulum (ER) via C-propeptide domains (Fig. 5; (33, 61, 62)).

Nascent procollagen chains undergo post translational modifications critical for proper folding, intramolecular stability, and vesicular cellular transport through the Golgi towards exocytosis (Fig. S2). Glycosylation and hydroxylation of procollagen molecules are the major post-translation events known to occur. Hydroxylation reactions secure and nucleate the chains in the triple helix of collagen via hydrogen bonds (63). Besides proline (see below), lysines at the telopeptide regions are hydroxylated (catalyzed by lysyl hydroxylase) transforming them into hydroxylysines. Several rounds of glycosylation concomitantly occur within both the ER and Golgi apparatus for proper procollagen processing into secretory vesicles during exocytosis to the ECM. In cases where the triple helix is compromised, over glycosylation of type I procollagen chains is known to occur.

Fibrillar collagens are highly conserved in all multicellular animals, whereby the 54 bp ancestral nucleotide triple helical unit was replicated numerous times (Fig. 6; (32)). The triple chain collagen helix forms the central, proteolysis-resistant domain of the procollagen I molecule, and is flanked by two substantial non-collagenous domains called the *amino* and *carboxyl propeptides*. The triple helical structure of collagen arises from a large abundance of the three amino acids glycine, proline, and hydroxyproline (Hyp; synthesized post-translationally via prolyl hydroxylase). A principle structural element in the folding

amino/ carboxyl propeptides

Figure 5. Fibrillar type I procollagen molecule
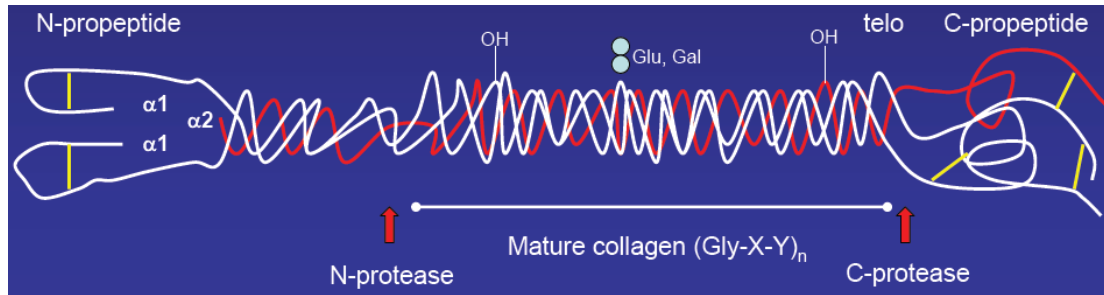
(Fig. 5) Unprocessed mature type I collagen with two pro alpha 1 chains and one pro alpha 2 chain. Yellow bars signify intra and interchain disulphide bridges. Hydroxylated (OH) and glycosylated (Glu, Gal) residues are shown. N- and C-propeptide regions are clipped during fibrillogenesis for proper fibril assembly.

maturation of the polypeptide chains into a triple helix is a sterically small glycine residue located at every third position near the central axis, thereby creating a $(Gly-X-Y)_n$ triplet repeat which is symbolic of all collagens (Fig. S3). The hydrogen bonds linking the peptide bond NH of glycine residues with peptide carbonyl (C=O) groups in an adjacent polypeptide governs intramolecular bonds which maintain the three chains together (64). The C-propeptide region of both procollagen chains are globular in structure and arranged into internally disulfide-linked complexes. The three folded intra-chain carboxyl peptide regions are also disulfide-linked to one another for stability, proper cellular processing and exocytic protection (65). All collagens to date are known to contain these three-stranded helical domains of similar structure, whereby the distinct properties of each collagen type are due mainly to segments that alter the triple helix and that fold into other forms of three-dimensional structures. In time, the processed procollagen molecules are deposited into the extracellular space, proteolytically cleaved by NH_2- and COOH-proteinases, and then the monomers are organized into highly-ordered collagen fibrils covalently cross-linked to increase tensile strength and rigidity to withstand stretching (see later; (66)).

Multiplex *cis*- and *trans*-acting regulatory elements and protein factors (e.g. homeodomain proteins and cytokines) of *col1a1* in bone have been evaluated in detail and revealed (tissue-specific) sites of biological importance (67, 68). Dysregulation at the transcriptional level can cause clinical conditions such as scleroderma and/or other tissue fibroses. Previous studies in humans identified associations between altered BMD and osteoporosis with polymorphisms within the proximal promoter of *COLIA1* and in its first intron (69), which constitutes a binding site for the transcription factor Sp1. The full repertoire of promoter binding factors which modulate COL1A1 expressivity are unknown and of medical interest.

Figure 6. Mouse pro alpha 1 type I collagen (pro-α1[I]) chain structure
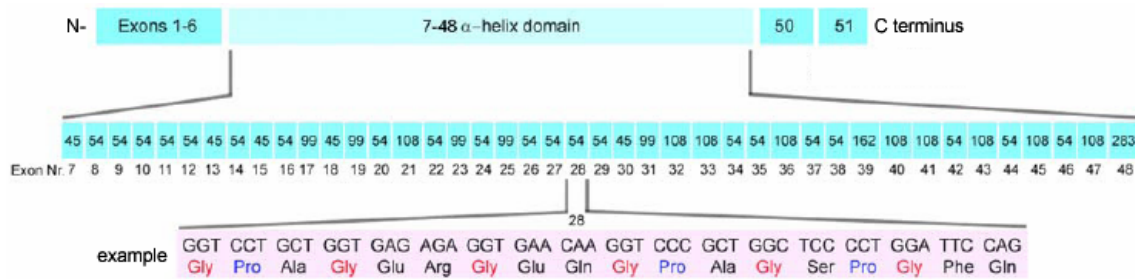
(Fig. 6) The major domain of the procollagen I molecule consists of a central triple chain helix flanked by amino and carboxyl non-collagenous propeptide domains. The (Gly-X-Y)$_n$ triplet repeat region is highlighted within exon 28, whereby any amino acid could substitute in the X and Y positions, but proline and Hyp are more often the case. *M. musculus* type I collagen protein and DNA sequences are 92.2 % and 89.3 %, respectively, homologous compared to *H. saipen* (http://string.embl.de).

1.3.2   Fibrillogenesis and cross-linking

After the assembly and processing of type I procollagen is complete, it is secreted within the extracellular space and the non-helical N and C terminus extensions (telopeptides) are trimmed by peptidases generating polymerized mature collagen fibrils capable cross-linking (33, 53). Before extrusion, long collagen fibrils are thought to reside within the cell, where coexisting with shorter fibrils via a specialized fibripositor (fibril-depositor) structure. Also, the proteolysis of full length procollagens is though to occur within the infoldings of the plasma membrane. Fibrillogenesis is tightly regulated by numerous non-collagenous proteins, many of which are still unknown (39). The telopeptide segment at either ends of the collagen molecule are important in the regulation of collagen fibrils via the cross-linking hydroxylysine residues (70, 71). Additionally, these segments are known to contain highly conserved amino acid sequences suggesting other important functions (72). Fibrillogenesis is regulated via lysyl oxidase, which is responsible for tissue-specific oxidative deamination of lysine and hydroxylysine residues in the formation of reactive aldehydes for cross-linking. These aldehydes spontaneously form specific covalent cross-links between two neighboring triple-helical molecules, which stabilizes the staggered packing array characteristic of collagen fibrils (Fig. 7). This quarter staggered distance or displacement (called the D-period, or one fibril unit) represents two distinct regions, the overlap (~20 nm in length) and gap (~47 nm in length). The type of cross-link generated is dependent on tissue-specific enzymatic

Figure 7. Type I collagen basic unit (the fibril) and interacting partners
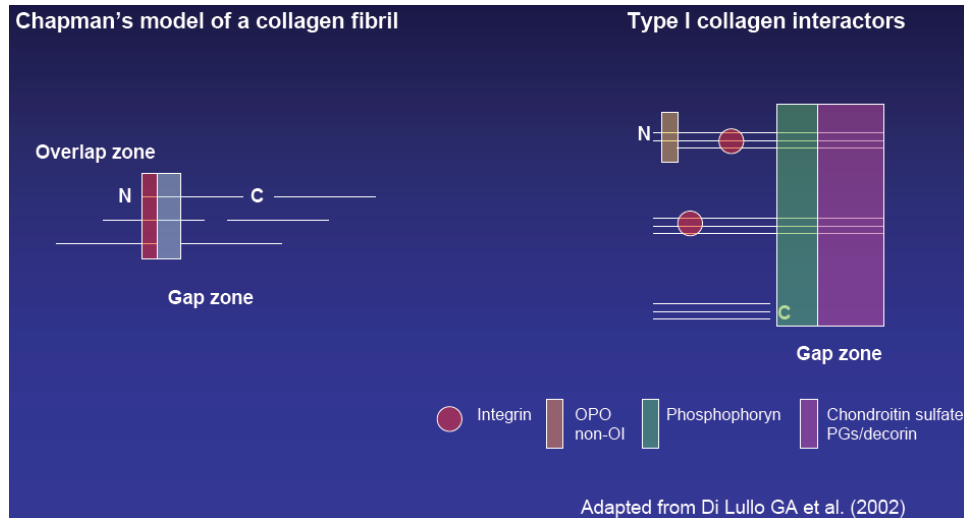
(Fig. 7) Collagen fibril composed of multiple mature collagen molecules in a quarter stagger arrangement. Cross-linking occurs at the N and C terminals between adjacent collagen molecules. The overlapping zone is shaded in red and gapped zone in gray. Multiple fibrils comprise a bundle, while multiple bundles form a collagen fiber (not shown). Over 80 individual interactors are known to bind to type I collagen. Decorin and other proteoglycans (PGs) are shaded purple and interact with collagen in the gap zone. Other gap zone binding sites included dentin phosphophoryn (indicated by the green box). Integrin receptor binding sites are located in the overlap zone of type I collagen. Nominal interactors are located near the N terminus (orange box), whereby mutations affecting these regions are known to cause mild osteoporosis (OPO) and non-OI phenotypes. Mutations which affect the gap zone are known to cause a dentinogenesis imperfecta phenotype, suggesting these interactors to be important in odontoblast function.

hydroxylation reactions, not on collagen types. The deposition of HAP crystals in bone, for example, is highly dependent on proper fibrillogenesis of type I collagen molecules.

1.3.3 Regulatory and physiological functions

Apart from its biomechanical properties of load-bearing tissues, specific spatial and temporal organizations with type I collagen are known to mediate cell adhesion, migration, polarity, proliferation, differentiation, survival, tumorigenicity, fibrosis, glycation, wound healing, tissue remodeling and interactions with non-collagenous matricellular proteins involved in calcification and fibrillogenesis within various cellular niches (28, 30). In addition, type I collagen retains IL-2, growth factors and thrombospondin, maintaining a role for glycoprotein inhibition of angiogenesis during ECM degradation and remodeling (73). Furthermore, the interactions of type I collagen with the GAG chondroitin sulphate of proteoglycans (e.g. decorin) are also believed to be important in the assembly and arrangement of macrostructures (74, 75). Of late, the type I collagen bone matrix scaffold may also play an influential role for

bone marrow-derived MSCs during their osteogenic differentiation within the bone niche (34, 76, 77). These events are mediated, for example, when type I collagen acts as an adhesive substrate with cellular ECM receptors (36, 78-80), and other matricellular components along major ligand binding regions (MLBRs) to regulate complex intracellular signal transduction pathways. A structurally and functionally heterogeneous group of cell surface receptors mediate the recognition of triple-helical collagens that include: integrins, discoidin domain receptors, glycoprotein VI, leukocyte-associated IG-like receptor-1, and members of the mannose receptor family (29, 81). Along with signals arising from other receptors for soluble growth factors (e.g. VEGF and EGF), collagens dictate cellular decisions on what biological action to embark.

Functionally, the helical domain of the type I collagen molecule provides tensile strength and serves as a matrix template for future mineral deposits in bone. The function of processed NH_2 terminal propeptides of type I collagen are unclear, but several important roles have been considered (82). Moreover, an early vertebrate developmental role for α1(I) N-propeptides was shown via a feedback mechanism involving a potential intracellular secretory cytokine receptor(s) regulating cell differentiation and collagen biosynthesis (66). Distinctively, the α1(I) terminal C-propeptide region is crucial in mediating procollagen chain association (33). The C-propeptide region is crucial in mediating procollagen folding by providing association between individual procollagen chains (63), and also chain selectivity via unique conserved discontinuous sequences (Fig. S4; (83)). Type I collagen C-propeptides also modulate collagen synthesis (i.e. augmenting its own synthesis), promote OB attachment, and regulate the bone metabolic effects of TGFß (84, 85). In addition, C-terminal trimers were shown to induce homing and metalloproteinases in breast carcinoma cells, potentially influencing cancer progression (86). Recently, Endo180, a urokinase plasminogen activator receptor-associated protein (uPARAP) involved in endocytic cellular uptake and degradation of collagens in the lysosomal compartment (87, 88), was shown to selectively bind both C-terminal pro- and α1(I) collagens regulating matrix adhesion, although the potential mediation of cell transformation remains unclear to date (89).

1.3.4   Osteogenesis imperfecta

A large collection of collagen mutations have been identified in heritable diseases such as osteogenesis imperfecta (OI; (90)), Ehlers-Danlos syndrome (EDS), chondrodysplasia, intervertebral disc disease, Alport syndrome, Bethlem myopathy and Ullrich muscular

Figure 8. OI clinical heterogeneity and mutational landscape
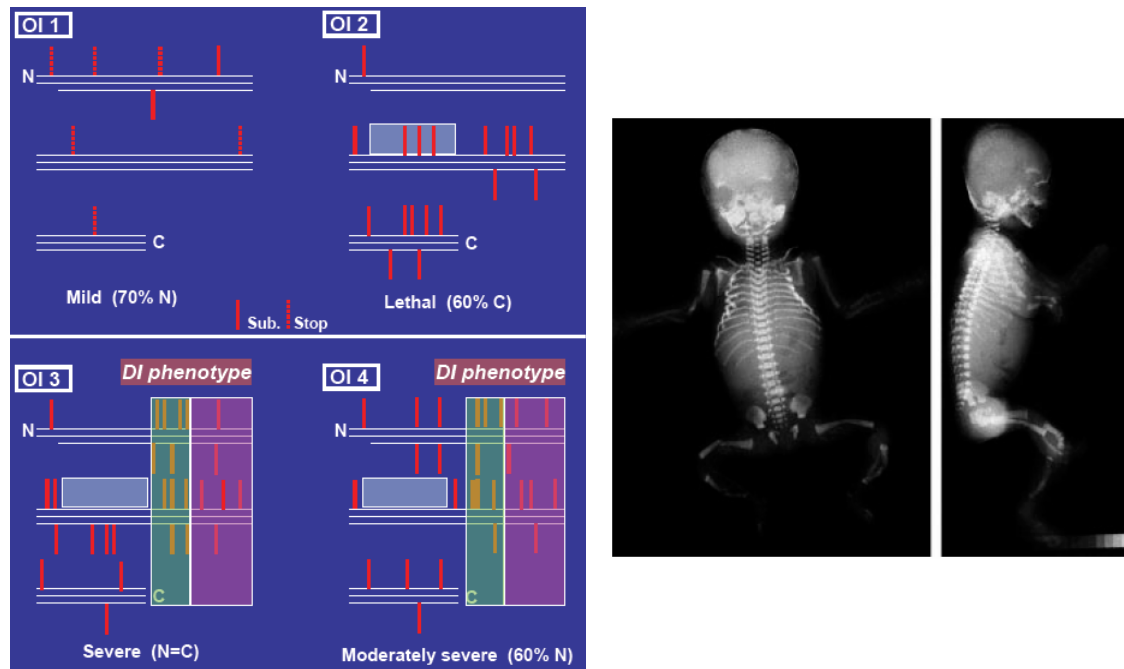
(Fig. 8) Variable phenotypes in OI. The tensile strength and signaling capacity of type I collagen is affected to varying degrees depending on the location of *COL1A1/2* mutations (left). OI mutations (e.g. either stop or substitution) affect phenotypes by altering binding interactions (green and purple boxes for crucial proteoglycans), processing of procollagen and collagen molecules (e.g. trafficking and post translational modifications), and mRNA stability. Regions may also define interactions which regulate lethality (i.e. gray box). Mutations in the terminal C-propeptide region typically result in perinatal lethal probands with clear type II OI radiological features (right; image taken from Pace et al. 2002 (91)). Adapted from the type I collagen human mutation database (92). Dentinogenesis imperfecta (DI), N-terminus (N), C-terminus (C)

dystrophy (28). Human mutations in type I collagen genes and alterations in the product synthesis and processing lead to inherited and acquired connective tissue disorders such as OI, osteoarthritis, aortic aneurysms, EDS, achondrodysplasia, osteopenia, osteoporosis, cortical hyperostosis, and various forms of muscular dystrophy, (10, 28, 90, 92-96). In particular, OI (MIMs type I 166200, II 166210, III 259420, IV 166220) is a heterogeneous disease classified by eight sub-types and is the most common heritable cause of skeletal fractures and deformity in humans (90, 92, 95, 97-100). The OI clinical features are a continuum ranging from perinatal lethality, individuals with severe skeletal deformities, fractures and reduced bone mass, and to asymptomatic conditions of mild predisposition to disease (101). Based on the clinical description, OI-I is considered mild with respect to types III and IV, which overlap in presenting a more severe phenotype of deformation, yet with normal sclera in the latter. The severity of the clinical phenotypes is partly related to the type of mutation, its location in the alpha chain, the surrounding amino acid sequences, and genetic interactions (Fig. 8; (10)).

Generally, N-terminal mutations within *COL1A1/2* lead to mild clinical symptoms, while core and C-terminal defects result in severe to severest OI phenotypes respectively. Substitution mutations of type I collagen at glycine positions are known to alter helix assembly and propagation, thereby exposing all three chains to elevated hydroxylation and glycosylation (90, 102, 103). Furthermore, alterations of the Gly-X-Y structure or procollagen assembly can cause increased chain flexibility, thus succumbing the procollagen molecule to increased proteolytic degradation toward discrete phenotypes. Of late, novel molecules and loci other than classic type I collagens have been implicated in recessive forms of OI, thus broadening the genetic heterogeneity in OI-related cases (104-107).

1.3.4.1 Type II OI

Type II OI represents the most severe form of the disease (consisting of subtypes A-C; (97)), whereby most probands die within the perinatal period, and account for ~20 % of all reported cases (108). Most OI-II probands acquire *new* dominant mutations in *COL1A1/2*, and a low frequency recurrence risk can be the result of gonadal mosaicism in one of the parents. In brief, the heterogeneous clinical phenotype of human OI-II is characterized as having abdomen protuberances, respiratory stress, laxed ligaments, poor muscle tone, bowed and truncated limbs, woven bone, de-ossified calvaria, generalized and localized osteopenia, intracranial bleeding and extensive fractures. OI-II-related mutations act in a dominant lethal manner as the mutant α(I) propeptides affect wild-type chain registration and assembly due to the polymeric nature of formation (i.e. called procollagen suicide; (109)). Consequentially, abnormal trimers are usually poorly passaged through the secretory pathway, and are more vulnerable to degradation and overmodification, thus compromising fibril formation and impairing overall ECM integrity and interactions. Moreover, critical steps of the cytoprotective unfolded protein response (UPR) are known to be concordantly activated due to certain C-terminal mutations (110-112), and lead to ER stress-induced apoptosis and cell death during more severe circumstances (Lisse et al, submitted). Recently, differential protein expression analysis revealed involvement of apoptosis-inducing factor Gadd153 (growth arrest and DNA damage inducible protein 153) within lethal animals of the BrtlIV OI muine line, suggesting the specific involvement of apoptosis in governing clinical variability (113).

1.3.4.2 ER stress response and caspases

Several disorders such as lysosomal storage disease, cystic fibrosis, 1-antitrypsin-mediated emphysema, hypothyroidism, multiple epiphyseal dysplasia, neurodegenerative diseases, and cancer result from the cells inability to export mutated proteins and enzymes from the ER (114, 115). These deleterious ER stress-induced conditions activate remodeling and compensatory tissue protective mechanisms which upregulate genes necessary to manage the entire ER folding machinery if the cellular damage is not adequately cleared (114, 116-121). The unfolded protein stress response (UPR) elicits a deluge of cell type-specific quality control pro-survival signaling pathways triggered upon calcium imbalances, accumulation of misfolded proteins and/or inhibition of disulphide formation within the ER (122). The UPR entails: 1.) attenuation of secretory protein synthesis, 2.) transcriptional activation of ER-resident chaperones and 3.) activation of ER-associated degradation (ERAD) pathways (116, 117). Misfolded and unfolded proteins elicit ER stress signaling (ERSS) via activation of ER-resident sensors which can either repress protein synthesis or upregulate ER-resident molecular chaperons and other translation regulators. One ERSS response involves apoptosis if the cellular damage is not adequately maintained. The coupling of ER stress to programmed cell death (PCD) has been reported and involves several pathways, although the entire process has not yet been described (123-125). Of interest, the translocation of Bim (a pro-apoptotic member of the Bcl-2 family; (126)), and the activation and processing of BiP (binding protein/glucose-regulated protein [GRP]78) chaperone and relinquished procaspase-12 (127), respectively, have been described. BiP is a central regulator of ER function due to its roles in protein folding and assembly, targeting misfolded protein for degradation, ER Ca^{2+}-binding and controlling the activation of transmembrane ER stress sensors.

Caspases are components of the mammalian PCD pathways, and entail an inherent minimal inflammatory process in the development, remodeling and senescence of bone cells towards tissue homeostasis (128). Caspase-12 is a member of the interleukin-1ß-converting enzyme (ICE) subfamily of caspases localized to the outer layer of the ER (129) and predominately expressed in skeletal tissues (130). Caspase-12 is a central player in the ER stress-induced UPR and PCD (131), and several models have been proposed for its direct activation, one of which involves crosstalk with m-calpain (129). The complex mechanisms underlying the ability of the cell to target, manage and retain unassembled or misfolded procollagens require the binding of molecular chaperones and actions of post-translational modifying enzymes (28). In many instances of mutated procollagens, partially folded

intermediates are sequestered and blocked from secretion, thereby leading to an accumulation of unfolded chains within the cell. These events likely trigger the cytoprotective UPR as a cell injury reaction to manage aberrant protein accumulation (see later). Despite a dedicated machinery which targets defective procollagens to a retrotranslocation channel for subsequent proteosomal degradation in OI-II cells, no apoptotic link (i.e. a mutational correlation) has been established in OI to date.

1.4   Genetic disorders in skeletogenesis and organogenesis of bone and cartilage

Disorders of the connective tissue and skeletal systems can be classified into groups based on clinical and molecular criteria such as morphology, growth, age of onset, nature of altered body composition, clinical chemical measurements, radiological assessments, genetic causes and hormonal, homeostatic and acquired anomalies (Fig. 9; (132, 133)). The molecular-pathogenic classification of genetic disorders of the skeleton can be grouped into defects which affect: 1.) Extracellular structural proteins, 2.) metabolic pathways (i.e. enzymes, ion channels and transporters), 3.) folding and degradation of macromolecules, 4.) hormones and signal transduction mechanisms, 5.) nuclear proteins and transcription factors, 6.) oncogenes and tumor suppressor genes, 7.) RNA and DNA processing and metabolism, and 8.) immune regulation (133). These categories entail complex molecular and cellular events which affect axis patterning, cell condensation (i.e. mesenchymal adhesion), cell fate determination (i.e. apoptosis, chondrogenesis or osteogenesis), digit and joint formation, ossification, skeletal homeostasis and metabolism (Fig. S1). The highly structured process of endochondral ossification is key to longitudinal bone growth during embryogenesis and early-adult postnatal life. Disruption of this organized process leads to chondrodysplasias (e.g. as seen in PTHrP deficiencies), consisting of a heterogeneous group of heritable disorders depicted by short stature. Apart from known genetic causes of skeletal disorders, cancers such as myeloma and metastases from breast cancer can affect signaling molecules like IL-1 and TNF, and PTHrP respectively that stimulate secondary bone resorption due to malignancy.

Figure 9. Human skeletal diseases
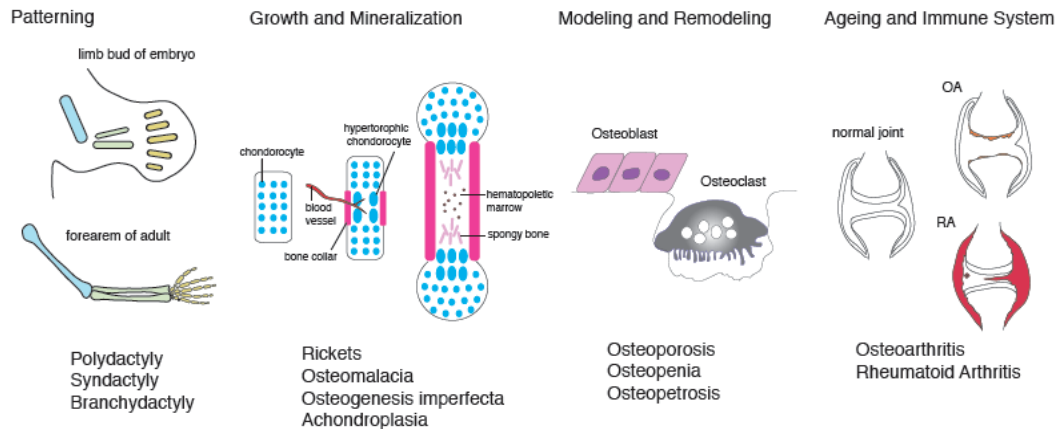
(Fig. 9) Image taken from Fuchs et al. (2006)

1.5   Positional cloning by linkage analysis

Positional cloning studies have identified many important molecules relevant to biology and the medical sciences (4, 134-139). Positional cloning entails a process utilizing gene mapping techniques to locate loci responsible for particular disorders when the cause of disease is unknown (156-161). The mapping of disease loci can be performed by tracking mutant musculoskeletal phenotypes generated by ENU mutagenesis (see next section) using genetic linkage analysis with both microsatellite (MS) and/or single nucleotide polymorphism (SNP) markers (140), as examples. The goal in linkage analysis is the identification of those marker loci that fail to recombine with the target locus in question, and since the positions of the markers are known, the map location of the disease locus can then be systematically inferred by haplotype analysis.

In mice, genetic linkage analysis is conducted via breeding studies in which one or both parents are detectably heterozygous at each of the experimental loci (Fig. 10). Genetic linkage is merely the result of physical linkage of two or more loci along the same pair of DNA molecules of a particular set of chromosome homolog within the diploid genome. In the simplest strategy of linkage analysis, only one parent is heterozygous at the loci, and the reciprocal parent is homozygous at the same loci. The fundamental principle underlying linkage analysis is recombination within the F_1 parent, and outcrossing enables the integration of the genomes to be conducive for polymorphic marker analysis. The N_2 offspring are the only means to analyze recombination, and the meiotic events in F_1 parents are crucial to linkage detection. A linked marker will have fewer recombinational events in the F_1 parent

such that a greater proportion of phenotype-positive N_2 mice will inherit the founder allele (C3H in Fig. 10), and hence be homozygous. Loci which are unlinked will assort randomly and have a recombination rate of 50 %. Map distances are measured in centimorgans (cM) with one centimorgan defined as the separation between two loci that recombine with a frequency of 1 % (i.e. one mouse in 100 will have a crossover event between those two genes).

Figure 10. Principle of linkage analysis
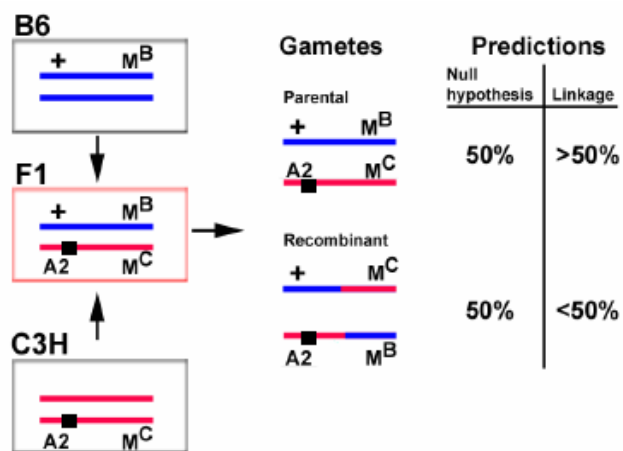
(Fig. 10) Outcross-backcross breeding strategy for dominant mutations. Backcrossing is performed on the B6 strain. The chromatids in the gametes are represented after single crossover events (multiple crossovers can also occur). A2 (target locus), M (polymorphic marker), ■ (mutation)

1.6   Generation of mouse models for human diseases through ENU mutagenesis

A number of mouse models have been generated to study human dysmorphological and connective tissue syndromes using an array of technologies (141, 142). There are only a few large-scale mutagenesis programs for the generation of non-locus-specific phenotypes (i.e. forward genetics) established world-wide in providing mouse models for relevant human diseases. *N*-ethyl-*N*-nitrosourea (ENU) is a potent alkylating agent used to induce discrete (single locus) point mutations in male premeiotic spermatogonia or embryonic stem cells at high rates. ENU acts by transferring its ethyl group ($-C_2H_5$) to nucleobases (usually thymine) in nucleic acids. The advantages of ENU mutagenesis in generating mouse models for human diseases has been well described in offering complementary and more stable systems for

genetic and molecular studies (140, 143, 144). The ENU-derived lines often provide more functional information (i.e. by generating hyper/hypo/anti-morphs) and are more relevant for human diseases where the function of a gene is by large completely eliminated or inappropriately affected due to random target insertion, remnants of foreign DNA, and variable copy numbers within the genome potentially causing anomalies in endogenous tissue distribution using other (transgenic) approaches. For example, the disadvantages of more artificial transgenic and knock-in approaches in attempting to study the genetics and molecular mechanisms of OI within mouse have been previously discussed (145). Therefore, the aim of adequately recapitulating human disorders without the modifying effects from both the genetic and pathophysiological perspective is well retained using ENU.

2.   Materials and methods

2.1   Antibodies, kits and reagents

Activated caspase-3 (R&D Systems, Germany), caspase-12 (BD Pharmingen, Germany), anti-α-tubulin (Sigma, Germany), type I collagen (Abcam, UK), BiP/GRP78 (Abcam, UK) and fluorescently-labeled secondary (Molecular Probes, Germany) antibodies were commercially purchased. Rabbit antisera LF-41 and -67 were generous gifts provided by Dr. L. Fisher (NIH, USA; (146)). Antibody against human ChM-I was kindly provided by Dr. C. Shukunami (147). The mouse TRACP 5b (IDS Ltd, UK) and osteocalcin (BTI, Germany) ELISA, and mouse/rat intact PTH and calcitonin immunoradiometric assay (Immundiagnostik, Germany) kits were commercially purchased. All assays were performed based on the manufacturers' recommendations. All chemical reagents were provided by Sigma.

2.2   Animal housing and handling, and the German Mouse Clinic (GMC) screens

Mouse husbandry was conducted at the GSF under a continuously controlled specific-pathogen-free (SPF) hygiene standard according to the Federation of European Laboratory Animal Science Associations (FELASA) protocols. All animal experiments were conducted under the approval of the responsible animal welfare authority. The animals entered the GMC, an open-access platform for standardized phenotyping, at five weeks of age as previously described (148). Investigations made in the GMC were performed according to standard operation procedures (SOPs). Non-supplemented standard rodent diet (Altromin 1314; Lage, Germany) and water were provided *ad libitum*. Non-*Aga2* and *Ali34* littermates were included as controls.

2.3   Linkage analysis of the *Aga2* locus, and sequencing

The F_1 dominant ENU mutagenesis screen was conducted on the inbred C3HeB/FeJ (C3H; The Jackson Laboratory, USA) strain and has been previously described (140, 149). *Aga2* was backcrossed to wild-type C3H mice for five generations, and then outcrossed to C57BL/6J

(F_1) and then backcrossed to the outcrossed strain (N_2). Phenotype-positive N_2 progeny were tail genotyped with MS markers available at MGI (www.informatics.jax.org). The rough mapping panel consisted of 65 MS markers with clearly distinguishable polymorphisms between relevant strains, whereby the average interval between the markers was 20.1 cM. PCR products were gel electrophoresed through 3 % agarose or 12 % polyacrylamide gels and visualized by ethidium bromide staining. In order to narrow the candidate region not covered by the available MS markers, strain-specific SSLPs were identified within the region and properly submitted to MGI. Recombination fractions and map distances were calculated using Mapmanager QTX and modelled as an autosomal dominant disorder with complete penetrance. The thresholds for significant and suggestive linkage were set at LOD > 4.3 ($p < 0.0001$) and > 2.8 ($p < 0.0034$) respectively, and then rechecked by χ^2 statistics (w/ Yates correction). Ambiguous genotypes were treated as missing data. The candidate chromosomal region was evaluated using the Genomatix Software (Germany). Sequencing was performed at the Genome Analysis Center (Neuherberg Germany) using the ABI 3100 DNA sequencer (Applied Biosystems, USA) and the manufacturer's sequencing kit and protocols (BigDye® Terminator v3.1). All gene primers are available upon request.

2.4   Chromosomal and fine mapping of the *Ali34* locus

Ali34/+ mutants on the C3HeBFe/J background were mated with C57BL/6J female mice (Charles River, Germany). F_1 hybrid males were randomly backcrossed with C3HeBFe/J females. Positive N_2 offspring were phenotypically classified by the appearance of abnormal limbs. After sacrifice, tissue samples were collected for subsequent DNA isolation. Tail clip samples were incubated overnight with a lysis buffer consisting of 10 mM Tris-HCl (pH 8.0), 1 % (w/v) SDS, 50 mM EDTA, and 300 µg/ml Proteinase K (Sigma). Automated DNA extraction from the lysates was performed using the AGOWA Mag Maxi DNA Isolation Kit (AGOWA GmbH, Germany). DNA concentration was determined by absorption measurement at 260 nm. For linkage analysis a genome-wide mapping panel consisting of 138 SNP markers was applied (150, 151). Genotyping of this panel was performed using MassExtend, a MALDI-TOF high-throughput genotyping system supplied by Sequenom (San Diego, USA). Further MS and SNP markers were identified using MGI and tested within the *Ali34* chromosome 6 candidate region.

2.5   Genotyping *Aga2* and RNA/DNA preparation

Two distinct methods were developed to geneotype *Aga2* mice. First, a 231 bp PCR-product fragment containing the entire intron 50 of *Col1a1* was generated using the primers for-5'-ggcaacagtcgcttcaccta-3' and rev-5'-ggaggtcttggtggttttgt-3'. The amplification profile (temp./time(s)) was 94 ºC/20, 55 ºC/30, and 72 ºC/20 for 30 cycles. All PCR reagents were purchased from Fermentas GmbH (Germany). The PCR product was then completely cleaved using *Msp*A1I (NEB, Germany) according to the manufacturer's protocol, and gel analyzed. The second method was a more robust one-step touch-down PCR-based procedure for genotyping the *Aga2* SNP termed ARMS based on Ye et al. (2001) (152). The primers were constructed internalizing or spanning exon 50 of *Col1a1* such as: Forward inner primer (A mutant allele) 5'-tcctaccttggtaatgaccctctccccca-3', reverse inner primer (T wild-type allele) 5'-ccggtgtgactctggtgtgaatgaagtca-3', forward outer primer 5'-agggatccaacgagatcgagctcagagg-3', and reverse outer primer 5'-gagtttacacgaagcaggcagggccaat-3', all with a melting temperature of 73 ºC. A 1.6:10 molar ratio of outer to inner primers was used. The primers from the first strategy were used to detect heteroduplexes. For RNA and cDNA preparation, the RNeasy Micro and Mini kits (Qiagen), and the SuperScript™ first-strand synthesis system for RT-PCR (Invitrogen GmbH, Germany) were utilized respectively according to the manufacturers' protocols. For genomic yolk sac and tissue DNA preparation, the DNeasy tissue kit (Qiagen GmbH, Germany) was used.

2.6   Skeletal and radiological analysis

Skeletal preparations were generated as previously described (153). Simple and compound fractures were grossly examined. Compression fractures were evaluated via dissecting microscope. For µCT scans (Tomoscope 10010m; VAMP, Germany), image reconstruction and visualization were performed using the ImpactCB and ImpactView software (VAMP) respectively. Bone structure was delineated by 70 μm, whereby each scan lasted 15 minutes for 360 projections. A smaller view was chosen to minimize the effect of reconstruction voxel size on the spatial resolution. During each image build, the CT attenuation number was kept constant (HU1000). For pQCT analysis, the methods were performed as previously described (154). *In vivo* whole body BMC and BMD were assessed using the DXA Nordland Sabre scanner (Stratec Medizintechnik, Germany) with small animal software. Before each scan, the

animals were anesthetized via i.p. injection, weighed and set in a prone position. Only the peripheral skeleton was assessed with a 0.02 g/cm^2 histogram averaging width, and the equipment was routinely calibrated with the supplied QC phantom. The *in vivo* precision of the scanner was determined (i.e. by rescanning repositioned animals with recalibrations) and the coefficient of variance for BMC and BMD were 4.91 % and 1.60 % of the mean values. Different mice were analyzed at each age for the longitudinal studies. Calibration and standardization were performed appropriately.

2.7   DXA adjustments

The bone mineral parameters BMD and BMC are animal size dependent (155). One normalization method is based on linear regression weight models as described by Srivastava et al. 2003 (142) to assess the change in mutagenized F_1 BMD, BMC, and projected bone area using linear-phase baseline trait data from non-mutagenized animals. Linear regression models are only estimation tools and are prone to many errors, therefore caution was taken in the analysis. This procedure was also applied during the *Aga2* characterization in the GMC. Due to different animal facilities, 12- and 14-week-old control C3H mice ($n = 20$ per age per sex) were used for the estimation regression of bone parameter data for the mutagenesis screen. Meanwhile 6-, 9-, 12-, and 15-week-old control C3H mice ($n = 20$ per sex) were used for the baseline estimation regression model for the *Aga2* characterization from the GMC. *Aga2*/+ animals have a severe weight deficit, therefore earlier time points were included to obtain closer predictions.

2.8   Histology and histomorphometry

Sample preparation, (plastic) embedding and double labeling experiments were performed as previously described (156). In brief, mice were anesthetized (ketamine 100 mg/kg and xylazine 10 mg/kg) and perfused with 100 unit/mL heparinized saline followed by fresh 4 % PBS buffered paraformaldehyde (pH 7.4). Tissue were trimmed, eviscerated or kept intact, and then stored in fixative for 12 hours at 4 ºC. Samples were either processed for basic histology (paraffin) or dynamic histomorphometry. Bones were decalcified for 2 - 3 days in either 10 % formic acid (for HE) or 0.3 M EDTA pH 7.4 (for immunofluorescence and enzyme assays), dehydrated, and embedded in paraffin. For undecalcified sections, the methyl

25

methacrylate (MMA)-based Osteo-Bed bone embedding kit (PolyScience Inc., Germany) was used following the manufacturer's protocol. Sections of undecalcified bone were made using a heavy-duty microtome with a tungsten carbide knife and pressed using a slide compressor (Leica, Germany). Five-μm sections were used for fluorescent microscopy of the fluorochrome labels and for HE staining for evaluation of static parameters. For a subset of MMA-embedded samples, sections were stained with von Kossa and counterstained with Paragon solution. For the demonstration of endogenous ALP and TRAP, the procedure of Miao D, Scutt A. (2002) (157) was performed with modifications. Bone tissues were fixed for 12 hours in 80 % ethanol at 4 °C and decalcified using 0.3 M EDTA-G (pH 7.3) solution. After the sucrose washing steps, tissues were snap frozen, embedded in Tissue-Tek OCT (Sakura Finetek, The Netherlands) and sectioned (7 μm) using a cryostat microtome (Leica, Germany). Both ALP and TRAP activities were depicted using kits by Sigma (86R and 386A, respectively). All bone histomorphometric parameters were derived from the standardized nomenclature (158). The mineralizing surface (MS) was the sum of the lengths of double label (dL) and single label (sL) in a given sector. MAR was the distance between the dual labels where the time interval (7 days) was the referent. BFR was calculated by multiplying MAR by M.Pm/B.Pm % (calculated dL.Pm + 0.5 X sL.Pm/B.Pm). Non-sequential sections were collected every 70 - 100 μm. All images and measurements were captured and determined using the Axioplan 2 workstation (AxioVision v3.1; Zeiss, Germany) and the ImageJ program (v1.36; NIH, USA). Automatic color thresholding was applied to stacked image sets. Labels were traced with minimal operator bias. Between 6 - 20 repeated measurements were made per section using four non-sequential sections, where n (4 - 6) equals the number of animals examined.

2.9   SEM and TEM

SEM was performed as previously described (159). For TEM, lower dorsal skin were prepared as previously described (160). Cells with extensive vacuolation and dilated ERs were counted within a population of eight sections (30 - 40 total cells/section) from three different skin preparations ($n = 3$). 20 - 30 collagen fibril/fiber measurements were analyzed ($n = 3$). Measurements were made using the Soft Imaging System (Germany).

2.10   Clinical chemical and hematological analysis

The methods performed during the laboratory analysis have been previously described (161, 162). In brief, blood samples (300 µl) were taken from 12-week-old fasted (i.e. 12 hours) ether-anesthetized mice by retro-orbital sinus puncture with 0.8 mm Φ non-heparinized capillaries (Laborteam K&K, Germany), and collected in heparinized tubes (Li-heparin KABE, Germany). For hematological investigations, 50 µl of blood was collected in EDTA-coated tubes. Plasma was analyzed using the high-throughput Olympus AU 400 autoanalyzer. Calibration and quality control were performed daily according to the manufacturer's protocol. Whole blood samples were analyzed with an automated blood analyzer that was validated for the analysis of mouse blood (ABC-Blutbild analyzer; Scil Animal Care Company GmbH, Germany). Second blood samples were collected from a subgroup of previously tested mice at 17 weeks of age, whereby parameters only revealing genotype-specific differences were retested for reproducibility.

2.11   Collagen biosynthesis and Western analysis

Collagen synthesis was monitored in neonate dermal fibroblasts as previously described (163). Collagens were labeled with 2 µCi/ml L-[U-^{14}C]proline (250 mCi/mmol; Amersham, Germany), and then equi-amounts of medium were treated with protease inhibitors, precipitated using 25 % saturated ammonium sulfate and treated with pepsin (100 µg/ml in 0.5 M acetic acid). All samples were dissolved in electrophoresis sample buffer and resolved by 5 % (w/v) SDS-PAGE under reducing conditions. Gels were processed for fluorography with Amplify (Amersham) using a phosphoimager. Cell layers were harvested, 20 µg of whole cell extracts were resolved, and blotted membranes probed with LF-67 (1:20). LF-67 recognizes pro-α1(I), pC-collagen, and fully processed collagen (α1(I)) chains, therefore capable of discerning the mutated *Aga2* isoforms as well. It does not recognize the α2(I) chain and it is not known to cross-react with other collagens. Blots were detected using the WesternBreeze chemiluminescent kit (Invitrogen). For caspase-12 and BiP detection, cells were lysed in RIPA buffer with protease inhibitors. Supernatants were analyzed using the NuPAGE® Novex gel system (Invitrogen). Procaspase-12 was probed using an antibody corresponding to aa 2 - 17, which is apart from any probable cleavage site between the prodomain and the p20

subunit. Thus, this antibody can detect the truncated products of procaspase-12 (inferred from Nicholson DW 1999 (164), and Nakagawa T, Yuan J 2000 (129)).

2.12   Primary osteoblast culture and cellular assays

OBs were prepared as previously described (165). Cells were plated at 2 X 10^4 cells/cm^2 for all experiments. OB differentiation was initiated via media exchange (i.e. α-MEM w/10 % FCS, 2 mM glutamine, 1 % pen-strep, 50 µg/ml ascorbic acid, 10 mM ß-glycerophosphate). A minimum of four calvarias/genotype were pooled representing an independent experiment (*n*) with four repeated measurements. OBs lysates were collected on ice (CelLytic M reagent; Sigma, Germany) from 24-well plates, centrifuged (13K rpm, 4 °C), and lysates separated from the nuclear pellet. The samples were either snap frozen or immediately processed for measurements. Protease inhibitors (e.g. protease inhibitor cocktail, PMSF) were added accordingly thereafter. From the collected samples, four main standardized assays were performed. First, DNA concentration was measured using the QuantiT dsDNA fluorogenic kit (Invitrogen, Germany) from 1 % SDS (v/v) dissolved nuclear pellets. Second, total protein concentration was determined using a BCA kit. Third, caspase-3/7 activity was measured using 20 µg lysate with 5 mM caspase-3/7 fluorogenic substrate (Ac-DEVD-AMC; Alexis Biochemical, Germany) dissolved in caspase activity buffer (10 mM HEPES, 220 mM mannitol, 68 mM sucrose, 2 mM NaCl, 2.5 mM KH_2PO_4, 0.5 mM EGTA, 2 mM $MgCl_2$, 5 mM pyruvate, 0.1 mM PMSF, 1 mM DTT, pH 7.4, protease inhibitors added fresh) at excitation 380 nm and emission 460 nm over time using a fluorometer. And fourth, ALP levels were monitored by dissolving lysates into ALP activity buffer (54 mM pNPP, 0.1 M glycine, 1 mM $MgCl_2$, 1 mM $ZnCl_2$, pH 9.6) and measuring absorbance at 405 - 650 nm over time (1 hour) at 37 °C. Separately, mineralization was quantified by establishing an alizarin red standard curve, and measuring dye release using 10% hexadecylpyridinium from OBs cultured in 6-well plates. For metabolic measurements, cells were incubated at 37 °C with MTT (5 mg/ml in medium, sterile filtered), lysed in an isopropyl/HCL-based solution and then measured using an enzyme-linked immunosorbent assay (ELISA) reader (Tecan Genios Pro, Germany) at 590 - 650 nm wavelengths for dye and reference correction respectively. For secreted acid-soluble collagen measurements, the dye-binding assay kit by Sircol (Biodye Science, UK) was utilized using culture medium. For all fluorescent-based assays, appropriate plasticware were utilized. Certain values were normalized to DNA or protein concentrations. For nodule characterization, samples were analyzed using the ImageJ software.

2.13 Crystal violet assay

Primary dermal explants and fibroblasts were prepared and cultured accordingly (163). Cells were seeded in 96-well plates at $1.5 \times 10^4/cm^2$ upon fourth passage. At designated time-points, the medium (α-MEM supplemented w/10 % FCS, 2 mM glutamine, 1 % pen-strep, 50 µg/ml ascorbic acid) was removed, wells washed and then the cells were stained and fixed with crystal violet solution (0.5 % [w/v] crystal violet, 8 % [v/v] formaldehyde, 0.17 % [w/v] NaCl, 22 % [v/v] ethanol to 100 ml ddH$_2$O) for 20 minutes at room temperature. This method assays the binding of crystal violet to cell nuclei, and provides a reliable cell count compared with a Coulter counter (166). Wells were thoroughly washed, air dried, solubilized with 100 µl methanol, and measured at 540 nm using an ELISA reader. Four individual explant preparations ($n = 4$) were analyzed with four technical replicates.

2.14 Indirect immuno-fluorescence and -histochemical, and TUNEL analysis

Cells were cultured on glass coverslips coated with poly-L-lysine, and appropriately stained. Criteria for positive and negative controls were set accordingly. For immunohistochemical analysis, sodium citrate (10 mM, pH 6.0 in microwave) and proteinase K (10 µg/ml, 37 °C) antigen retrieval methods were performed, and the Vectastain ABC kit (Vecta Labs, USA) utilized. Terminal deoxyribonucleotide transferase (TdT)-mediated dUTP-biotin nick end-labeling (TUNEL) assay was performed with kits by Boehringer Mannheim (Germany). For caspase-3 analysis, tissue sections were stained (1:1000) and thoroughly washed followed by incubation with Alexa 488-labled goat anti-rabbit IgG (H+L) secondary antibody (1:1000; Molecular Probes, Germany) for one hour. The tissue sections were washed, mounted using aqueous medium w/DAPI, and photographed under oil emersion. Four independent preparations ($n = 4$) were analyzed with repeated measurements. For cell culture, 300 - 400 cells were counted per image field. For *in vivo* caspase-3 analysis, a region 0.4 mm from the growth plate was analyzed, whereby 400 - 480 total cells were evaluated within set regions (i.e. magnification field).

2.15   qPCR

RNA and cDNA were prepared as previously described (167). RNA purity was determined as the $A^{260/280}$ ratio with expected values between 1.8 and 2.0. qPCR was performed using the Roche LightCycler with primers (Table S8) and the QuantiTech SYBR green kit (Qiagen). For UPR analysis, the TaqMan® and ready-to use primers from Qiagen (QuantiTect primer assays) were applied. Primers were tested following standard guidelines (168). Dissociation curve, cycle thresholding and amplification efficiencies were analyzed as previously described (169, 170). Duplicate crossing points per marker were averaged per independent experiment ($n = 4$). Significance was depicted between time points. Values were normalized to levels of β-actin from the same pool for fold differences.

2.16   Cardiovascular screen

ECG was performed in a faraday cage on anesthetized (isoflurane/pressured air inhalation) mice using three metal bracelets on foot joints with electrode gel. The electrodes were positioned on the front paws and the left hind paw, resulting in the bipolar standard limb leads I, II and III, and the augmented unipolar leads AVF, AVR, and AVL. ECG was recorded for approximately seven minutes. Profile analysis of the ECG traces was performed with the ECG-auto software (EMKA technologies, France). In addition, the recordings were screened for arrhythmias, including supraventricular and ventricular extrasystoles, and conduction blockages. In the quantitative ECG analysis, sets of five analyzed beats were averaged for each animal (see Fig. S18 for an ECG trace template). The parameter Q-T interval was also corrected for the RR interval.

2.17   Lung function screen

Automated data analysis on whole-body plethysmography provided TV, f, MV, Ti and Te values at 10-second intervals using a commercially available system from Buxco® Electronics (USA). MEF was calculated from the ratio of TV and the respective time interval. sTV and sMV were calculated by relating the absolute values to body mass. Breathing was analyzed during phases of activity (i.e. exploration/grooming) and rest. Before each

measurement, the system was calibrated for barometric pressure, temperature, and humidity accordingly. Animals were measured between 8 A.M. and 11 A.M. for 40 minutes each.

2.18 Metabolic screen

Mice were individually caged for a period of 14 days on grid panels at an ambient temperature of 23 ± 1 °C (light – dark = 12:12 h, lights on 6:30 A.M. central European time) and received standard diet *ad libitum*. Mean BW was calculated weighing the mice every second day. E_{up} equals the energy content of food (18.5 kJ/g) multiplied by grams of food consumed per day and corrected for spillage. E_{met} subtracts energy content of feces and urinary energy loss (2 %; (171)) from E_{up}. E_{fec} was determined using bomb calorimetry (IKA Calorimeter C7000, Germany) collecting at 3-day intervals by drying lab chow and feces (~1 g) at 60 ° C for two days, homogenizing in a coffee grinder and squeezing to a pill.

2.19 Expression profiling screen

The methods applied have been previous described (172). In brief, four 15-week-old mutants and littermate controls ($n = 4$) each were sacrificed for organ collection. Animals were sacrificed between 9 and 12 A.M. by carbon dioxide asphyxiation. Total RNA (tRNA) from individual samples was obtained according to manufacturer's protocols using RNeasy Midi kits (Qiagen). tRNA aliquots were run on a formaldehyde agarose gel to check RNA integrity, and the concentration was calculated from $OD_{260/280}$ measurements. The RNA was stored at – 80 °C in RNase free water. Glass-surface DNA-chips containing ~21,000 probes were utlized. Roughly 20,200 of these probes were from the commercial Lion mouse array-TAG clone set (Lion Bioscience, Germany), derived mostly from 3' UTRs. In total eight chip experiments from four independent *Aga2* biological lung samples were performed and analyzed in reference to a pool of ten control individuals. Each sample was analyzed in two experimental replicates including two dye swap experiments. If differential gene expression was detected between mutant and control mice, additional wt/wt (pool) experiments were performed. By this approach it was possible to distinguish inter-individual variation of reference individuals that was relevant to a mutant. For labeling, 20 µg of tRNA was used for reverse transcription and indirectly labeled with Cy3 or Cy5 fluorescent dye according the TIGR protocol (173).

Labeled cDNA was dissolved in 30 µl hybridization buffer (6x SSC, 0.5 % SDS, 5x Denhardt's solution and 50 % formamide) and mixed with 30 µl of reference cDNA solution (pool from five control animals) labeled with the second dye. This hybridization mixture was placed on a pre-hybridized microarray under a cover slip, placed into a hybridization chamber (Genetix, Germany) and immersed in a thermostatic bath at 42 °C for 16 hours. After hybridization, slides were washed in 40 ml of 3x SSC, 1x SSC and 0.25x SSC at room temperature. Dried slides were scanned with a GenePix 4000A microarray scanner and the images were analyzed using the GenePix Pro3.0 image processing software (Axon Instruments; California, USA).

2.20 Alendronate treatment

At one week of age, LM control and *Aga2*/+ offspring were each randomized into two subgroups (eight mice per group) to receive weekly s.c. injections of alendronate sodium trihydrate (Sigma) at a dose of 0.03 mg/kg/day or saline in an equal volume of 0.1 mL/10 g body weight. Mice were weighed weekly for adjustment for dosage and tracking of weight gain. Pups were weaned from their mothers at three weeks of age, and male and female pups separated. The infant pups were treated from one to 18 weeks of age, at which time the mice were killed via carbon dioxide.

2.21 Statistics and database

Differences were estimated by two-way analysis of variance (ANOVA) on the influence of factors genotype and sex, and subsequent pairwise mean comparisons were performed by the *post hoc* (Student-Neuman-Keuls) test. Level of significance was set at $p < 0.5$. For all animal studies, n = number of animals investigated. In the ageing studies, overall survival was defined from the time of weaning until death of the mice. Censored events were stated accordingly. Univariate comparisons of Kaplan-Meier survival curves were performed using the logrank test. Analysis of covariance (ANCOVA) was performed with body mass as a covariate for weight-dependent parameters. All statistics were calculated using the Prism 4 (GraphPad, USA) and SigmaStat v. 3.1 (Systat Software, Germany) software programs. For array analysis, normalization of the raw experimental data was performed using TIGR Microarray Data Analysis System (MIDAS (174)) applying Locfit (LOWESS) normalization

and flip dye consistency checking as statistical methods (175). In brief, expression data were normalized performing a total intensity normalization to transform the mean log2 ratio to zero. To eliminate low-quality array elements, several filtering methods were applied that included: background checking for both channel with a signal/noise threshold of 2.0, one bad tolerance policy parameter and flip dye consistency checking (176). Identification of significantly differential expressed genes was performed using TIGR MultiExperiment Viewer (MEV). Significance Analysis of Microarrays (SAM) identified genes with statistically significant changes in expression by assimilating a set of t tests (177). Each gene was assigned a score (i.e. relative difference) on the basis of its change in gene expression relative to the standard deviation of repeated measurements for that gene. Genes with scores greater than a 0.4 threshold were deemed potentially significant. To estimate the false discovery rate, nonsense genes (i.e. less than 10 % of the selected genes) were identified by analyzing permutations of the measurements.

3.   Results

3.1   *Aga2* (<u>a</u>bnormal <u>ga</u>it 2)

3.1.1   Connective tissue phenotypes and responses

3.1.1.1 F_1 dominant musculoskeletal screen and positional cloning of *Aga2*

The original *Aga2* mouse was identified in the Munich ENU dominant mutagenesis screen, whereby at five weeks of age displayed an abnormal gait among the F_1 mutagenized progeny, and lowered DXA parameters at 16 weeks of age (Fig. S5). Genetic mapping of the *Aga2* locus was performed following the standard outcross-backcross breeding strategy. In all, 16 N_1 carriers were backcrossed to C57BL/6J animals and yielded 456 N_2 offspring. From the 456 offspring, 45 % (84 male, 120 female) were affected while 55 % (131 male, 121 female) were normal, whereby the skewed χ^2 distribution ($\chi^2 = 5.05$, $p < 0.05$, df = 1) represented, for the most part, the lethal nature of the *Aga2* locus. Moreover, the larger percentage of affected animals suggests a strong modifier effect on the outcross strain (compare Tables 1 and 2). Genome-wide segregation analysis was conducted with 30 affected N_2 animals using microsatellite (MS) markers (Fig. 11A). Significant *Aga2* linkage was observed on the distal end of mouse chromosome 11, whereby LOD (log of odds ratio) scores indicated that for all markers except those on chromosome 11, the recombinant fraction was roughly 0.5. Upon high-resolution haplotype analysis using 195 affected individuals, the *Aga2* locus was tightly linked to *D11Lis1* (0 crossovers), and situated within a ~1 cM (700 kb) region flanked by *D11Mit288* and *D11Lis2* (Fig. 11B).

3.1.1.2 Identification and characterization of the *Aga2* mutation

Within the *Aga2* candidate region, two skeletal genes were identified, *Col1a1* (procollagen type I, alpha 1; MGI 88467) and *chad* (chondroadherin; MGI 1096866), which share a conserved synteny on human chromosome 17 (17q21.33). Both candidate genes were

Figure 11. Genetic mapping of *Aga2*
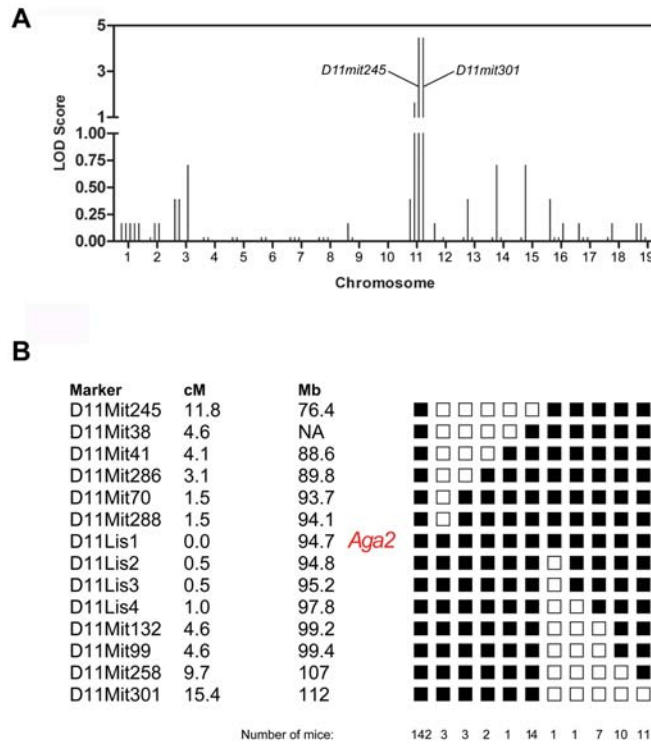
(Fig. 11) Genome-wide linkage and high resolution haplotype analysis of the *Aga2* locus. *A*, genome-wide linkage analysis revealed *Aga2* linkage on mouse distal chromosome 11. *B*, haplotype analysis identified the most probable *Aga2* candidate region (red) between *D11Mit288* and *D11Lis2*. Centimorgan (cM), megabase (Mb), and ■ heterozygous (C3HeB/FeJ & C57BL/6 alleles), □ homozygous (C57BL/6 allele)

sequenced, whereby a novel T to A transversion mutation within intron 50 of *Col1a1* (IVS50-18T>A) was identified (Fig. 12A scheme and chromatogram). The region entails the fibrillar C-domain of col1a1 (InterPro: IPR000885). Moreover, mouse strains CAST/EI, BALB/ByJ, 129X1/SvJ, AKR/J, and C57BL/6J were sequenced for potential *Aga2* polymorphisms, and each were homozygous for the wild-type T allele (data not shown). The *Aga2* substitution generated a novel cryptic 3' splice acceptor site, and predicted a terminal frameshift beyond the endogenous stop (Fig. S6).

The mutation was further confirmed at the genomic level through segregation analysis and a genotyping methodology. First, the *Aga2* line was maintained on the C3HeB/FeJ background for > 5 generations to dilute any potential ENU-induced silent mutations, and to show derivation from one mutational event. Moreover, the T to A exchange disrupted the endogenous *Msp*A1I restriction site, generating a cleavage-resistant allele in *Aga2/+* samples (Fig. 12B). On the transcript level, cDNA from affected calvaria revealed heteroduplexes and presence of the 16 bp cryptic alternative splice transcript. Homozgous embryos depicted

35

Figure 12. The C-propeptide *Col1a1*^{Aga2} mutation
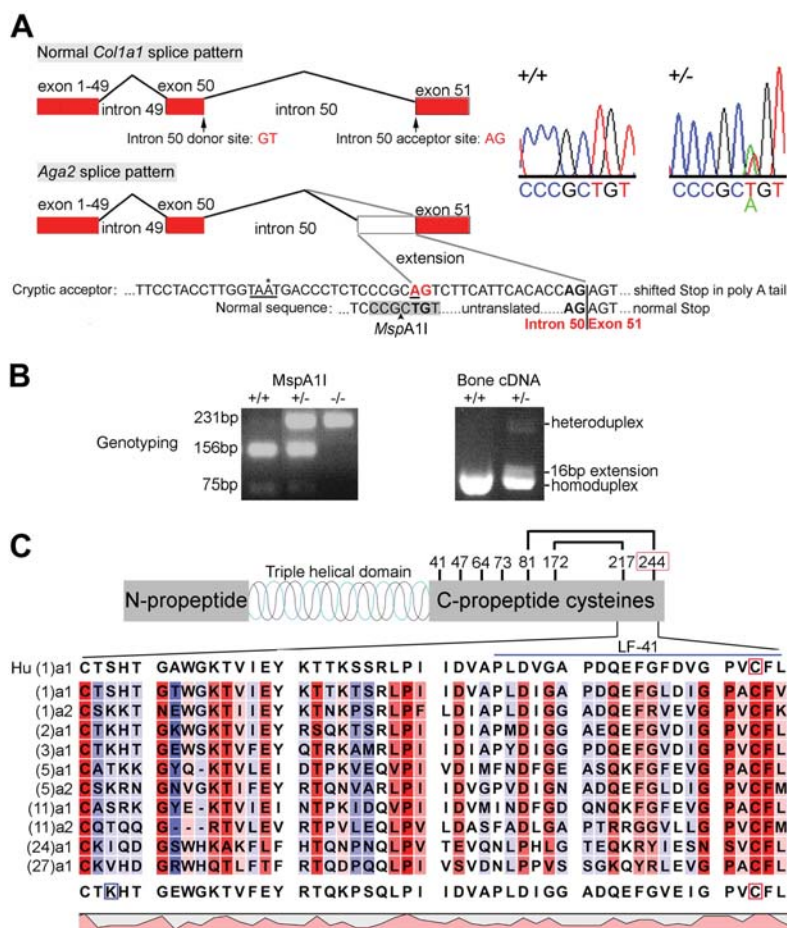
(Fig. 12) The *Aga2* mutation. *A*, the T to A transversion splice accepter mutation within intron 50 of the *Col1a1* gene. Splicing can occur either at the endogenous acceptor site (scheme, top gray line), or at the cryptic site (sequence, AG red highlight). The TAAT domain (underline) harbors a putative spliceosome branch site (*). *B*, genotyping of *Aga2* and presence of the alternative splice transcript. *C*, alignment of terminal C-propeptide ends of all major fibrillar collagens. Regions of conservation are in shades of red, while non-homologous regions are in blue. Start of exon 51 is boxed in blue. The frameshifted cysteine is boxed in red. The LF-41 recognition sequence is marked in blue. All sequences were retrieved from the MGI and NCBI databases. Alignments were made using the CLC Workbench software (v3.2.1). See Fig. S6 for the entire frameshift sequence.

predominate usage of the alternative spice site (data not shown). The data suggests the ability of the splicing machinery to efficiently discriminate the novel splice site in *Aga2*.

The C-terminal portion of all major fibrillar collagens were aligned highlighting specific residues of importance (Fig. 12C). Of interest, the most terminal conserved cysteine C244 (aa 1451) was ablated in the *Aga2*. Moreover, 48 endogenous amino acids including the stop were frameshifted, concomitantly predicting 89 new amino acids beyond the termination position into the poly A cleavage site (Fig. S6). Additionally, five new cysteines and a potential *N*-linked oligosaccharide (*CHO*) attachment site were introduced. The predicted

molecular weight (MW) of the *Aga2* pro-α1(I) chain is 149 kDa with a pI of 7.5. The secondary structure of the *Aga2* product was predicted to remove the hydrophobicity of the short loop formed by the last intra-chain disulphide bond (Fig. S7-9).

3.1.1.3 *Aga2* postnatal and embryonic lethality

The *Aga2* progeny derived from different breeding schemes were characterized. *Aga2* males have general reproductive success, and the mutation segregated in a dominant manner with complete penetrance (Table 1). *Aga2*/+ females produced smaller litter sizes due to a large reduction in body size. Reverse breeding generated no comparable litter size change arguing against intrauterine lethality. Likewise, regardless of the heterozygous-to-wild-type mating direction, no significant changes in χ^2 distribution were observed in the postnatal progeny. Paternal and maternal-derived *in utero* (E19-21) lethality in *Aga2* was studied, whereby among four litters no dead embryos were identified (12 wt:14 het, $\chi^2 = 0.04$; and 6 wt:11 het, $\chi^2 = 0.04$ $p > 0.05$, respectively). These results suggest *Aga2*/+ animals die during the postnatal period. A large subset of *Aga2*/+ animals succumbed to postnatal lethality (Table 2). All *Aga2*/+ lethals presented severe bone deformities and fractures. *Aga2*/+ *inter se* matings yielded non-Mendelian ratios for dominant inheritance suggesting embryonic lethality. Various embryonic stages were investigated to determine gestational arrest in *Aga2* homozygotes (Table S5). Homozygous lethality was estimated to occur between embryonic days 8.5 - 11 *post coitus*.

Table 1. Semi-dominant mode of inheritance in *Aga2*

Mating			Breeding Pairs	Offspring [♂/♀]	Litter Size [mean ± SD]	Postnatal Progeny[1]				χ^2
						Male		Female		
Female	X	Male				wt	het	wt	het	
C3H	X	C3H	15	51/50 (101)	6.9 ± 0.20	51	-	50	-	0.00
Aga2/+	X	C3H	18	48/51 (99)	5.4 ± 0.51*	23	25	22	29	0.65; df = 1
C3H	X	*Aga2*/+	14	45/55 (100)	7.1 ± 0.42	19	26	26	29	0.81; df = 1
Aga2/+	X	*Aga2*/+	4	10/7 (17)	4.3 ± 0.54*	3	8	2	5	6.76; df = 2; *p* = 0.5
							no homozygous			

[1] Genotyped after weaning using all collected animals. Ambiguous samples (e.g. unknown sex; *n* = 3) were not considered in both Tables 1 and 2. * *p* < 0.01 Student t test vs. C3H. C3H (C3HeB/FeJ)

Table 2. Postnatal lethality in *Aga2*

Mating			Nr. Postnatal Lethals to Weaning[1]				Logrank Test[2]	
			Male		Female		χ^2	p
Female	X	Male	wt	het	wt	het		
Aga2/+	X	C3H	3 (13 %)	15 (60 %)	1 (5 %)	20 (69 %)	26.89, df = 3	< 0.0001
C3H	X	*Aga2*/+	2 (11 %)	11 (42 %)	3 (12 %)	17 (58 %)	16.28, df = 3	0.001

[1] Total progeny derived from Table 1. Censored animals are featured in Table 1.
[2] Tested for sex and genotype distribution. C3H (C3HeB/FeJ)

3.1.1.4 *Aga2* skeletal and growth phenotypes

Among *Aga2*/+ animals, the gross skeletal phenotype was discernable between days 3 - 11 after birth. Heterozygous animals that survived to adulthood were extensively characterized and classified as moderately-to-severely affected, and displayed the hallmark diastrophic limb(s), severe fractures, body composition changes, and generalized decreases in DXA-based bone cross-sectional parameters (Fig. 13A-D and Table S6). Hearing impairments (via clickbox) were not observed in *Aga2* animals up to 30 weeks of age. In contrast, lethal animals developed scoliosis, precocious hemorrhaging at joint cavities and intracranial sites, provisional rib and long bone calluses, severe body size deficit, *pectus excavatum*, gasping, platyspondyly, edema of the eyes, greasy skin and eczema (Fig. 13E). Comminuted fractures incurred signifying the severe brittleness of *Aga2* bones characteristic of a type II OI phenotype (Fig. 14).

The effect of the *Aga2* mutation on volumetric bone mineral density (vBMD; mg cm^{-3}) and content (vBMC; mg) was evaluated in a subset of mice using *in vivo* peripheral quantitative computed tomography (pQCT; Table 3). In *Aga2* distal femora, trabecular and cortical vBMD within the metaphysis were substantially decreased compared to controls (32 % and 15 % respectively). vBMD was also significantly reduced within the diaphysis at the respective bone structures (20 % and 8 %). Cortical vBMC was markedly diminished in both the metaphysis and diaphysis in *Aga2* (47 % and 41 % respectively). In contrast, the trabecular vBMC in both regions were unchanged due to enlarged medullar areas (see below). The diminished trabecular vBMD in *Aga2* largely represented the paucity in trabecular number as determined independently (Table S7). Moreover, the metaphysial subcortical area in *Aga2* was significantly decreased by 37 %, while the trabecular area was comparatively increased by 37 %. The diaphysial cortical area was decreased by 36 %, yet the trabecular area was increased by 52 %. Furthermore, the calculated trabecular area *versus* total bone area

Figure 13. *Aga2* skeletal and growth abnormalities
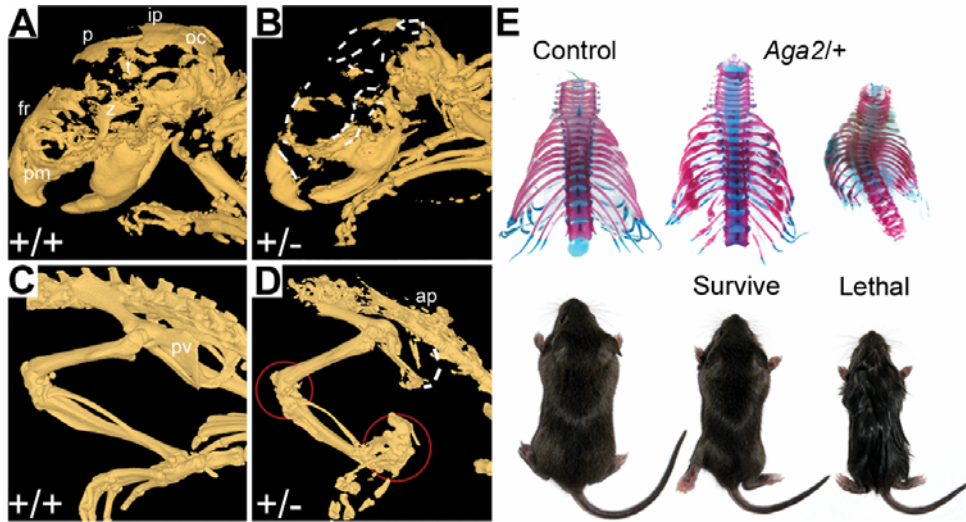
(Fig. 13) Morphometric and indirect mineral assessment of *Aga2* animals. *A* and *B*, cranial and craniofacial features of 16-day-old male mice were evaluated via microcomputed tomography (μCT). *C* and *D*, lateral μCT views of 12-week-old male skeletons highlight the axial vertebrae, pelvis (white trace), and hind limb (encircled) defects in *Aga2*. *E*, young *Aga2/+* animals (< 3 weeks) feature provisional-bony rib calluses and severe overall growth defects. Temporal (t), occipital (oc), parietal (p), frontal ridge (fr), premaxillar zone (pm), zygomaticum (z), articular process (ap), pelvis (pv)

Figure 14. OI type II skeletal phenotype in *Aga2*
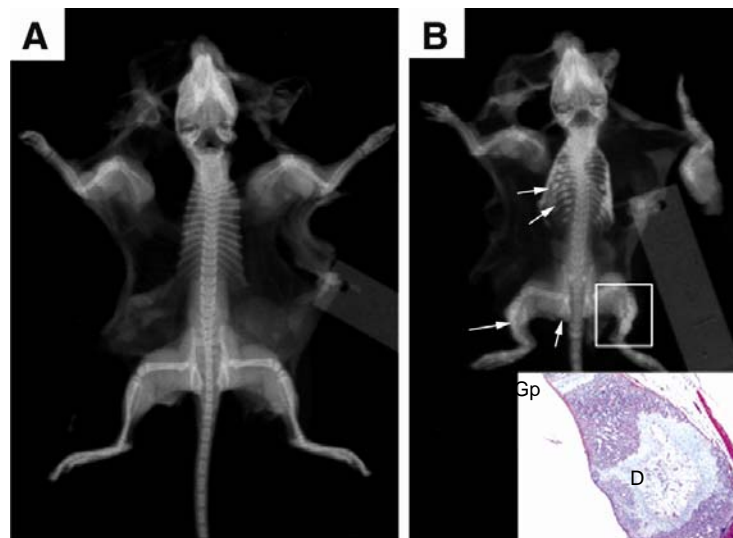
(Fig. 14) Radiological analysis: callus formation after fracture. In *A*, a wild-type 15-day-old skeletal radiograph is depicted. In *B*, age-matched severely affected *Aga2/+* animal shows excessive deformities, a deteriorated pelvis, and rib and long bone calluses throughout the skeleton (arrows). Boxed region in *B* depicts the mechanically unstable repair blastema (i.e. consisting mainly of MSCs differentiating into cartilage) located at the tibial diaphysis (D). Growth plate (Gp)

Table 3. *in vivo* pQCT analysis in paternal-derived 16-week-old male femur

Parameter & Region	Bone	Control (n = 6)	*Aga2*/+ (n = 6)	Student t test
vBMD (mg cm⁻³)				
Metaphysis	Trabecular	296.4 ± 4.46	200.5 ± 7.25	p < 0.0001
	Cortical	856.8 ± 6.20	725.5 ± 17.34	p < 0.0001
	Total	699.1 ± 8.22	451.1 ± 15.20	p < 0.0001
Diaphysis	Trabecular	216.0 ± 4.62	172.6 ± 6.14	p < 0.0001
	Cortical	1302 ± 2.73	1198 ± 9.94	p < 0.0001
	Total	1034 ± 10.35	816.8 ± 16.32	p < 0.0001
vBMC (mg)				
Metaphysis	Trabecular	0.34 ± 0.02	0.30 ± 0.04	p = 0.116
	Cortical	1.95 ± 0.04	1.04 ± 0.06	p < 0.0001
	Total	2.28 ± 0.04	1.36 ± 0.06	p < 0.0001
Diaphysis	Trabecular	0.06 ± 0.01	0.07 ± 0.04	NS
	Cortical	1.79 ± 0.06	1.05 ± 0.06	p < 0.0001
	Total	2.02 ± 0.06	1.29 ± 0.07	p < 0.0001
Area (mm²)				
Metaphysis	Trabecular	1.15 ± 0.05	1.56 ± 0.06	p < 0.0001
	Cortical	2.27 ± 0.04	1.43 ± 0.07	p < 0.0001
	Total	3.41 ± 0.07	3.01 ± 0.08	p < 0.001
Diaphysis	Trabecular	0.25 ± 0.04	0.38 ± 0.04	p < 0.0001
	Cortical	1.38 ± 0.04	0.88 ± 0.05	p < 0.0001
	Total	1.96 ± 0.06	1.58 ± 0.07	p = 0.002
Circumference (mm)				
Diaphysis	Periosteum	6.54 ± 0.07	6.14 ± 0.08	p = 0.0008
	Endosteum	5.04 ± 0.08	5.41 ± 0.10	p = 0.009

(Table 3) Values represent mean ± SEM, where *n* = 6 animals combining left and right femora. vBMD (volumetric bone mineral density), vBMC (volumetric bone mineral content), NS (not significant)

percentage at the metaphysis was 33.5 ± 1.0 % for control and 52.6 ± 1.6 % for *Aga2*, and a similar trend was observed at the diaphysis. The calculated cortical area *versus* total bone area percentage at the diaphysis was 87.0 ± 0.8 % for control and 55.7 ± 1.3 % for *Aga2*. The calculated diaphysial cortical BV/TV % (bone volume/total bone volume) was decreased by 21 % in *Aga2* (70.7 ± 0.1 % control and 55.6 ± 0.1 % *Aga2*/+). In addition, the *Aga2* periosteal circumference was significantly reduced by 7 %. In contrast, the affected endosteal circumference was elevated by 7 %. The endosteum circumference represented 88 % and 77 % of the periosteum in *Aga2* and control, respectively, suggesting elevated resorption. Lastly, all the trends observed in the pQCT and static histomorphometric analysis were preliminarily confirmed using μCT analysis (Fig. S10). Collectively, these results suggest potential defects in mineralization and/or bone formation.

3.1.1.5 Steady longitudinal decrease in weight, BMD and BMC in *Aga2*

The OI type and bone metabolic defects within *Aga2* were further evaluated and judged during long-term DXA time course studies. The weight, and BMC and BMD in a longitudinal study from ~6 (1.5 months) to 76 (19 months) weeks in age were investigated in order to identify potential late-onset effects (e.g. osteoporosis) due to the *Aga2* mutation (Fig. 15). The rate of weight gain appeared steady between 12 – 21 weeks of age within both sexes of each genotype. In contrast, *Aga2* mice of both sexes were ~48 – 57 % ($p < 0.001$ *post hoc*) decreased in weight compared to age-matched littermate controls throughout the entire time course study. Although BMC and BMD within both genotypes depicted similar trends as in weight (i.e. increasing between 12 and 21 weeks during the active growth period), both parameters in *Aga2* gained less rapidly during this period compared to controls. A sustained ~77 % decrease ($p < 0.001$ *post hoc*) in BMC was depicted in *Aga2*/+ mice, while a ~38 - 43 % ($p < 0.001$ *post hoc*) reduction in BMD was observed maintained throughout adulthood. In both sexes at all time points, the calculated Z-scores (i.e. Δ standard deviation) for *Aga2*/+ BMC and BMD were > 3 and > 6.5 below respective age-matched control values (data not shown). Additionally, all calculated BMC and BMD T-scores (i.e. the Δ standard deviation referencing 16-week-old control) for *Aga2*/+ mice were > 5 below the reference, further suggesting consistently lowered bone parameters over the entire time course study (data not shown). Lastly, to better understand the relationship between the bone parameters and weight change in *Aga2*, the differences in BMD and BMC between control and *Aga2*/+ mice were tested via analysis of covariance (ANCOVA) with weight as a covariate. For example at 16 weeks of age, *Aga2*/+ animals were shown to be significantly different from littermate controls (BMD genotype $p = 0.010$; BMC genotype $p = 0.007$). These results indicate that the decrease in BMD and BMC in *Aga2* is not merely due to diminished body mass, but due to anomalies in mineralization and/or bone formation. These results clearly show that the *Col1a1* gene defect sustained a strong skeletal phenotype through the life cycle in *Aga2*.

Figure 15. Longitudinal analysis using DXA
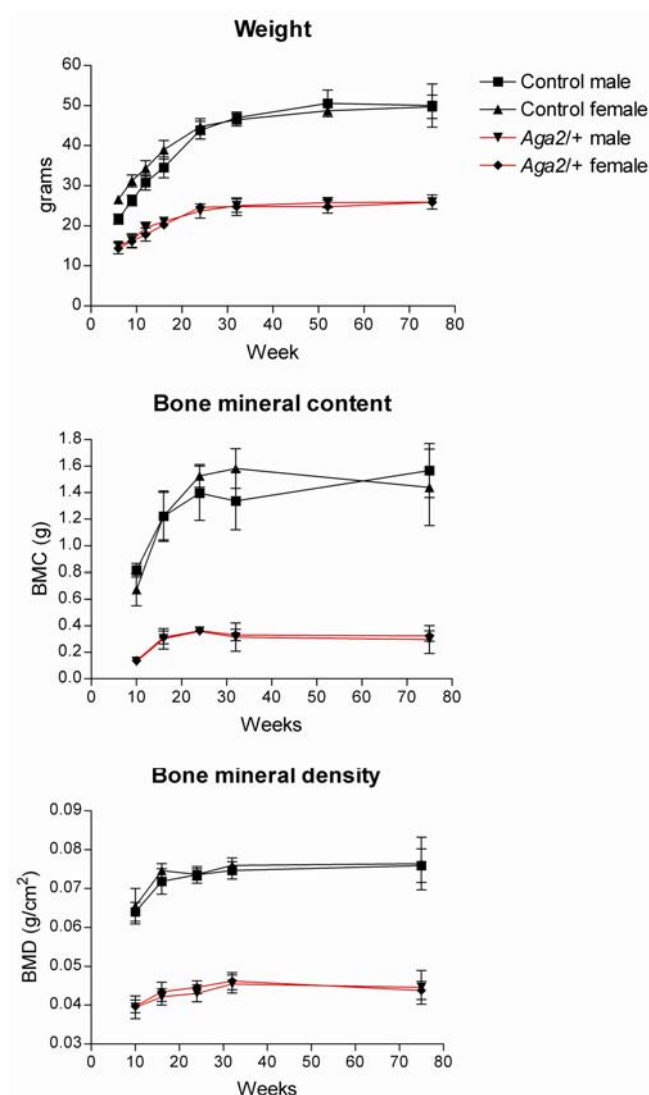
(Fig. 15) Long-term weight, BMC and BMD analysis of *Aga2* mice. *Aga2*/+ animals of both sexes per age group (*n* = 8) showed significant differences between control within all parameters throughout the entire longitudinal study (*p* < 0.001 ANOVA). Age-matched control littermates were included. Analysis of covariance with weight selected as the covariate is depicted in the text. Plots represent mean ± SD as error bars.

3.1.1.6 Increased mortality in aged *Aga2*/+ mice

The burden of the identified systemic responses (see later) to defective type I collagen was examined in survival analysis using aged *Aga2* mice (Fig. 16). Analysis of the survival curves revealed lowered survival in *Aga2*/+ mice compared to littermate controls which lasted the entire duration (*p* = 0.001 Logrank test). The reduction in life span was found to be more

Figure 16. Aging effect in type OI-III/IV *Aga2* mice
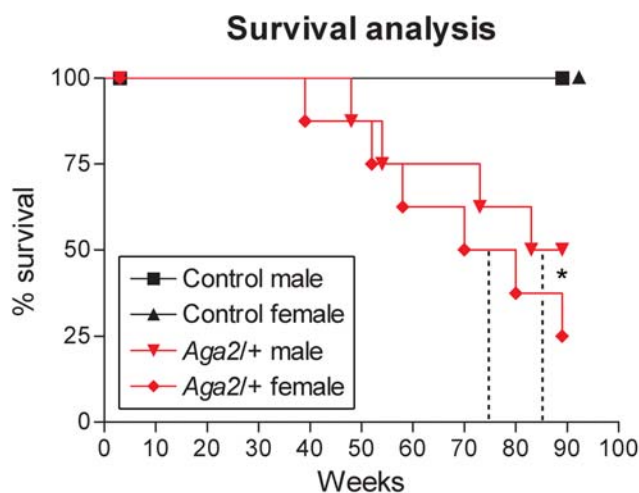
(Fig. 16) Kaplan-Meier survival analysis of *Aga2* mice. Data represent groups of eight mice per sex and genotype monitored for health from weaning until 89 weeks. Censored subjects at the end of the study were eight for each control group, and four and two for *Aga2*/+ male and female groups respectively. Survival curves were compared using the Logrank test (*$p = 0.001$).

profound in the female population. The median survival for *Aga2*/+ males was 85 weeks, while affected females had a median survival of 76 weeks in our study. Among the non-censored female mice which died during the study, four among six animals were malignant, and developed large tumors localized to the trunk region. For health reasons, these animals were sacrificed and two animals were sent to pathology for histological analysis (data pending). These results in conjunction with the DXA longitudinal studies suggest the compromise of multi-organ systems in contributing to the increased mortality rate induced by the gene defect in *Aga2* animals. Collectively, the longitudinal DXA studies and radiological evaluation (i.e. deformities) depict surviving *Aga2* as moderately affected with type IV OI clinical features. The aging study depicted *Aga2* animals as progressively deteriorating, therefore it was concluded that surviving *Aga2*/+ animals have overlapping clinical features of type III and IV OI.

3.1.1.7 Clinical chemical and hormone analysis

Several biochemical and hormonal markers within serum were evaluated to better understand the bone metabolic defects in *Aga2* (Table 4). A major elevation in total alkaline phosphatase (ALP) levels was detected in 12-week-old *Aga2*/+ samples compared to littermate controls (167 % male and 106 % female). Osteocalcin levels were significantly increased in both sexes

Table 4. Clinical chemical analysis at 12 - 16 weeks of age

Parameter	Control (A)		Aga2/+ (B)		Pairwise		ANOVA		
	Male	Female	Male	Female	A-B Male	A-B Female	Genotype	Sex	Interaction
Bone Turnover	(*n* = 15)		(*n* = 15)						
Calcium [mmol/l]	2.08 ± 0.03	2.23 ± 0.01	2.20 ± 0.02	2.21 ± 0.02	***	NS	**	*	*
ALP [U/l]	89.70 ± 2.73	137.90 ± 2.29	239.60 ± 8.91	283.39 ± 13.13	***	***	***	***	NS
	(*n* = 6)		(*n* = 6)						
TRACP 5b [U/l]	1.93 ± 0.04	2.02 ± 0.04	2.50 ± 0.04	2.40 ± 0.03	***	***	***	NS	NS
Osteocalcin [ng/ml]	226.77 ± 3.64	240.08 ± 3.76	374.20 ± 4.88	381.70 ± 5.15	***	***	***	NS	NS
Hormone[1]	(*n* = 5)		(*n* = 5)						
PTH [pg/ml]	127.30 ± 12.69	107.00 ± 8.21	159.00 ± 8.32	142.40 ± 4.57	*	*	**	NS	NS
Calcitonin [pg/ml]	31.56 ± 3.26	34.40 ± 2.59	51.26 ± 3.92	74.32 ± 8.12	*	***	***	*	NS

[1] Measured at 16 weeks of age
Data presented as mean ± SEM. *$p < 0.05$, **$p < 0.01$, ***$p < 0.001$
Tartrate-resistant acid phosphatase 5b (TRACP 5b), parathyroid hormone (PTH), not significant (NS)

in *Aga2* (66 % male and 59 % female). Circulating TRACP 5b (i.e. a marker for OCs) was significantly elevated in *Aga2* (32 % male and 19 % female). Furthermore, a subtle transient increase in the total calcium level was detected only in male mutants (6 %; $p < 0.01$). No changes in inorganic phosphate levels were detected (data not shown). *Aga2* males and females depicted a significant 25 - 33 % increase in PTH levels. Furthermore, *Aga2* females yielded a 118 % increase in calcitonin, while a 64 % significant increase was observed in the male population.

3.1.1.8 Assessment of physiological bone growth and remodeling in *Aga2*

Bone formation and resorption were directly monitored *in vivo* using histomorphometric methods. A 47 % comparative increase in the number of endogenous OBs was noted in *Aga2* samples (Fig. 18A and S11). ALP-positive hypertrophic OBs were also localized to the surface periphery and embedded in mineralized bone. Dynamic histomorphometry depicted an increase in the *in vivo* double-labeled bone surface (MS/BS, mineralizing surface per bone surface) in *Aga2* (Figure 17A,C main; 12.1 ± 3.9 % control and 39.4 ± 5.2 % *Aga2*/+ respectively; $p < 0.001$ Student t test). In *Aga2*, deposition of immature woven bone was

Figure 17. *Aga2* skeletal and growth abnormalities
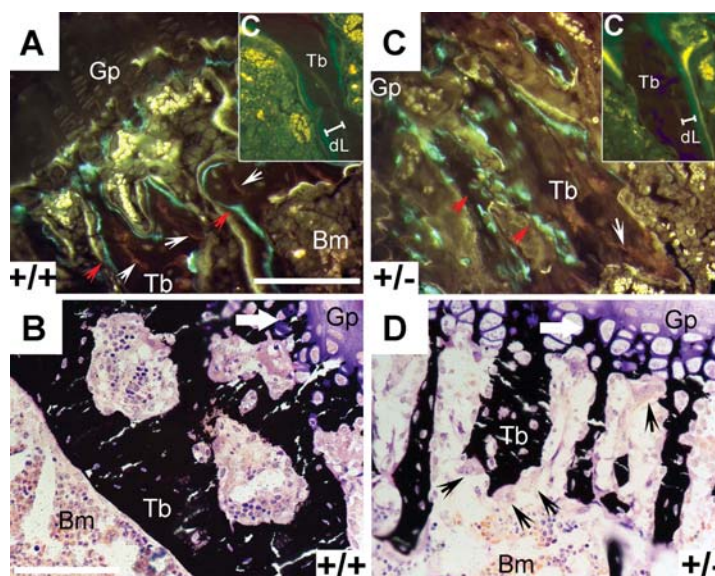
(Fig. 17) Micrographs of bone formation and resorption in 16-week-old male mice. *A* and *C*, bone formation and mineral accretion were monitored by dual calcein (red arrows) and tetracycline (white arrows) *in vivo* labeling (dL), whereby tibial secondary cancellous (C; inset) and endocortical (not shown) regions were characterized. *Bar*, 100 μm for main in *A* and *C* combined. Bracketed bars within the corner boxes represent mean ± SEM of sample dL lengths (17.9 ± 0.6 μm/7 days control and 11.7 ± 1.0 μm/7 days *Aga2*/+). *B* and *D*, undecalcified tibial sections in control and *Aga2*, respectively, depict increased resorptive bays with multinucleated OCs (black arrows) at the osteogenic zone, and extended hypertrophic zone of the growth plate (Gp; horizontal arrow) in *Aga2*. *Bar*, 100 μm combined; stained with von Kossa and countered with Paragon. Bone marrow (Bm), trabecula (Tb)

apparent and less striated compared to controls. The mineral apposition rate (MAR; matrix production per unit time) in both mid-cancellous and endocortical regions of the tibia were significantly reduced (Fig. 18B). The bone formation rate (BFR; a surrogate for OB activity) in *Aga2* was comparatively increased by 143 % (Fig. 18B), signifying overly active bone surfaces. A 35 % comparative increase in the number of tartrate-resistant acid phosphatase (TRAP)-positive OCs (OCs) was revealed in *Aga2* (Fig. 18C). Static histomorphometric analysis of both tibiae and femora confirmed marked negative changes depicted in the pQCT analysis (Table S7). Also, histological analysis of both *Aga2* femoral and tibial epiphysial plates revealed regions of abrogated ALP activity within hypertrophic chondrocytes (Fig. S12). The growth plate hypertrophic zone appeared extended in *Aga2* (Fig. 17D, horizontal arrow), whereby deviated epiphysial plates were commonly seen during histological preparations. Lastly, *Aga2*/+ mineralized bones were more cell-dense and loosely organized without cortical perforations (Fig. 18D).

Figure 18. Quantitative analysis of physiological bone growth and remodeling in *Aga2*
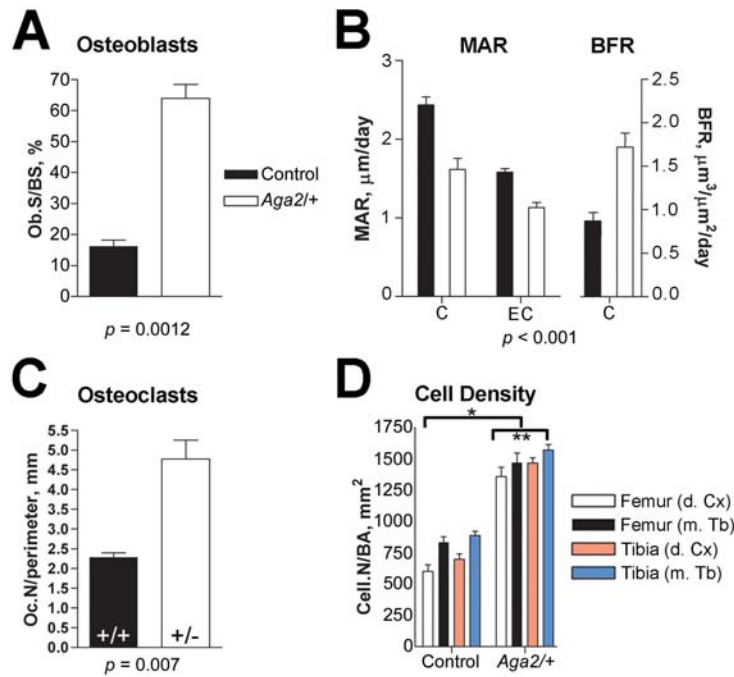
(Fig. 18) Static and dynamic histomorphometric measurements in 16-week-old male tibiae. *A* depicts the percentage of secondary trabecular surface encompassed with OBs. *B* depicts MAR calculated within both secondary cancellous (C) and endocortical (EC) bones, while BFR was calculated for mid-cancellous bones. *C* shows the relative number of TRAP-positive OCs within secondary trabeculae. *D* depicts hypercellularity within *Aga2* femora and tibiae. Bars represent mean ± SEM, where $n = 4$ in *A-C*, and $n = 6$ experiments in *D*. *p* values in *A-C* derived from the Student t test, while in *D*, *$p < 0.0001$ one-way ANOVA and **$p < 0.001$ *post hoc* test. Diaphysis (d), metaphysis (m), cortex (Cx), trabeculae (Tb), and ■ control, □ *Aga2*/+ for *A-C*

3.1.1.9 Bisphosphonate treatment

Bisphosphonates are a class of drugs commonly used on OI patients that inhibits osteoclast-mediated bone resorption. The potential anabolic effects of alendronate, a nitrogenous bisphosphonate family member, on 21-week-old treated male mice were examined (Fig. S13). The serum ALP measurements at 21 weeks revealed a significant ~33 % decrease in *Aga2*/+ treated animals. Control animals with or without alendronate showed no significant differences. Alendronate-treated *Aga2*/+ animals displayed a ~87 % increase in BMD compared to untreated *Aga2*/+ animals. There was a significant ~16 % BMD increase between alendronate-treated and untreated control animals. There was a ~211 % BMC increase in alendronate-treated *Aga2*/+ animals compared to control. A ~55 % BMC increase was reported in control animals treated with alendronate. These results show the positive anti-

resorptive effects of alendronate, and further confirm the pathological role of increased OC activity in the *Aga2* skeleton.

3.1.1.10 Collagen defects within *Aga2*

Evidence for type I collagen defects in *Aga2* connective tissues was sought (Fig. 19). Transmission electron microscopy (TEM) revealed alterations in the assembly of *Aga2* collagen fibrils based on the staggered striation pattern of Chapman's model (178). *Aga2* collagen fibrils depicted a 48-nm cross-striation pattern resulting in a 20 % comparative depreciation in the banding periodicity (59.2 ± 0.7 nm control and 47.7 ± 1.0 nm *Aga2*/+; $p <$ 0.0001 Student t test), and a 18 % decrease in fiber diameter (73.4 ± 0.7 nm control and 59.6 ± 0.6 nm *Aga2*/+; $p <$ 0.001 Student t test; Fig. 19A,E). *Aga2* dermis contained heterogeneous populations of fibroblasts with smaller nuclei, aberrant electron-dense ERs, lysosomes and empty autophagic-like vacuoles interspersed throughout the cells (Fig. 19F, inset). *Aga2* ER appeared dilated and less contiguous compared to wild-type cells (Fig. 19B). *Aga2* ERs appeared contiguous with secretory vesicle signifying the formation of ER associated compartments. The relative percentage of unhealthy dermal fibroblasts was significantly elevated in *Aga2* (2.8 % ± 0.6 control and 15.4 % ± 1.1 *Aga2*/+; $p <$ 0.0001 Student t test). Scanning EM (SEM) studies on cortical nanostructure of *Aga2* samples depicted an anti-parallel, less-densely packed network of collagen bundles when compared to controls (Fig. 19C,G). At higher magnifications, *Aga2* surfaces depicted thinner hydroxyapatite-laced fibers and microfractures predominantly situated near Volkman canals (Figure 19H, arrow heads).

The structural integrity of the dermal fibroblast ECM was further accessed in immunofluorescence studies (Fig. 20A,B). The relative number of cells featuring intact extracellular type I collagen was comparatively reduced in *Aga2* cultures, whereby *Aga2* cells intracellularly retained procollagen molecules instead (Fig. 20C). The EM observations were independently confirmed in radiolabeling experiments whereby *Aga2* affected fibroblasts specifically secreted less overall type I procollagens and exhibited a pro-α1(I):pro-α1(III) ratio near 1:1, compared to the 3:1 ratio in wild-type cells (Fig. 20D). Also in silver stain gel analysis, *Aga2* fibroblasts did not reveal proportional changes in secreted type I collagen chains (Fig. S14). Western analysis using antiserum LF-67 recognized type I procollagen, pC/N-collagens, and the fully processed collagen, and did not cross react with other collagens (Fig. 20E and S15). Wild-type samples showed processing of type I procollagens and isoforms to the ECM. In contrast, diminished levels of surface type I collagens with

Figure 19. Native collagen structure in 12-week-old dermis and cortical bones
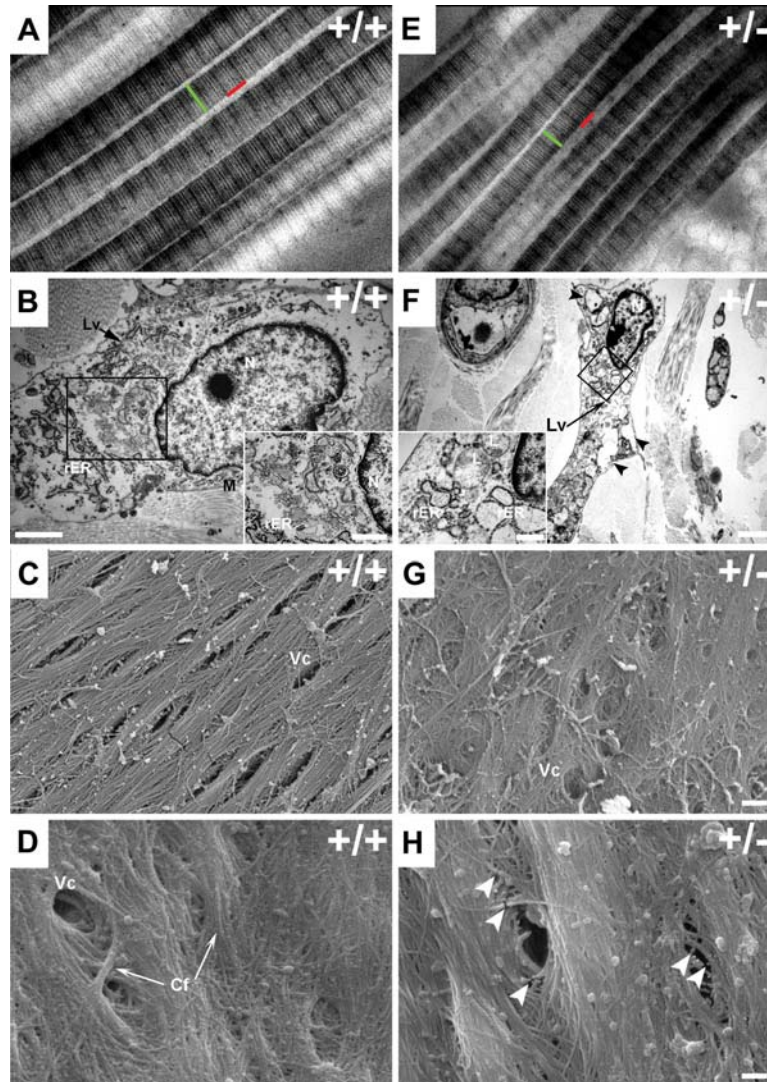
(Fig. 19) TEM and SEM analysis. *A* and *E*, TEM micrographs of longitudinally-sectioned dermis depict collagen fibrils with a banding periodicity of 60 nm in control and 48 nm in *Aga2* samples, respectively (100k X; red lines). The collagen fiber diameter is in green. *B* (*bar*, 2 μm; 6.4k X) and *F* (*bar*, 2 μm; 5k X) represent TEM micrographs of control and *Aga2* fibroblasts respectively. The ERs in *Aga2* are engorged (inset; *bar*, 500 nm; 40k X) compared to control (inset; *bar*, 1 μm; 20k X). Increased intracellular empty vacuoles (black arrow heads) and lysosomes (L) were present in *Aga2*. *C* and *G*, SEM of femoral endosteal surfaces depicts the arrangement of collagen bundle fibers (*bar*, 1 μm combined; 8k X). *D* and *H*, high magnification of collagen fibers (Cf) revealed microcracks in *Aga2* (arrow head; *bar*, 300 nm combined; 25k X). Lipid vesicles (Lv), mitochondria (M), rough endoplasmic reticulum (rER), Volkman canal (Vc)

concomitant increases in normal procollagen I isoforms (i.e. a dominant negative effect) were depicted within *Aga2* cells. Also, only in *Aga2* cells a slow-migrating collagenous specie was discriminated reasoned to be the mutated protein product. In addition, this low-present specie was more pepsin-insensitive, suggesting proteolytic resistance due to potential secondary structural changes. To further clarify the intracellular abnormalities indicated above, aberrant pro-α1(I) chains colocalized with an ER-resident protein, not to a *cis*-Golgi marker (Fig. S16).

Figure 20. Type I collagen defects in *Aga2*
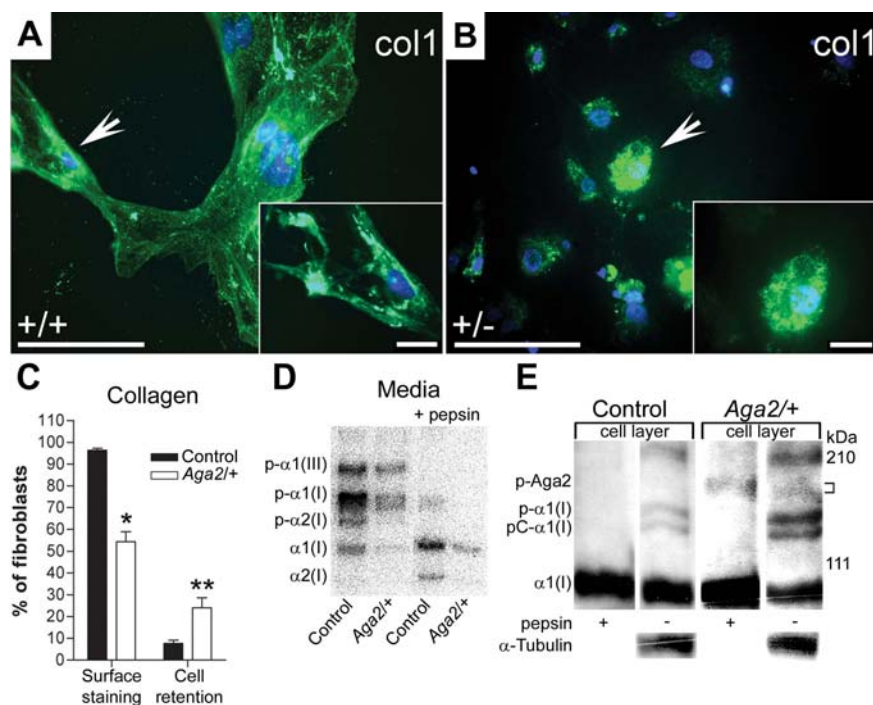
(Fig. 20) *In vitro* secretory and structural defects of *Aga2* pro-α1(I) and type I collagen in primary dermal fibroblasts. *A* and *B* depict type I collagen immunofluorescence, where boxed cells are designated by arrows. Cells were counterstained using both DAPI and ß-actin (not shown). *Bars*, 100 μm in *A* and *B* main, 20 μm in boxes. *C*, quantification of structural elements. Columns represent mean ± SEM, where $n = 4$ experiments (*$p = 0.0009$ and **$p = 0.02$ Student t test). *D*, procollagen biosynthesis via [^{14}C]proline radiolabeling. *E*, Western analysis using antiserum LF-67. Pepsin treatment and α-tubulin were used for specificity and loading purposes.

Also, immunostaining with antiserum LF-41, which only recognizes wild type α1(I) Chains due to its epitope, showed intracellular accumulation of procollagen molecules, further confirming the dominant negative effect of the mutation (Fig. S16B). In addition, vesicular structures were observed in *Aga2*/+ cells which likely represent proteasome structures (Fig. S16D). Based on our results, the *Aga2* mutation affected pro-α1(I) processing by blocking its ER-to-Golgi anterograde transport, thus inhibiting vesicular exocytosis to the matrix.

3.1.1.11   Enhanced *ex vivo* osteogenic activity and nodular defects in *Aga2*

The OB metabolic and functional phenotypes were further characterized utilizing the primary calvarial culture system. First, OB activity was studied by kinetically monitoring ALP levels, whereby a relative 91 - 56 % increase was observed until day 26 in *Aga2* (Fig. 21A). The

Figure 21. *Aga2* osteoblastic *ex vivo* response and function
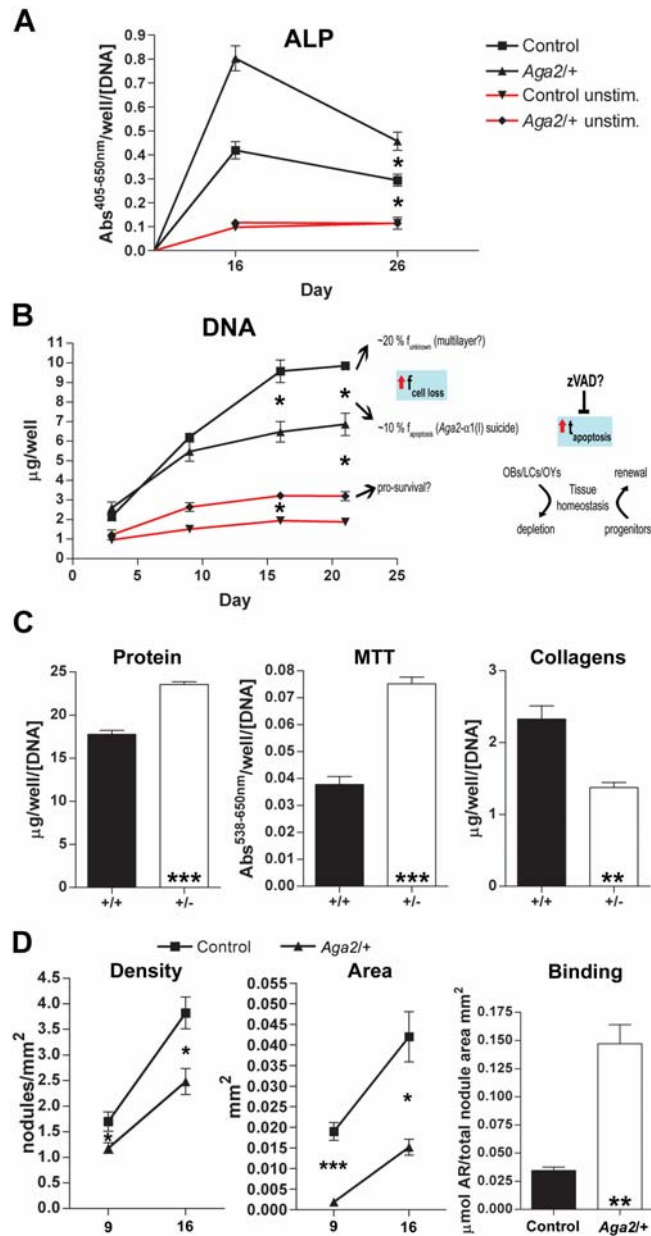
(Fig. 21) Characterization of *Aga2* OBs. *A*, ALP activity measurement in primary OB lysates. *B*, growth curve analysis. *C*, OB total protein, reduced MTT, and secreted acid-soluble collagen levels at 21 days in culture. *D*, time-course analysis of the density and individual area of bone-like nodules, and the amount of bounded alizarin red (AR) dye per total nodule area at day 16. Asterisks show significant differences at $*p < 0.05$, $**p < 0.001$ and $***p < 0.0001$ (Student t test), while stimulated-unstimulated p values were derived from ANOVA w/ *post hoc* test. Values represent mean ± SEM, where $n = 4 - 5$ independent experiments. 3-(4,5-dimethylthiazol-2yl)-2,5-diphenyl tetrazolium bromide (MTT), unstimulated (unstim.), fraction (f), tissue (t), lining cells (LCs), osteocytes (OYs)

growth curve of *Aga2* primary OBs was evaluated, and a limited saturation density was observed within the stimulated samples (Fig. 21B). The estimated 30 % reduction in OB

numbers between control and *Aga2* samples presumably comprised of cell loss due to apoptosis (see later) and reduced *in vitro* multi layering, potentially capable of triggering *in vivo* tissue renewal. Moreover, the observed deficiency in *Aga2* OB growth and viability was confirmed in extraskeletal primary dermal fibroblasts (Fig. S17). Similar to the OBs, stimulated *Aga2* fibroblasts depicted density limitation, suggesting a cell autonomous growth capacity defect in cells known to secrete large amounts of type I collagen. The cellular metabolic parameters were studied, whereby *Aga2* total protein and mitochondrial reductase activity levels were significantly increased by 32 % and 102 % respectively (Fig. 21C). There was a dramatic 60 % reduction in the total amount of secreted acid-soluble collagens tested in *Aga2* media. Of note, unstimulated *Aga2* OBs depicted no significant change in cellular protein and metabolic activity levels (data not shown).

To address the functional defects in *Aga2* OBs, nodular formation, growth and binding capacities were studied over time. The formation of *Aga2* bone-like nodules was persistently reduced 44 - 54 % between days 9 and 16, respectively (Fig. 21D, Density). The rate of nodule formation was significantly reduced in *Aga2* (0.39 ± 0.03 control and 0.19 ± 0.01 *Aga2*/+ nodules/mm^2/day; $p < 0.05$). The average area of individual *Aga2* nodules was reduced 89 - 64 % compared to controls (Fig. 21D, Area), and the rate of nodular growth was significantly inhibited (3.3 ± 0.5 control and 1.8 ± 0.2 *Aga2*/+ μm^2/day; $p < 0.05$). Lastly, a 3.2 fold comparative increase in nodular dye-binding capacity was observed in *Aga2* (Fig. 21D, Binding). These results clearly suggest defects in both OB metabolism and function.

3.1.1.12 Induction of matrix maturation without terminal differentiation

Osteocalcin (i.e. a specific marker for mature OBs) was evaluated to better define cellular differentiation in primary OB cultures. At 26 days in culture, *Aga2* calvarial OBs secreted 55 % elevated amounts of osteocalcin (Fig. 22A, graph). Late-stage osteocalcin immunoreactivity was localized to ossification centers and adjacent fronts of control nodules, depicting the matrix-dependent cessation of synthesis among the majority of cells (Fig. 22A, *ex vivo*). In contrast, *Aga2* cultures contained large subpopulations of mature OBs depicting intracellular osteocalcin within non-ossified matrix-spanning regions, and were also concentrated at the ossified foci of nodules. Histologically within normal cortex, osteocytes appeared morphologically distinct as dendritic, expressing limited amounts of osteocalcin (Fig. 22A, paraffin). On the other hand, *Aga2* cortical bones were hypercellular, and depicted increased distinct oblong cells. These cells were overly immunoreactive for osteocalcin at

Figure 22. Anomalies in *Aga2* osteoblast differentiation
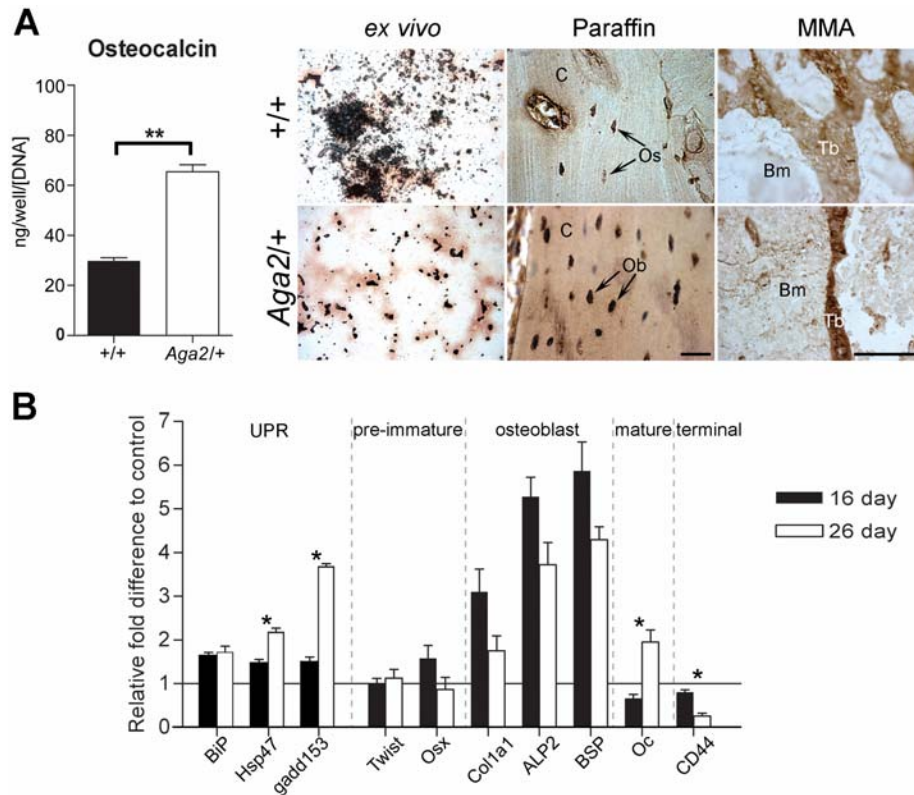
(Fig. 22) Analysis of the *Aga2* differentiation status. *A*, secreted osteocalcin levels were monitored in calvarial cultures at day 26 (graph), while osteocalcin immunoreactivity was visualized *ex vivo*, and in decalcified paraffin- and undecalcified MMA-embedded 12-week-old male femoral cortex and trabecula respectively. *Bars*, 20 μm for paraffin and 100 μm for MMA embedded samples. *B*, qPCR analysis of stimulated calvarial OBs. Values represent mean ± SEM, where n = 4 - 5 experiments (*$p < 0.01$ and **$p < 0.001$ Student t test). See Table S8 for genes. Os (osteocyte), Ob (osteoblast), Bm (bone marrow), C (cortex), Tb (trabecula), MMA (methyl methacrylate)

distances from active bone surfaces. Within undecalcified bone, *Aga2* trabeculae depicted elevated osteocalcin reactivity indicating a certain functional capacity toward the limited mineralized surface (Fig. 22A, MMA).

The temporal behavior of *Aga2* primary OBs was quantified by monitoring the expression of specific markers reflecting matrix maturation and mineralization via real time quantitative RT-PCR (qPCR; Fig. 22B). At day 16, no relative fold differences were observed in pre-immature OB lineage markers *Twist1* and *Osx* (osterix), indicating diploid cells during the post-proliferative phase. At day 16, large relative fold increases in OB markers *Col1a1*, *ALP2,* and *BSP* were observed in *Aga2*, signifying their temporal down regulation upon onset of mineral deposition within controls. At 16 days in culture, osteocalcin transcript levels were largely decreased in *Aga2*, depicting an earlier matrix synthesizing phase when compared to control. At day 26, the OB marker set was collectively decreased, yet still largely above the

Figure 23. Caspase-12-3-mediated apoptosis in *Aga2* primary osteoblasts and periosteum
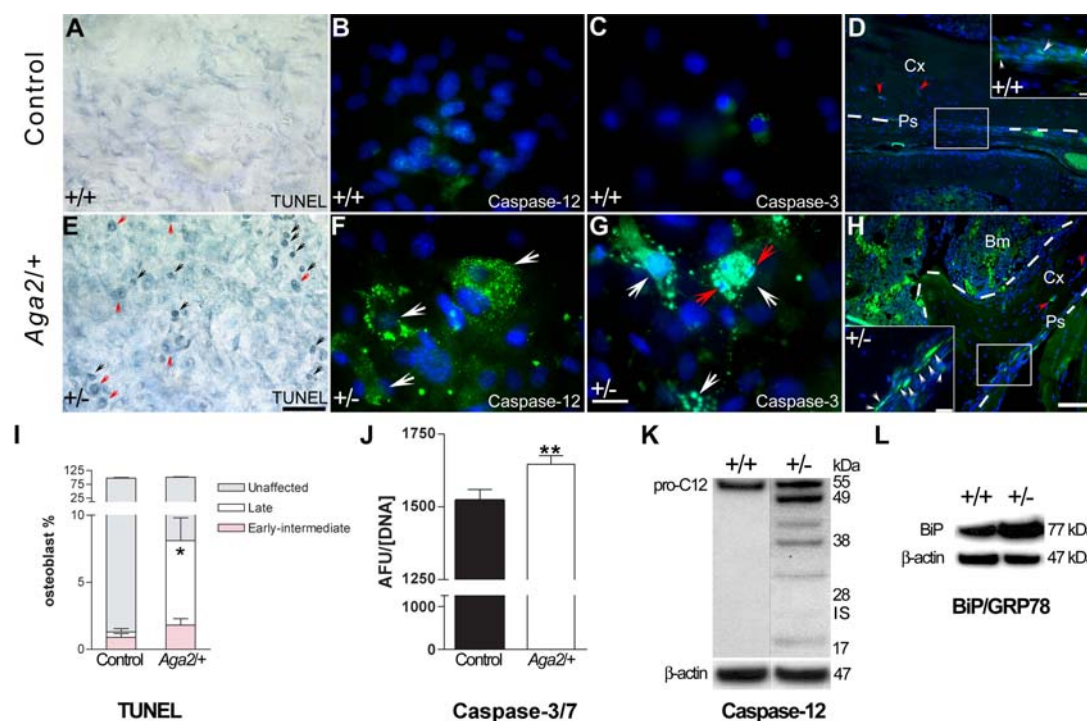
(Fig. 23) Initiation and execution of apoptosis in *Aga2*. *A* and *E*, TUNEL staining of 14-day-old stimulated calvarial OBs (early- and late-stages, red and black arrows respectively) were quantified in *I*. Caspases 12 and 3 immunofluorescence of 14-day-old OBs in *B* and *F*, and *C* and *G* respectively. Red arrows depict DNA fragmentation in *Aga2*. *D* and *H*, activated caspase-3 labeling of 12-week-old distal femur depicting dying cells (white arrows) within the periosteum (Ps) and cortical bone (Cx; red arrows). *J*, caspase-3/7 activity was measured via a fluorometric substrate assay. *K* and *L*, Western analysis of procaspase-12 and BiP using primary OBs respectively. Results are presented as mean ± SEM (*p = 0.0002 ANOVA and **p = 0.04 Student t test), where n = 4 independent experiments. *Bar*, 100 μm in *A*, *E*, and *D* and *H* main. *Bar*, 50 μm in *B*, *C*, *F*, and *G*. *Bar*, 20 μm in *D* and *H* insets. Nuclei were stained with DAPI. Arbitrary fluorescent unit (AFU), bone marrow (Bm), periosteum (Ps), low-present isoform (IS)

controls depicting dysregulation. The *Aga2* osteocalcin mRNA level was increased ~2-fold at day 26 reflecting heterogeneous subpopulations of both mature and active OBs, and the concomitant down regulation of upstream genes in control. *CD44* (hyaluronate receptor) is late-stage mineralization phase marker (17), whereby its relative level was unchanged in *Aga2* at day 16. At the terminal time point, *CD44* mRNA levels were reduced in *Aga2* indicating limited terminally differentiated OBs. Our results suggest a delay of the matrix-mineral phase transition in *Aga2* OB cultures.

3.1.1.13   Initiation of ER stress-induced apoptosis in *Aga2* OBs

To show involvement of key regulators of ER stress response pathways, qPCR studies were performed using primary calvarial OBs (Fig. 22B). At day 26 in culture, molecular chaperones BiP/GRP78 (binding protein/glucose-regulated protein 78) and Hsp47 (heat shock protein 47) transcripts were upregulated, i.e. less inducible in the former, ~1.7 – 2.2 folds above control, respectively. BiP protein levels were increased compared to controls as revealed during Western analysis (Fig. 23L). Gadd153 (growth arrest and DNA damage 153), a transcription factor involved in the induction of apoptosis, transcript was over expressed ~3.7 folds compared to control levels in *Aga2*/+ cells at the later time point.

Cell apoptosis was next studied within the context of ER-induced stress. The *Aga2* mutation led to a combined 7.5 ± 0.19 % relative increase in the number of early-late stage TUNEL-positive OBs compared to control (Fig. 23A,E,I). At 14 days in culture, *Aga2* preparations depicted a 10 % relative increase in the number of OBs which contained aberrant caspase-12-immunoreactivity (Fig. 23B,F; 3.3 ± 0.9 % control and 12.9 ± 1.9 % *Aga2*/+; $p = 0.0007$ Student t test). Additional caspase composites (i.e. negative controls) are available upon request. For specificity, proteolytic processing of procaspase-12 was evident only in *Aga2* samples via Western analysis (Fig. 23K). A 15 % relative increase in the number of activated caspase-3-positive OBs was observed in *Aga2* cultures (3.0 ± 0.9 % control and 17.5 ± 2.2 % *Aga2*/+; $p < 0.001$ Student t test). Caspase-3 activation was independently confirmed, and depicted a significant 9 % comparative increase in activity (Fig. 23J). Lastly, activated caspase-3 immunoreactivity was observed within femoral periosteum (Fig. 23D,H). *Aga2* tissue contained elevated relative numbers of activated caspase-3-positive OBs (28.9 ± 2.7 % control and 42.6 ± 4.1 % *Aga2*; $p = 0.02$ Student t test), suggesting a 14 % comparative basal increase in apoptosis. TUNEL experiments also revealed increased numbers of DNA-fragmented OBs within *Aga2* periosteum (Fig. S18). In *Aga2*, ER-associated apoptosis was

Figure 24. Proposed ER stress response pathway in *Aga2* osteoblasts
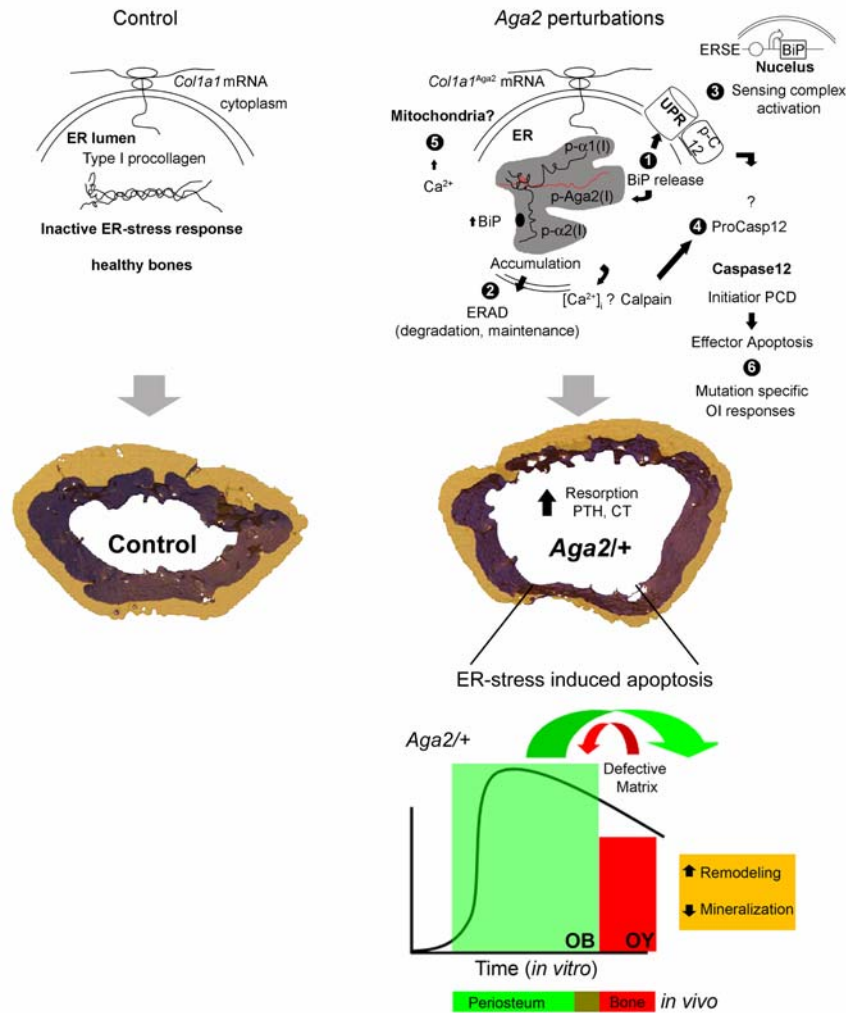
(Fig. 24) Scheme depicting the UPR initiation of the caspase cascade in *Aga2. Aga2* perturbations were initiated via accumulation of mis/unfolded type I procollagen molecules within the ER. Sequestration and release of BiP chaperone (circle 1) from divergent molecular transducers localized in the ER membrane regulate stress responses and provide the conditioning for apoptosis. BiP attachment to mis/unfolded proteins is potentially involved in the retrotranslocation machinery towards proteasomal degradation (circle 2). Activation of the sensing complex leads to a series of reactions which include the transcription of ERSE genes (e.g. BiP; circle 3). If the stress sensor complex cannot manage the overall ER load, a caspase-12 pro-apoptotic pathway is triggered via several potential mechanisms (circle 4). Convergence of other apoptotic signals may derive from the mitochondria (circle 5). Eventually, an effecter response is reached leading to detrimental consequences on skeletal tissue integrity (circle 6). The matrix defect leads to increased bone resorption and a decrease in procollagen extrusion in *Aga2*. ER associated degradation (ERAD), ER stress element (ERSE), p-C12 (procaspase 12), parathyroid hormone (PTH), calcitonin (CT)

inherent within OBs, evident at the periosteum, and mediated via caspases 12 and 3 toward eventual death (Fig. 24).

3.1.2 *Aga2* systemic phenotypes

3.1.2.1 Clinical chemical analysis

In collaboration with the Clinical Chemistry unit of the GMC, basic clinical chemical and hematological parameters in 12-week-old animals were investigated in order to detect anomalies in various organ systems apart from the skeleton by way of alterations in metabolic pathways and electrolyte homeostasis (Table 5). A pathological ~30 – 28 % decrease in mean α-amylase activity was found in both sexes of *Aga2*/+ animals when compared to control in plasma. Furthermore, triglyceride and cholesterol concentrations were decreased to pathological levels, the latter more severely affected in *Aga2* males. Additionally, small significant increase in creatinine levels, as well as large increases in creatinine kinase, aspartate-aminotransferase and alanine-aminotransferase activities were detected (data not shown) only in *Aga2* males compared to controls. *Aga2* males also yielded a comparative ~6 % reduction in total protein amounts. In particular, *Aga2* females showed a slight significant increase in chloride concentrations, and a weakly significant decrease (~8 %) in mean lipase activity (data not shown). *Aga2* animals showed a decrease in amylase activity. Sodium, potassium, urea, glucose, ferritin and transferrin levels were unchanged in *Aga2* animals (data not shown). Overall, the *Aga2* male population was induced to more drastic changes in clinical chemical parameters.

Concerning the hematological analysis, increased white blood cells in both sexes of *Aga2* mice was detected compared to control. No changes in the red blood cell, platelet and hematocrit counts/measurements were observed in *Aga2* mice (data not shown). Moreover, hypochromic anemia was uncovered in both sexes of *Aga2* mice depicting a ~5 - 4 % reduction in whole blood hemoglobin concentration, and a ~4 - 2.5 % decrease in erythrocyte hemoglobin content. Lastly, a ~7.5 – 3 % increase in erythrocyte size variability within *Aga2* male and female mice was observed. Sex differences were detected in both control and *Aga2* animals which may reflect physiological differences typically seen in C3HeB/FeJ mice. All in all, these results suggest systemic tissue injury and metabolic considerations within *Aga2* mice.

Table 5. Clinical chemical analysis at 12 weeks of age

Parameter	Control (A)		Aga2/+ (B)		Pairwise		ANOVA		
	Male	Female	Male	Female	A-B Male	A-B Female	Genotype	Sex	Interaction
Plasma	(*n* = 15)		(*n* = 15)						
Total Protein [g/dl]	5.78 ± 0.08	5.4 ± 0.06	5.4 ± 0.04	5.3 ± 0.08	***↓	NS	**	***	NS
Creatinine [mg/dl]	0.34 ± 0.004	0.37 ± 0.005	0.36 ± 0.006	0.38 ± 0.005	*↑	NS	**	***	NS
Cholesterol [mg/dl]	176.8 ± 4.05	123.9 ± 3.01	143.1 ± 1.93	112.8 ± 1.54	***↓	*↓	***	***	***
Triglyceride [mg/dl]	328.9 ± 21.90	288.0 ± 19.20	151.1 ± 15.20	131.3 ± 8.10	***↓	***↓	***	NS	NS
α-amylase [U/l]	2365 ± 38.4	2007 ± 35.8	1691 ± 41.0	1557 ± 23.8	***↓	***↓	***	***	**
Blood									
WBC [10^3/µl]	6.3 ± 0.33	6.2 ± 0.29	8.4 ± 0.64	7.1 ± 0.32	**↑	*↑	***	NS	NS
Hemoglobin [g/dl]	15.0 ± 0.16	15.3 ± 0.12	14.3 ± 0.15	14.8 ± 0.12	***↓	**↓	***	**	NS
MCHC [g/dl]	33.0 ± 0.21	33.8 ± 0.14	31.7 ± 0.22	32.9 ± 0.20	***↓	**↓	***	***	NS
Red cell dist. Width [% of MCV]	13.3 ± 0.07	13.1 ± 0.06	14.3 ± 0.13	13.5 ± 0.11	***↑	*↑	***	***	**

(Table 5) Data presented as mean ± SEM. *$p < 0.05$, **$p < 0.01$, ***$p < 0.001$
White blood cell (WBC), mean corpuscular hemoglobin concentration (MCHC), mean corpuscular volume (MCV)

3.1.2.2 Primary cardiology screen

At 14 weeks of age, *Aga2* animals were investigated in collaboration with the Cardiovascular Unit of the GMC to identify anomalies of the vascular system via measurements of non-invasive blood pressure and electrocardiogram (ECG). Blood pressure analysis did not reveal any significant differences between the tested groups (data not shown). ECG analysis detected genotype-specific increases in the heart rate of *Aga2* mice compared to controls (Table 6; see Fig. S18 for sample ECG trace). Accordingly, the RR interval was also reduced in *Aga2*. The P-wave duration was only found to be slightly increased in *Aga2* females compared to controls. In both *Aga2* sexes, the JT interval and the QRS amplitude were comparatively enhanced. These observations were mainly caused by amplitude differences of the Q and S waves. Overall, the ECG alterations suggest morphological and/or conductive defects of *Aga2* heart.

Table 6. Cardiovascular screen at 14 weeks of age

Parameter	Control (A)		Aga2/+ (B)		Pairwise		ANOVA		
	Male (n = 10)	Female (n = 9)	Male (n = 10)	Female (n = 10)	A-B Male	A-B Female	Genotype	Sex	Interaction
ECG									
P-wave duration [ms]	19.4 ± 0.6	17.6 ± 0.6	18.3 ± 0.8	20.1 ± 0.8	NS	*↑	NS	NS	*
RR interval [ms]	128.8 ± 4.9	114.2 ± 3.4	105.1 ± 1.8	104.8 ± 1.5	***↓	*↓	***	*	*
Heart rate [bpm]	471.9 ± 17.0	529.4 ± 15.0	572.4 ± 9.6	573.9 ± 7.9	***↑	*↑	***	*	*
JT interval [ms]	3.6 ± 0.3	3.6 ± 0.1	4.4 ± 0.1	4.6 ± 0.3	*↑	**↑	***	NS	NS
Q amplitude [mV]	0.01 ± 0.00	0.02 ± 0.01	0.05 ± 0.01	0.05 ± 0.00	***↑	**↑	***	NS	NS
S amplitude [mV]	-0.28 ± 0.1	-0.83 ± 0.2	-1.37 ± 0.2	-1.30 ± 0.2	***↑	*↑	***	NS	NS
QRS amplitude [mV]	2.48 ± 0.1	2.88 ± 0.2	3.24 ± 0.1	3.34 ± 0.2	**↑	*↑	***	NS	NS

(Table 6) Data presented as mean ± SEM. $*p < 0.05$, $**p < 0.01$, $***p < 0.001$

3.1.2.3 Primary lung function screen

In collaboration with the Lung Function Unit of the GMC, spontaneous breathing patterns during rest and activity were analyzed in 15-week-old *Aga2* mice for potential alterations in mechanisms that control respiration. *Aga2*/+ males had more affected parameters compared to mutant females relative to controls during both rest and active spirometry measurements (Table 7). The weight differences in *Aga2* mutant mice led to obvious breathing pattern differences at rest, i.e. large specific TV and MV increases compared to controls (sTV: ~65 % male and ~54 % female; sMV: ~38 % male and ~55 female). ANCOVA was performed with weight as a covariate for both TV and MV. No significant differences were observed in both TV and MV, speculating that the specific differences observed were due to weight effects. Nevertheless, the mean expiratory time (Te) was ~18 % longer in *Aga2* males compared to controls with a concomitant ~13 % lowered mean respiratory rate. The rest to activity transition was nearly the same for all measured parameters. One major difference for males was a ~13 % reduction in the mean expiratory flow rate (MEF), which was enhanced during activity as a result of the longer Te. For females during activity, there was a weakly significant ~7 % decrease in inspiratory time (Ti), which was partly due to an increased, yet insignificant, tendency toward an elevated respiratory rate. Overall, these results suggest possible tissue defects affecting respiration in *Aga2*.

Table 7. Lung function screen at 15 weeks of age

Parameter	Control (A)		Aga2/+ (B)		Pairwise		ANOVA		
	Male (n = 7)	Female (n = 7)	Male (n = 7)	Female (n = 7)	A-B Male	A-B Female	Genotype	Sex	Interaction
Rest									
BW [g]	35.0 ± 1.4	29.0 ± 1.9	21.8 ± 0.8	18.0 ± 0.4	***↓	***↓	***	NS	NS
F [1/min]	333.1 ± 7.2	334.7 ± 5.4	290.1 ± 10.6	345.0 ± 15.7	**↓	NS	NS	*	*
[1]TV [ml]	0.20 ± 0.01	0.19 ± 0.01	0.20 ± 0.01	0.18 ± 0.01	NS	NS	NS	NS	NS
sTV [µl/g]	5.7 ± 0.1	6.7 ± 0.3	9.4 ± 0.5	10.3 ± 0.4	***↑	***↑	***	*	NS
[2]MV [ml/min]	63.9 ± 2.3	62.6 ± 3.5	55.3 ± 1.4	60.8 ± 4.0	NS	NS	NS	NS	NS
sMV [ml/min/g]	1.8 ± 0.1	2.2 ± 0.1	2.5 ± 0.1	3.4 ± 0.2	***↑	**↑	***	***	NS
Te [ms]	127.1 ± 3.7	126.2 ± 2.4	149.6 ± 5.9	123.6 ± 6.9	**↑	NS	NS	*	*
Activity									
F [1/min]	463.7 ± 5.3	468.0 ± 7.9	428.5 ± 10.5	480.6 ± 10.4	*↓	NS	NS	**	*
[1]TV [ml]	0.21 ± 0.01	0.21 ± 0.01	0.20 ± 0.01	0.18 ± 0.01	NS	NS	*	NS	NS
sTV [µl/g]	6.0 ± 0.2	7.2 ± 0.4	9.3 ± 0.4	10.2 ± 0.6	***↑	**↑	***	*	NS
[2]MV [ml/min]	95.6 ± 3.6	95.8 ± 3.4	85.2 ± 1.4	87.2 ± 3.9	NS	NS	**	NS	NS
sMV [ml/min/g]	2.7 ± 0.1	3.3 ± 0.1	3.9 ± 0.1	4.9 ± 0.3	***↑	***↑	***	***	NS
Ti [ms]	41.9 ± 0.7	41.2 ± 0.5	43.6 ± 0.9	38.4 ± 0.4	NS	**↓	NS	***	**
Te [ms]	87.6 ± 0.9	87.1 ± 1.9	96.8 ± 2.6	86.6 ± 2.7	**↑	NS	NS	*	*
MEF [ml/s]	2.4 ± 0.1	2.4 ± 0.1	2.1 ± 0.1	2.1 ± 0.1	**↓	NS	**	NS	NS

[1] ANCOVA with body mass as a covariate was also performed for genotype, sex and interacting factors: Rest - Genotype $p = 0.46$; Sex $p = 0.97$; and interaction $p = 0.26$; Activity - Genotype $p = 0.43$; Sex $p = 0.45$; and interaction $p = 0.52$.

[2] ANCOVA with body mass as a covariate was also performed for genotype, sex and interacting factors: Rest - Genotype $p = 0.40$; Sex $p = 0.77$; and interaction $p = 0.37$; Activity - Genotype $p = 0.20$; Sex $p = 0.40$; and interaction $p = 0.18$.

Data presented as mean ± SEM and arrows relative to control. $*p < 0.05$, $**p < 0.01$, $***p < 0.001$

Body weight (BW), F (respiratory rate), s (specific), TV (tidal volume), minute ventilation (MV), inspiratory time (Ti), expiratory time (Te), mean expiratory flow rate (MEF)

Table 8. Metabolic screen at 18 - 20 weeks of age

Parameter	Control (A)		Aga2/+ (B)		Pairwise		ANOVA		
	Male (n = 7)	Female (n = 7)	Male (n = 7)	Female (n = 7)	A-B Male	A-B Female	Genotype	Sex	Interaction
BW [g] *ad libitum*	32.8 ± 0.58	33.9 ± 1.02	21.9 ± 0.61	20.8 ± 0.45	***↓	***↓	***	NS	NS
Rectal temp. [°C]	35.9 ± 0.06	36.4 ± 0.04	35.4 ± 0.25	36.0 ± 0.04	*↓	NS	**	**	NS
Food consumption [g day^{-1}]	4.3 ± 0.12	4.49 ± 0.10	3.01 ± 0.25	4.42 ± 0.29	***↓	**↓	***	***	NS
[1]Energy uptake [kJ day^{-1}]	76.9 ± 2.19	84.8 ± 3.69	53.7 ± 4.47	78.8 ± 5.24	***↓	**↓	***	***	NS
Energy uptake BW^{-1} [kJ g^{-1} day^{-1}]	2.35 ± 0.08	2.62 ± 0.13	2.44 ± 0.18	3.8 ± 0.27	NS	***↑	**	***	**
Feces production [g day^{-1}]	1.05 ± 0.02	1.12 ± 0.04	0.8 ± 0.05	0.9 ± 0.03	***↓	***↓	***	*	NS
Energy content feces [kJ g^{-1}]	15.5 ± 0.06	15.5 ± 0.05	15.4 ± 0.08	15.3 ± 0.03	NS	*↓	*	NS	NS
[2]Metabolized energy [kJ day^{-1}]	59.4 ± 1.87	69.3 ± 1.47	40.6 ± 3.85	63.7 ± 4.84	***↓	*↓	***	***	NS
Metabolized energy BW^{-1} [kJ g^{-1} day^{-1}]	1.81 ± 0.06	2.06 ± 0.11	1.84 ± 0.16	3.07 ± 0.25	NS	***↑	**	***	**
Food assimilation coefficient [%]	77.2 ± 0.32	78.6 ± 0.42	74.9 ± 1.66	80.5 ± 0.73	NS	NS	NS	***	NS

[1] ANCOVA with body mass as a covariate was also performed for genotype, sex and interacting factors: Genotype $p = 0.007$; Sex $p = 0.54$; and interaction $p = 0.13$.
[2] ANCOVA with body mass as a covariate was also performed for genotype, sex and interacting factors: Genotype $p = 0.01$; Sex $p = 0.61$; and interaction $p = 0.72$.
Data presented as mean ± SEM. *$p < 0.05$, **$p < 0.01$, ***$p < 0.001$
Body weight (BW)

3.1.2.4 Primary energy metabolism

Basal energetic demands were monitored in *Aga2* during *ad libitum* feeding starting at 18 weeks of age in collaboration with Energy Metabolic Unit of the GMC (Table 8). Among *Aga2* mice, food and energy uptake were comparatively less reduced in females (~2 % and ~7 % respectively) versus males (~21 % both). The specific energy uptake and ratio of metabolized energy were significantly elevated compared to controls only among the *Aga2/+* females (~45 % and ~49 % respectively). The differences observed in energy uptake and energy metabolized could be solely related to body mass, not genotype. Subsequently, strong genotype differences were observed for energy uptake ($p = 0.007$) and metabolized energy (p

Figure 25. Molecular phenotyping of lung tissue
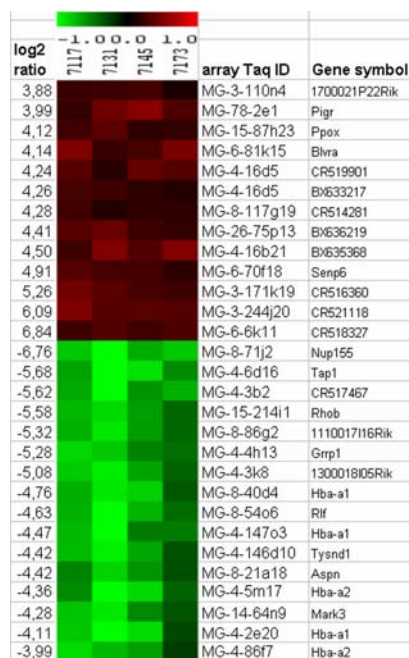
(Fig. 25) Heat map of gene expression profiles from eight DNA microarray experiments of *Aga2* versus control mice. Two dye-flip pairs represent two experimental replicates of each analyzed individual (n = 4). The ArrayTAG ID is the unique probe identifier from the Lion Bioscience clone set. The scale bar encodes the log ratio of the fold induction. 0.1 % of the elements was above the upper limit of the color range selection (green is down-regulation and red is up-regulated in *Aga2* samples). Pigr (polymeric Ig receptor), Ppox (protoporphyrinogen oxidase), Blvra (biliverdin reductase A), Senp6 (SUMO/sentrin specific peptidase 6), Nup155 (nucleoporin 155), Tap1 (transporter 1, ATP-binding cassette, sub-family B), RhoB (ras homolog gene family, member B), Grrp1 (glycine/arginine rich protein 1), Hba-a1/2 (hemoglobin alpha, adult chain 1/2), Rlf (rearranged L-myc fusion sequence), Tysnd1 (trypsin domain containing 1), Aspn (asporin), Mark3 (MAP/microtubule affinity-regulating kinase 3)

= 0.01) using ANCOVA with weight as a covariate. Lastly, the degree of food assibilation was unchanged between *Aga2* mice and controls signifying no physiological defects in the ability to metabolize the available energy. Overall, *Aga2* animals appear to rely on different metabolic strategies, whereby the females exhibited the highest energetic demand.

3.1.2.5 Expression profile

Last, lung tissue from 15-week-old animals were used to generate gene expression profiles from DNA microarray experiments. Statistical analysis detected four upregulated and ten down regulated genes (Fig. 25). The dysregulated genes represent many genes known to be essential for regulation of cellular and tissue function. Upregulated genes clustered into heme biosynthetic (e.g. Ppox) and catabolic (e.g. Blvra), mucosal-dependent immune protection

(e.g. Pigr), and the ubiquitin-like cycle/proteolysis (e.g. Senp6) functional categories. The down regulated genes were functionally characterized as affecting nucleocytoplasmic transport (e.g. Nup155), immune defense (e.g. Tap-1), apoptosis (e.g. RhoB), zinc binding (e.g. Rlf), oxygen transport (e.g. Hba-a1/2), porin (e.g. Aspn), phosyphorylation (e.g. Mark3), and unknown (e.g. Grrp1) pathways. Both Hba-a1 and 2 were down regulated ~4.76 – 3.99 folds respectively compared to controls. Nup155, Tap1, RhoB, and Grrp1 were down regulated $> 5 \leq 6.76$ folds in *Aga2* samples. And Senp6 was the highest overexpressed gene (4.91 folds) in *Aga2* samples compared to controls. These results suggest significant transcriptional changes in either the blood (i.e. derived from alveoli capillaries), lung parenchyma and stroma, and hyaline cartilage and smooth muscle of the bronchi within *Aga2* lung tissue.

3.2   *Ali34* (abnormal limb 34)

3.2.1   Dysmorphological changes

In *Ali34*/+ animals, secondary bone formation and gross chondrocytic abnormalities were apparent (Fig. 26). *Ali34* mice feature altered hind limb morphology with the disorganization of skeletal elements, while the skeletal remainder was kept largely intact suggesting that movable joints in the upper limbs, spine and pelvis were unaffected. The sesamoid patella of *Ali34* was partially encased in the inferior trochlear groove (see later). Irregular sclerotic changes at the knee were obvious. Ectopic bone struts were located on both lateral and media epicondyles, and superfluous cartilage formation was evident at the posterior condyles. The hyaline cartilage of the tibial plateau was obscured by ectopic bone formation. In *Ali34* animals, the epiphysial line of the tibial inferior aspect of the articular capsule did not assume the curved path and perpendicularly to the articular surface at every point as seen in control. Epiphysial stippling was apparent, as well as abnormal medial invagination. Portions of the subchondral growth plate were devoid of cartilage, suggesting degradation. Consequentially, both *Ali34* femur and tibia were blunted and thickened. These dysmorphological features occurred at a lowered penetrance and stochastically between either or both hind limbs in heterozygous animals. No evidence of brachydactyly was ever witnessed in the *Ali34* line.

Figure 26. *Ali34*/+ dysmorphology
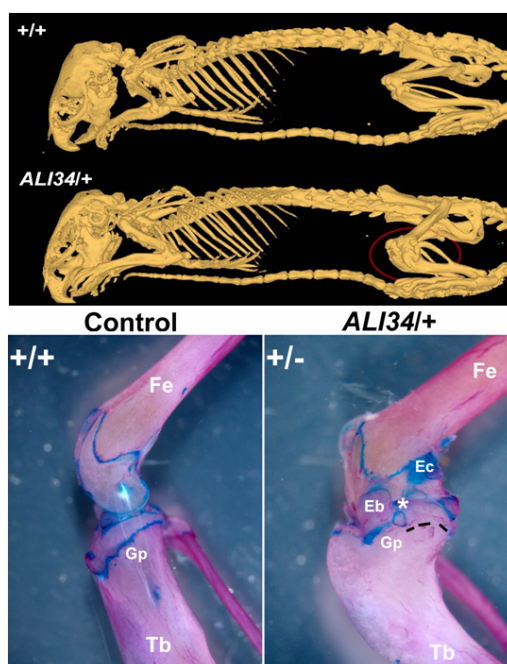
(Fig. 26) µCT and skeletal preparations. 29-week-old *Ali34*/+ mice feature severe anklylosis (red circle). Both *Ali34* femur (Fe) and tibia (Tb) were achondroplastic and sclerotic. Growth plate (Gp), ectopic bone struts (Eb), ectopic cartilage (Ec), medial invagination (*), missing cartilage of subchondral growth plate (black dash)

Homozygosity of the *Ali34* locus was studied within heterozygous double matings (Fig. 27). *Ali34*/*Ali34* embryos lacked the neurocranium (i.e. the calvaria and base of skull) and developed deviated vertebral columns. The viscerocranium (i.e. the mandible, zygoma, and maxilla) and craniofacial plates in *Ali34*/*Ali34* embryos appeared intact. These results suggest that the *Ali34* locus plays a key role during calvarial intramembranous ossification and spinal column formation during development. The *Ali34* locus could either play a role during preosteoblast condensation and somitogenesis, or during the differentiation and maintenance phase which occurs thereafter.

3.2.2   Histological and semi-histomorphometric analysis

The *Ali34* manifestations during early adult stages consisted of subchondral bone struts and bone formation within joints (Fig. 28). Sclerotic bone struts symbolize anomalies during chondrogenesis, and normal subchondral calcification and degradation leading to inhibition of horizontal limb growth. The mottled epiphysial appearance was most likely caused by alternating zones of faulty chondrogenesis and osteogenesis. Furthermore in the histological

Figure 27. Embryonic lethality and calvarial agenesis
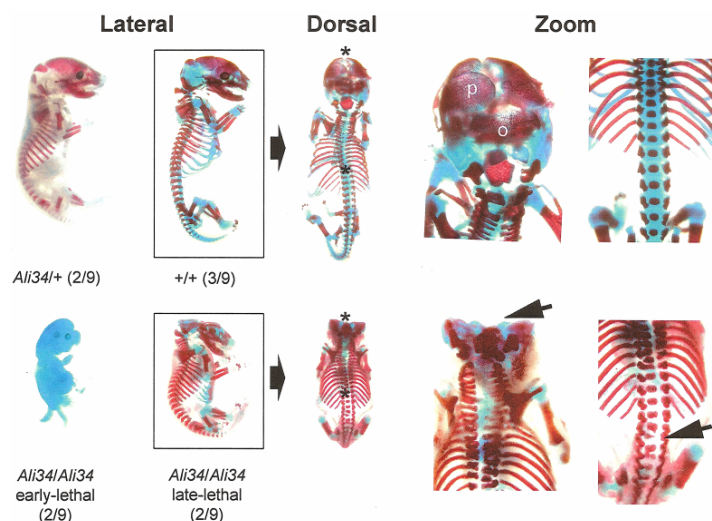
(Fig. 27) Skeletal preparations. Embryos (E18) from *Ali34*/+ X *Ali34*/+ matings were placed into four categories (lateral view): 1. suspect heterozygotes (i.e. depicting anomalies in musculature), 2. wild types (boxed), 3. severely-affected homozygotes, and 4. homozygotes with calvaria agenesis (boxed). *Ali34*/*Ali34* embryos lacked the caudal portion of the skull and developed un-fused vertebral columns (arrow heads). * (zoomed regions), P (parietal plate), O (occipital plate)

sections, excessive neotendon formation was seen in *Ali34* as a fibrous layer encapsulating the patella. The posterior patella merged into the synovial capsule. The fibrous capsule extended into the articular space adjacent the tibia, not surrounding as in control (see Fig. S19 for knee joint scheme). Soft bone elements were continuous with the *Ali34* fibrous layer. Chondrification (see later) and mineralized ectopic bone-like formation were present within the articular space leading to further joint stiffness. A qualitative histomorphometric analysis of bone formation depicted a reduction in new net bone formation within both the primary spongiosa and metaphysial trabeculae in *Ali34* femora (Fig. 29). Areas of ectopic growth contained new bone-like formation, although disorganized yielding only a detectable single label. In agreement with reduced endochondral bone formation, pQCT analysis of the femur metaphysis revealed significant reduction in trabecular vBMD within *Ali34*/+ male animals (295.4 ± 15.4 mg/cm^3 control [$n = 10$] and 258.3 ± 30.5 mg/cm^3 *Ali34*/+ [$n = 8$]; $p = 0.001$), presumably due to reduced trabecular numbers. Cortical density at the femur diaphysis was unchanged (data not shown).

Figure 28. Diarthrosis (knee joint) ossification
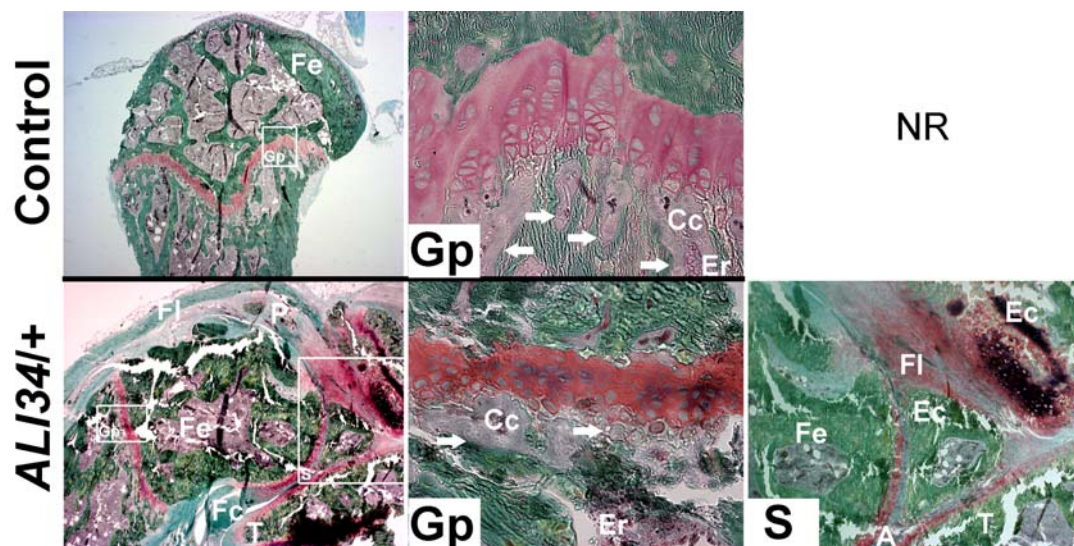
(Fig. 28) Undecalcified sagittal femoral sections of 12-week-old mice. Normal epiphysial plate harbors degraded cartilage formed as spicules undergoing provisional calcification (arrows; Cc). In *Ali34*, the subchondral surface was sclerotic (arrows; Cc). The posterior patella (P) and fibrous capsule (Fc) merged into the synovial capsule (S box) to form mineralized components (Ec green). Villanueva osteochrome stain applied during histology. Light green (fibrous elements), dark green (bone), light red (cartilage, soft bone or osteoid seam), tibia (T), erosion (Er), neotendon (Fl), articular space (A), not relevant (NR)

Figure 29. Reduced endochondral bone formation
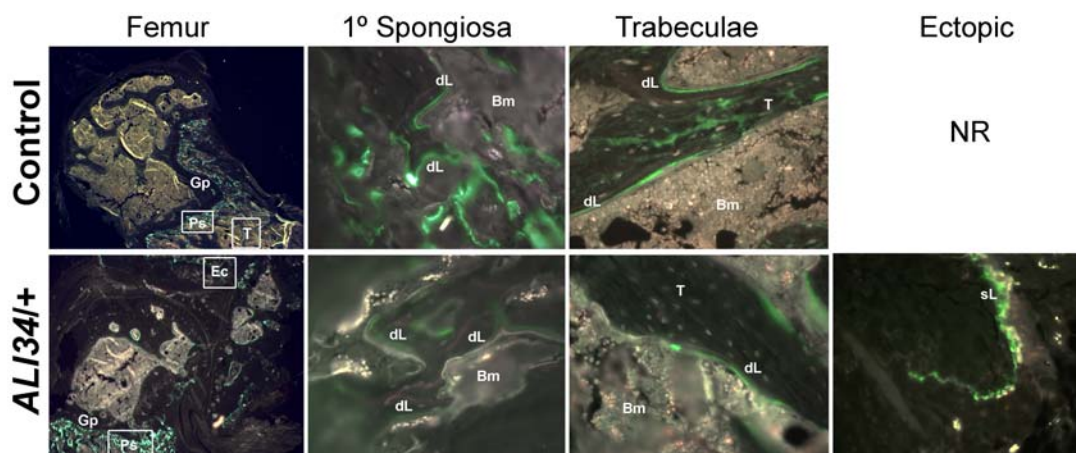
(Fig. 29) Rates of mineralization and bone formation were observed in tetracycline (red)-calcein (green) double labeling (dL) studies among 12-week-old male mice. Qualitatively (i.e. as judged by both red and green areas over time), endochondral bone-like formation at the osteogenic zone was reduced in *Ali34*. Ectopic regions (Ec) harbored new bone formation, although disorganized as a single label (sL). Bm (bone marrow), Ps (primary spongiosa), T (trabeculae), Gp (growth plate)

3.2.3   Growth plate and articular defects

The interstitial growth plate and articular cartilage defects were further studied in *Ali34*. Disorganized clusters of non-isogenic chondrocytes, and chondromalacia of articular and epiphysial cartilages were present in *Ali34* (Figures 30-32). Proteoglycan expression (i.e. as monitored via Safranin O staining) was restricted to only the anterior edge of both femoral and tibial articular cartilages, suggesting severe chondrolysis and degradation (asterix, Fig. 30). Furthermore, regions of the growth plate were devoid of proteoglycan expression. There was also an absence of isogenous groups, and the resting and proliferative zones. Such isogenous groups reflect the last mitotic division of a chondrocyte whose daughter cells have not secreted more territorial matrix. In the *Ali34* growth plate, there appeared to be an excess of larger cells, but it is unclear whether this population is indeed pre/hypertrophic chondrocytes, or immature chondrocytes with altered growth features. In order to assess vascularitiy in the growth plate, immunohistochemical analysis against chondromodulin I (ChM-I) was performed. ChM-I is an autocrine tissue-specific angiogenesis inhibitor localized to the avascular zone 3 of the growth plate, and hypovascular connective tissues (147). In the *Ali34* growth plate, ChM-I was expressed territorially as in the control, but disorganized in an unrestricted fashion encompassing the entire tissue. Moreover, ChM-I ectopic synthesis was present at the capsule region of lacunas, not in territorial regions as in normal growth plate chondrocytes. This could reflect local altercations in the hypertrophic ectopic ECM milieu as incompatible in retaining ChM-I, or homing of the glycoprotein towards the proteoglycan rich regions of clustered blastema/chondroblasts for proper growth stimulation. Lastly in *Ali34* osteophytes, a clear sequential process of chondrification was present which presumably derived from a mesenchyme blastema originating from the disorganized connective joint layers. It is also possible that mesenchyme tissue surrounding the blastema gave rise to ectopic perichondrium. These results show that the *Ali34* mutation involved the entire synovial joint, including both cartilage and synovium.

Articular cartilage is depicted as zones, whereby each zone secretes distinct matrix (Fig. 31). Zone 1 is a connective non-cellular layer. Zone 2 is a transitional zone which harbors 'resting' chondroblasts and ground substance. In *Ali34*, zone 2 was missing. The radial zone 3 contained maturing and hypertrophic chondrocytes. In *Ali34*, zone 3 constitutes a larger relative portion of articular cartilage compared to control. Zone 4 is a calcified cartilage layer with a tidal mark above subchondral bone. This is a zone which contains partly

Figure 30. Interstitial growth plate defects
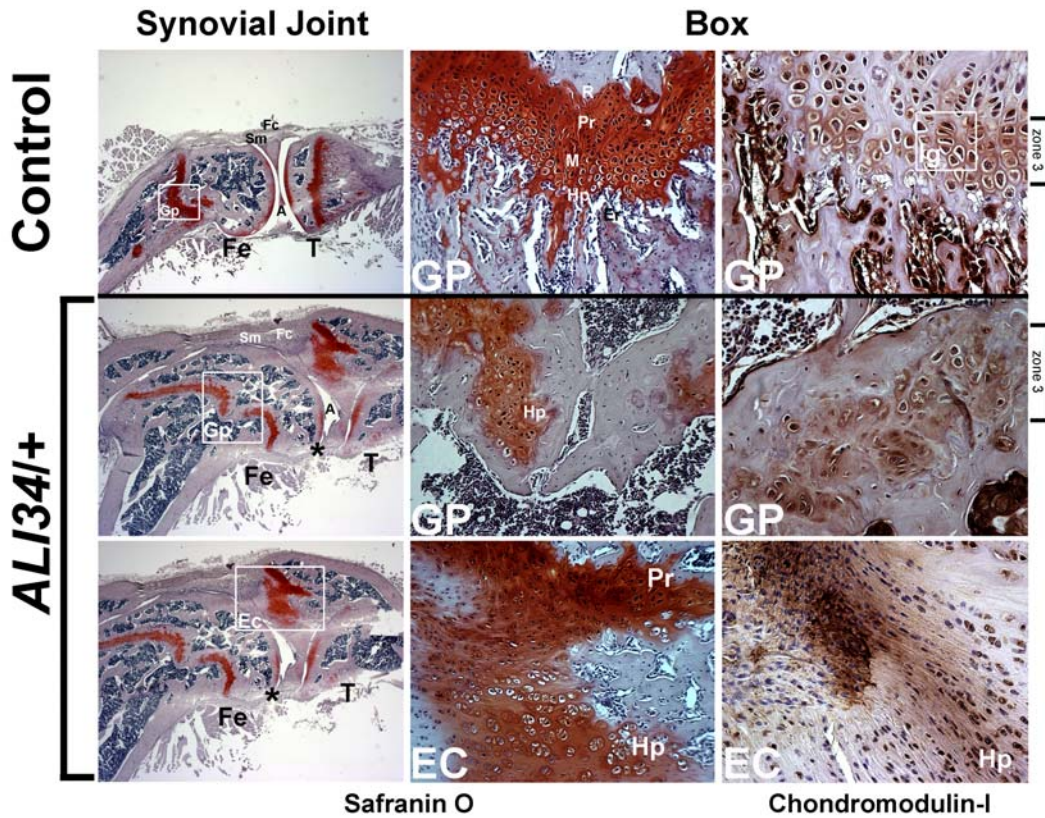
(Fig. 30) Growth plate defects in 12-week-old *Ali34* animals. Fe (femoral), T (tibial), * (articular cartilage), Ig (isogenous groups), R (resting zone), Pr (proliferating zone), Ec (ectopic or osteophytes), A (joint space), M (mature), Hp (hypertrophic), Er (erosion), Sm (synovial membrane), Fc (fibrous capsule), Gp (growth plate)

Figure 31. Articular defects
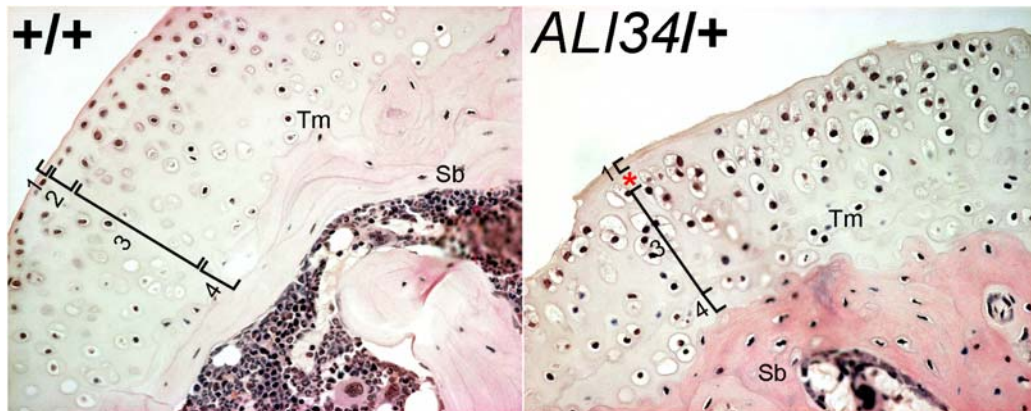
(Fig. 31) Disorganized and enlarged chondrocytes in *Ali34* articular cartilage. Stained with H&E using 12-week-old tissue. * (missing zone 2), Tm (tidal mark), Sb (subchondral bone)

Figure 32. Articular matrix defect
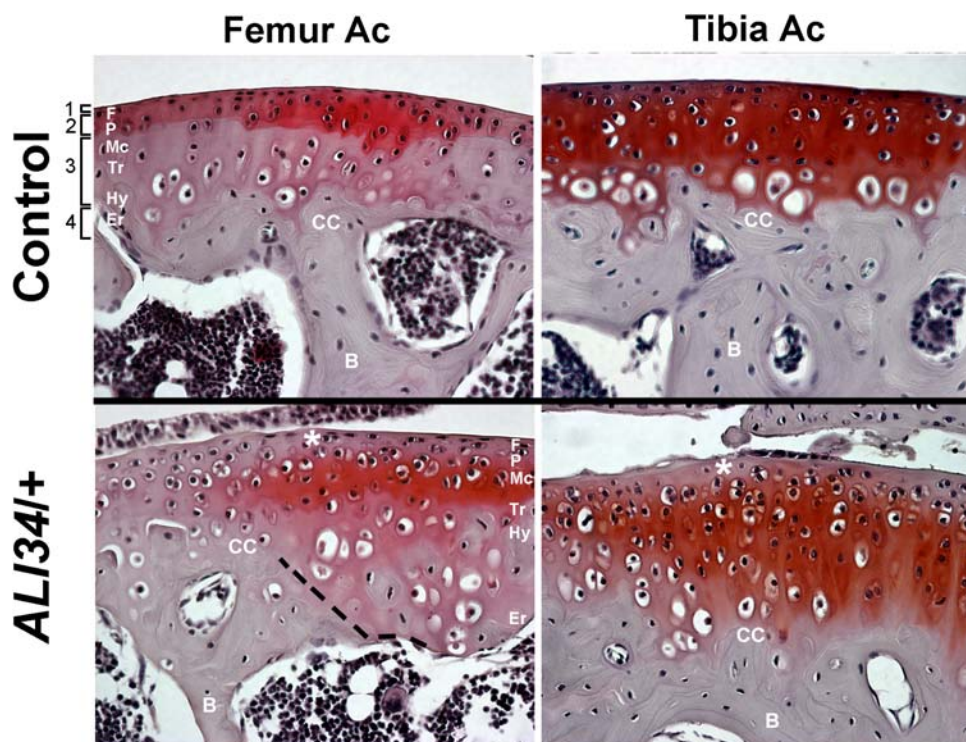
(Fig. 32) Precocious destruction and erosion of both *Ali34* tibial and femoral articular cartilage (Ac) matrix in 12-week-old mice. Stained with Safranin O. * (zone 2), B (bone), Cc (calcified cartilage; dotted line), F (fibrous zone), P (chondroblast), Mc (mature chondrocyte), Tr (transitional), Hy (hypertrophic), Er (erosion)

dieing hypertrophic chondrocytes, neovascularation, and considered a region where osteogenesis begins. In *Ali34*, zone 4 was reduced. These results suggest that the chondrocyte transition (i.e. differentiation) was compromised in *Ali34*. Proteoglycan degradation was marked in *Ali34*/+ and regionalized to the superficial layer (zone 2; Fig. 32). Furthermore in certain locations, the enlarged chondrocytes in *Ali34* extended to the bone surface without a calcified cartilage zone. Additionally, the growth plate and articular cartilage of the intervertebral discs and fore limbs were histologically investigated, and all appeared to be unaffected in *Ali34* animals (data not shown). Of note, cartilage fissures were not observed, which can cause over proliferation of cartilage cells during repair.

Figure 33. Fibrous alteration and tendon metaplasia
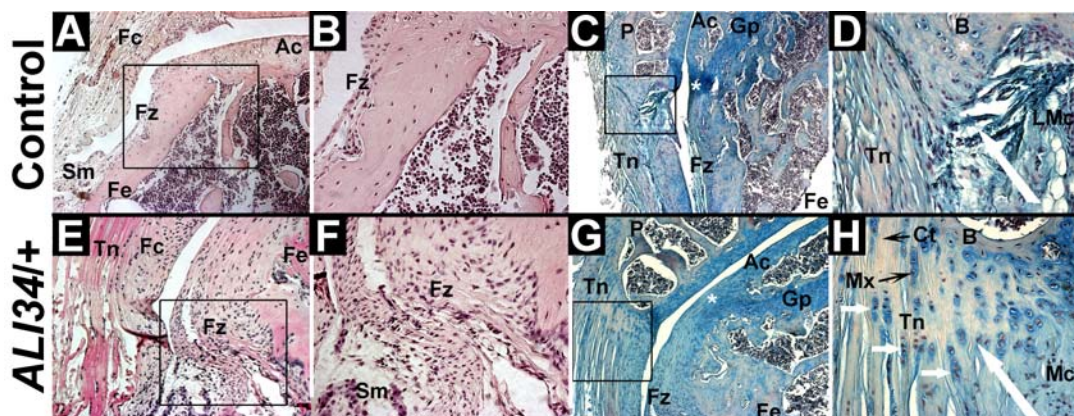
(Fig. 33) The posterior femoral (Fe) articular capsule is shown in Panels *A-B* (control) and *E-F* (*Ali34*/+) using H&E stain in 12-week-old tissue. Tendon structure was studied using alcian blue in Panels *C-D* (control) and *G-H* (*Ali34*/+). Fz (fibrous zone), Fe (femur), Ac (articular cartilage), Fc (fibrous capsule), Gp (growth plate), B (bone), LMc (loose mesenchyme), Mx (cartilage matrix), Ct (collagen bundles), P (patella), angled white arrow (mesenchyme lamina), * (articular-growth plate junction), Sm (synoviocyte/villi)

3.2.4   Increased MSCs and musculoskeletal phenotypes in *Ali34*

An increased number of mesenchyme cells were evident at marginal zones and the patella in *Ali34* animals (Fig. 33) In control, normal encroachment of undifferentiated stellate-shaped mesenchyme cells was present at the terminal perichondrium contiguous with articular cartilage (Fig. 33A,B). In *Ali34*, the fibrous zone was increased in mesenchyme cellular thickness compared to control (Fig. 33E,F). In control, the synovial (villi) connective membrane runs contiguous with the overlying fibrous capsule. In *Ali34*, the synoviocyte number was increased suggesting potential low-grade inflammation/irritation or metaplasia. The extensive folds in the *Ali34* membrane could lead to islets of cartilage via metaplasia of the synovial fibroblasts (i.e. synovial osteochondromatosis), thereby leading or potentiating the observed ectopic phenotype.

Tendon development was monitored in alcian blue stained sections. Tendons normally appear dense, with longitudinal collagen bundles and elongated fibroblasts lying between the collagen fibers (Fig. 33C,D). Distal to this tensile region, tendons bifurcate and wrap the sesamoid patella before insertion into bone. The tissue at the contact surface of the insertion is characterized by collagen fibers and an increased restricted focal expression of extrafibrillar aggrecan (i.e. fibrocartilage). Adjacent the fibrocartilage, toward the outer curvature of the tendon, lays a pool of loose mesenchyme cells capable of bone formation. Under normal conditions, this population of mesenchyme cells is restricted aside the fibrocartilage-tendinous

Figure 34. Musculoskeletal phenotype
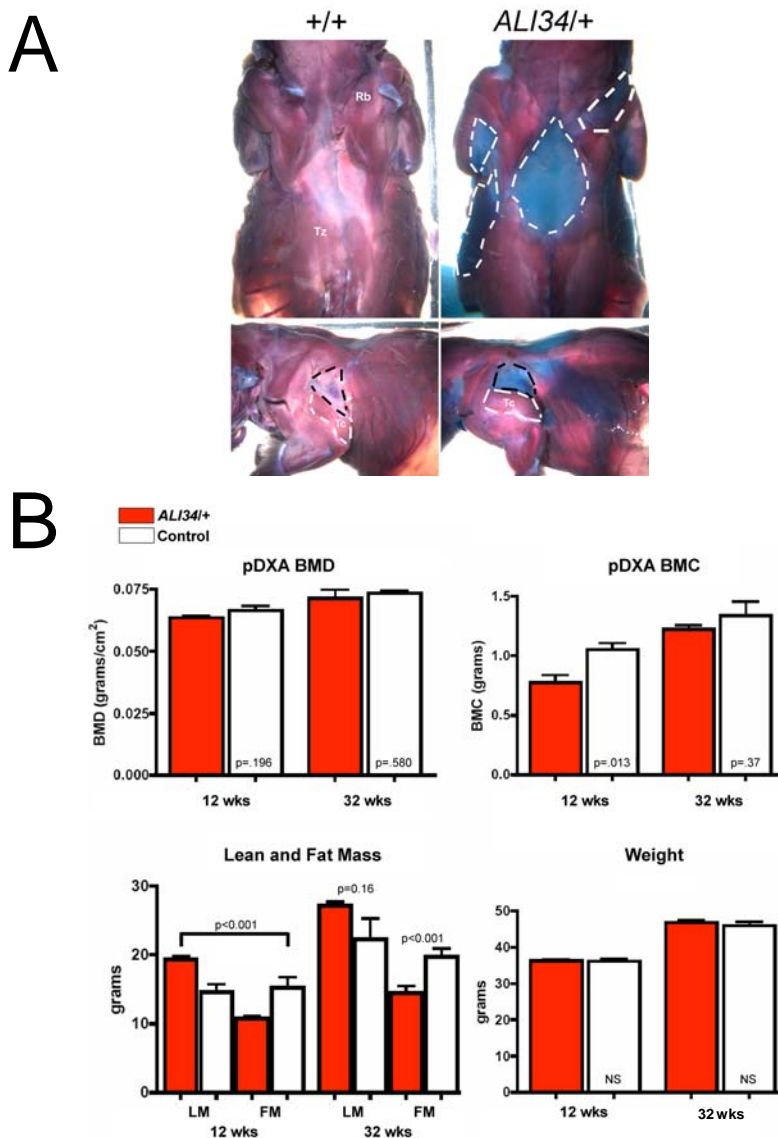
(Fig. 34). In *A*, alizarin red and alcian blue musculature staining in 12-week-old eviscerated animals. In *B*, DXA analysis of littermate control and *Ali34*/+ male mice. *p* values derived from ANOVA w/ Students t test, where the error bars represent mean ± SD, and *n* equals 6 animals. (Tz) trapezius, (Rb) rhomboideus, (Tc) tricep, LM (lean mass), FM (fat mass)

junction via basement membrane lamina structures. Although fibrocartilage development during tendinous insertion is a normal phenomenon, cartilage elements were embedded further within *Ali34* tendon as isogenous metaplastic groups when compared to control (Fig. 33G,H; white arrows). In addition, an increase in tendon fibers was observed in *Ali34*

The aforementioned musculoskeletal phenotypes were further confirmed by analyzing alcian blue stained carcasses and DXA measurements. In *Ali34*, both underlying layers of muscle and fat reserves contained large deposits of cartilaginous elements (Fig. 34A). Both

the underlying apex of the trapezius along the lumbo-dorsal line and rhomboideus extending from the vertebral border of the scapula towards the mid-dorsal line were alcian blue positive in *Ali34*. Furthermore, a distinct positive region was present directly above the triceps. Peripheral DXA analysis highlighted the musculoskeletal phenotype in both younger and older *Ali34* male cohorts (Fig. 34B). Whole body mineral density BMD and weight were not affected in *Ali34*. BMC was decreased due to shorten limbs, while older animals were able to regain bone mass after epiphysial closure. Lean mass content in *Ali34* was significantly increased presumably due to the inclusion of dense cartilaginous elements, while a concomitant decrease in fat mass was observed.

3.2.5 Mapping and identification of the *Ali34* locus

In order to successfully identify the *Ali34* mutation, the outcross-backcross strategy onto the parental strain was utlized due to strong modifying effects (Fig. S20). For chromosomal mapping of the *Ali34* mutation, a high throughput genome-wide SNP platform was utlized to haplotype 20 phenotype-positive N_2 animals (Fig. S21). The combined strategies resulted in *Ali34* linkage on chromosome 6.

During the course of positional cloning the *Ali34* locus, several skeletal-related candidate genes were analyzed (Fig. 35). At the beginning of high resolution mapping, the largest candidate region dictated by the SNP haplotyping results contained *Mgp* (matrix Gla protein; MGI:96976), *Wnt5b* (wingless-related MMTV integration site 5B; MGI:98959), and *Galnact2* (chondroitin sulfate GalNAcT-2; MGI:1926002) as potential causal genes based on text mining searches (Genomatix Software). All three genes are known to be expressed in cartilaginous tissues, and known to regulated chondrocyte growth and maintenance. Initially, both *Mgp* and *Wnt5b* coding regions were sequenced, but no mutation was identified (data not shown). Upon further haplotype analysis, both *Mgp* and *Wnt5b* were excluded from the new candidate window.

Subsequently, *Galnact2* became the next most likely candidate gene. GalNAct-2 (GalNAcT transferase 2) is responsible for biosynthesizing the repeating disaccharide units of chondroitin sulfate and is key to proper proteoglycan function within cartilage. Mutations in such classes of enzymes are known to cause chondrodysplasias and diastrophic dysplasias (179). The coding region of *Galnact2* was sequenced, but no mutation was identified. The non-coding regions (i.e. > 1000 bps of the 5' UTR, 3' UTR and all introns and predicted promoter regions) were sequenced (performed by diploma student Christian Cohrs; data not

shown), but no mutation was identified. Despite a strong functional correlation, *Galnact2* was eventually excluded as a candidate gene.

Soon thereafter in a recent publication, *Plxnd1* (plexin D1; MGI:2154244) deficiency was shown to induce axial skeletal anomalies (i.e. deviated vertebral columns) in a targeted knock out murine line (180). Partial similarities of the skeletal phenotypes between both lines suggested *Plxnd1* as the potential causal gene. Plexin D1 is a membrane receptor protein involved in vascular development, and interacts with semaphorins (i.e. protein signals that guide nerve and endothelial cells) and presumably to other semaphorin receptors like neuropilin for blood vessel growth along proper paths. *Plxnd1* was located within the new, most restricted candidate region harboring the *Ali34* locus (i.e. between D6Mit366 and SNP

Figure 35. Fine mapping of the *Ali34* locus
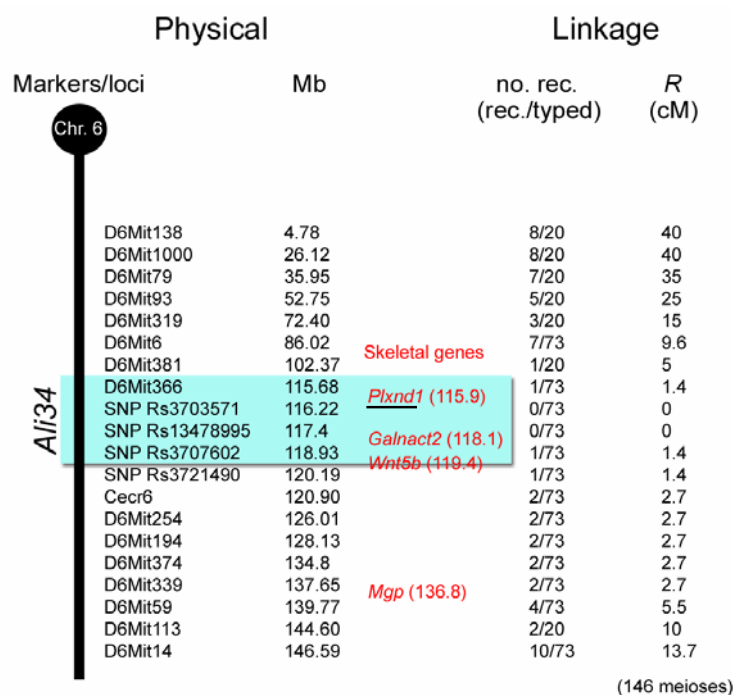
(Fig. 35) Candidate gene search on mouse chr. 6. Inclusion of the entire MS and SNP fine mapping marker sets. Of note, discrepancies in the number of recombinations reflect several markers tested only within a subset of haplotyped mice, and the recombination frequencies reflect the tested sample groups. no (number), rec (recombination), R (rec. frequency)

Rs3707602; see recombination frequencies), and this region is syntenic with human chromosome 3q21. Upon sequence analysis, a point mutation was identified in the *Plxnd1* gene that caused a premature stop site leading to a truncated protein product within the *Ali34* line (identified by Christian Cohrs; full *in silico* description of the mutation described in his

diploma thesis). The *Ali34* phenotypes recapitulate several features of osteochondrodysplasia and OA listed in OMIM entries, therefore *Ali34* represents a new mouse model and a new mechanism toward the pathologic basis of disease.

4.   Discussion

During this doctoral research project, the *N*-ethyl-*N*-nitrosourea (ENU) mutagenesis program at the GSF National Research Center in Munich Germany was utilized to help identify and characterize new genes and alleles that regulate skeletal development and homeostasis in the mouse. ENU mutagenesis is a powerful approach in identifying mouse models for human skeletal disorders (142). Subsequently, the *Aga2* and *Ali34* autosomal dominant mutant lines were cloned and phenotyped depicting distinct features of osteogenesis imperfecta (OI) and osteochondrodysplasia respectively.

4.1   *Aga2*

Type I collagen is the most studied molecule in biology, and warrants a comprehensive discussion within this dissertation. Human mutations affecting the α1/2(I) C-propeptide coding and non-coding regions have been identified less often than other types of mutations, and reflect strong variability in clinical outcomes. Some of these mutations encounter early termination codons and the mRNA is unstable or, if stable, the peptide chain is either unstable or rapidly degraded or fails to properly assemble into trimers inhibiting passage through the secretory pathway and into the extracellular space. It is assumed that in some of these cases the phenotype reflects the integrity of the pool from which normal molecules were assembled. In *Aga2*, the causal gene was mapped by linkage analysis and a C-propeptide mutation was identified in the *Col1a1* gene. Accordingly, the *Aga2* line represents a unique mouse model for type II/III/IV OI. To date, there exists no genetically-stable murine line which models OI by disruption of the terminal C-propeptide region of *Col1a1*. Three OI mouse lines have been previously described that display perinatal lethality which include the transgenic human mini-gene and *Col1a1* substitution lines, amd the Brtl knock-in line (145, 181, 182), providing unique tools in understanding OI subtype pathophysiology. The *Aga2* OI line has a more severe phenotype as judged by peri-postnatal lethality when compared to the transgenic lines, and comparable to the $Col1a1^{G349C}$ BrtlIV knock-in line. OI is an incurable debilitating human disease, and the *Aga2* line provides a valuable tool to understand both the underlying disease mechanisms and the efficacy of novel therapeutic strategies (183).

4.1.1 OI-related phenotypes in the *Aga2* line

In *Aga2*/+ embryos, no evidence of antenatal lethality was observed, suggesting congenital effects. *Aga2* homozygotes died earlier than Mov-13 embryos (i.e. a tissue-specific *Col1a1* null mutant line (184)), further supporting the dominant negative nature and early developmental defects of the *Aga2* mutation. Like other murine and human OI cases, long-bone fracture incidence was mitigated after the pubescent growth period (Table S6), suggesting possible adulthood adaptation due to an age-specific modulation of OB activity (185).

The *Aga2* skeletal phenotypes resembled many OI characteristics (30). Lethal *Aga2* animals resembled human OI-II probands, while surviving animals displayed overlapping clinical features of both types III and IV OI. Many forms of OI are associated with high bone turnover. But it remains unknown how much of the skeletal pathology was caused by high-turnover osteopenia due to metabolic effects, and how much to intrinsic matrix defects caused by the collagen or other mutations. To help elucidate these uncertainties, both *in vitro* and *in vivo* studies were performed to better understand cell autonomous versus regulatory defects. The histomorphometry and biochemical serum results indicated increased bone turnover in *Aga2*. The elevated numbers of OBs and OCs at bone surfaces hinted towards increased proliferation and/or life-span of the cells, arguing for alterations in progenitor lineage pools and cell fate decisions. It is unclear if the changes in *Aga2* cell differentiation and fate were mediated via cell autonomous cell-cycle controls or entirely dependent on the ECM environment alone (186). Our *in vivo* histomorphometric results depicted more surfaces undergoing new bone formation and an elevated BFR due to collective work performed by more ALP-positive active OBs. Our *ex vivo* studies showed that *Aga2* OBs deposited less collagen matrix, commonly seen in human OI samples (187), and were overly active and less temporally differentiated, thus inhibiting the bone functional unit by way of delayed nodule condensation, maturation and improper mineral binding (50, 185, 188). The metabolic activity of primary *Aga2* OBs was elevated likely reflecting the adaptive stress response and prolonged duration in the matrix-synthesis phase. Limited density and reduction in maximal cell growth rates in both primary OB and dermal fibroblast *Aga2* cultures were identified (see later). Despite levels of other ECM components at more mature levels (see later), *Aga2* and OI cells are generally considered fetal-like or less differentiated (50). Thus in *Aga2*, the number of remodeling cycles which occurred on a given bone surface per unit time was elevated, although matrix assimilation during a single remodeling cycle was reduced and unable to

balance net mineral accretion (Fig. 18; (189)). Although our MAR results were in disagreement with the *oim/oim* studies (i.e. a recessive murine OI line; (185)), the difference may reflect alternative mechanisms toward adaptive tissue mineralization.

Previous interpretations of increased cortical cell density were attributed to increased osteocyte numbers (188). By contrast, the increased inclusion of distinct mature OBs within *Aga2* mineralized bone was observed (Fig. 8A), and our *ex vivo* studies corroborated the tissue organization (Fig. 22). As osteocytes are the only cells in bone which can recognize the need for homeostatic remodeling, the disrupted osteocyte syncytium in terms of OB displacement, microfractures, and severely stressed surface OBs and lining cells (see later), constitutively influenced *Aga2* adaptive events (190).

Matrix deposition is a cooperative response where the pre-existing template induces matrix deposition. In *Aga2*, collagen deficiency was amplified by causing an inherent cycle of defective renewal. High bone turnover partially involves the OC's ability to respond to the surface via $\alpha_v\beta_3$ integrins for commencement of catabolic bone remodeling events (185, 191). BSP (a member of the SIBLING [small integrin-binding ligand, *N*-linked glycoprotein] family of genetically related proteins) contains the RGD (Arg-Gly-Asp) adhesive motif and can interact with cellular integrins to induce OC adhesion and function (39). Importantly, BSP and osteocalcin were significantly upregulated within *Aga2* OBs, potentially modulating OC and OB renewal, and nucleation and composition of crystals via circulation and/or discrete binding to the matrix (185, 192).

4.1.2 Bisphosphonates

Bisphosphonates affect OCs and rates of bone resorption by blocking the 3-hydroxy-3-methylglutaryl-CoA (HMG-CoA) pathway involved in cell membrane prenylation. Studies have shown that bisphosphonates reduce fracture incidence and improve bone density and size in children and adults with OI (193). However, doubts still persist concerning the effect of these drugs on bone properties such as ultrastructure and composition, particularly in the growing patient (194). Many forms of OI depict elevated bone turnover rates leading to osteopenia. Addressing metabolic imbalances, presumably caused by the abnormal bone matrix itself, may ameliorate many of the consequences of the collagen mutations, even though the mutations still remain. The third-generation bisphosphonate alendronate was applied to *Aga2* growing animals to evaluate the potential anabolic response in a severe form of OI (Fig. S17). Despite the fact that the newly accumulated matrix during treatment was still

functionally limited, inhibition of OCs resulted in sustained mineral deposition in *Aga2* treated animals. ALP levels were significantly reduced in alendronate-treated *Aga2* animals possibly due to direct effects on osteoblastogenesis, and/or a secondary response to deposited bone (195). Likewise, it is uncertain if the large gain in *Aga2* bone mass was due to apoptosis suppression or cross talk, as bisphosphonates were previously shown to promote OB survival via apoptosis inhibition (196). Based on our results, it is conceivable that a remodeling imbalance was in favor of OC activity that inhibited normal bone thickening over time in *Aga2*. Our preclinical studies demonstrates that alendronate was effective in reducing fractures in a growing mouse model of OI, and was also an important indicator of potential positive outcomes of third-generation bisphosphonate therapy in children with type II OI. Side-effects were observed during treatments, and further considerations are necessary (i.e. by performing detailed pharmacokinetic studies). Although such a pharmacological approach failed to address the underlying cause of OI, the efficacy of the treatment warrants further investigation. All in all, our results indicated that increased bone resorption was a key pathologic basis of disease in *Aga2*, which led to part of the systemic hormonal response (see later).

4.1.3 *Aga2* growth plate defects

Aga2 growth plates were more prone to fractures as observed during histological preparations, suggesting either primary structural damage, or increased fractures due to secondary bone defects. In the *Aga2* epiphysial growth plate, loss of restricted ALP expression, a surrogate of nascent assembly of matrix vesicles (MVs) and late-stage chondrocyte differentiation, was present (Fig. S12). MV proteins (e.g. ALP and annexin V) are known to interact with site-specific proteins of ECM osteoid in order to control mineralization (42). In *Aga2*, the epiphysial growth plate chondrocytic profile and the hyaline cartilage surrounding the articular joint surfaces appear normal from a histoanatomical point of view, reflecting the normal early phase biogenesis of MVs. On the other hand, the level of ALP expression in *Aga2* growth plate was suppressed at the zone of overt calcification and chondrocyte disintegration. This implied that the second (late) phase of MV genesis (i.e. the propagation and accumulation of MVs onto the collagenous ECM) was defective. Kirsch et al. (1997) (197) showed colocalization of types I, II, and X collagens along with annexin V in the growth plate cartilage. These findings suggest that type I collagen is situated close to the chondro-osseous junction and directly facilitates hydroxyapatite growth from the ruptured

MVs. Hence in *Aga2,* the limited expression of ALP at the growth plate may represent loss of MV binding. Furthermore, it is possible that alterations in *Aga2* proteoglycans, for example in their interactions and/or expression, could regulate, inhibit, and exacerbate the effects of MV assimilation in the ECM. Of note, PTH receptors are known to be expressed at reduced levels within growth plate chondrocytes, but are upregulated during pre-hypertrophy (198). And recently, PTH was shown to induce cell cycle delay of chondrocyte hypertrophy, strongly suggesting possible direct influences of elevated PTH on *Aga2* epiphysial plate and endochondral bone development as a possible cause for reduced ALP expression (see later; (199)). These results suggest that the transition toward bone formation was affected in *Aga2* growth plates possibly owing to altercations in chondrocyte function, and cartilage vascularization, degradation and mineralization, thus disturbing endochondral bone growth and rendering trabeculae functionality obsolete.

4.1.4 *Aga2* pro-α1(I) biosynthesis and fibrillogenesis

In many lethal C-propeptide-determined OI cases, there exists a degree of heterogeneity regarding the biochemical consequences of mutated and normal propeptide chains, and the corresponding clinical phenotypes (200-202). The procollagen triple helix precedes from the carboxyl to amino end, and this association is modulated by correct folding via intra-chain disulphide bonds in the C-propeptide region before chain association and inter-chain disulphide linkage (33). In certain C-propeptide OI-II lethal conditions, the mutated pro-α1/2(I) chains can associate with normal chains to form secreted triple helical procollagen molecules despite alterations in endogenous disulfide bonds (112, 200), while in other lethal cases chain formation with the mutated propeptide is entirely or largely precluded (201, 203). Based on these results, the lethal OI phenotypes are heterogeneously derived from structural and/or cellular metabolic defects. The presumptive disruption of a crucial beta sheet in *Aga2* likely destabilized protein conformation, thus affecting proteolysis and preferential chain assembly (Fig. S7-9; (204)). At the biochemical level, significant reduction in secreted pro-α1(I) chains and increased retention of aberrant procollagen molecules within *Aga2* cells were reported, therefore producing minimized collagenous matrix for deleterious ECM formation. Moreover, the majority of aberrant chains were wild-type in nature, and the mutated pepsin-resistant collagenous product was detected at degraded levels. Thus, it is conceivable from the secretion defect that *Aga2* molecules interfered with the assembly of wild-type chains into disulfide-linked trimers (Fig. S14). Also, overmodified chains in media preparations were

never observed (Fig. S13), suggesting that the mutated chains were not incorporated into the collagen fibrillar matrix. Likewise, the normal 2:1 ratio of α1(I):α2(I) chains was observed in the media suggesting secretion of normal mature type I collagen. Of importance, the ~60 % decrease in secreted collagens into the media (Fig. 21C) is consistent with the protein suicide model proposed by Prockop (205). These findings strongly suggest that *Aga2* chains were not assembled into secreted trimers and intracellularly degraded, but did not exclude alternative, aberrant disulfide bridging with wild-type chains via the newly incorporated cysteines to cause the severe phenotype.

The final aspect of procollagen processing was compromised in *Aga2*, whereby the fibril arrangement and native collagen structural network were severely altered affecting the overall biomechanical tissue and cellular properties for growth and maintenance (Fig. 19). The fibrillar cross-linking defects in *Aga2* may have developed due to post-translational changes of nascent or mature pro-α1/2(I) secreted chains, or dysfunction of critical matricellular proteins known to regulate proper fibrillogenesis (39). Further biochemical studies are needed to understand the contributing factors toward ECM instability and emanating responses in *Aga2*.

4.1.5 Hormone response in *Aga2*

The modular mechanisms which influence cell number and activity toward tissue homeostasis are ambiguous in OI. Bone homeostasis partly involves the physiological regulation of extracellular Ca^{2+} levels via parathyroid (PTH) and calcitonin (CT) peptide hormone signaling in OBs and OCs respectively (18). *Aga2* animals were induced to chronic hyperparathyroidism due to elevated bone resorption. The larger mobilization of Ca^{2+} from bone stores in *Aga2* males correlated with a smaller, yet deleterious shift in the PTH-CT axis, suggesting possible anomalies in periodicity and/or sex-specific factors. The elevation in CT was likely a secondary response to high bone turnover to maintain adequate mineral supply in *Aga2*. The larger percentage increase in CT compared to PTH implicated the greater demand for mechanisms aimed at lowering serum Ca^{2+} levels (i.e. inhibiting OCs). But despite the increase in CT, bone turnover remained elevated indicating that the increased OB and OC activity was likely regulated at the local level and was not suppressed even in the face of a physiological increase in CT.

The biological consequences of heightened PTH and CT are elusive within OI (188), which may involve cross talk with OB apoptosis inhibition (206, 207), and also affect

epiphysial plate and endochondral bone development (199) as already seen in *Aga2*. In one study, OI-II cells were less responsive to PTH challenge compared to OI-I/III/IV cells, implicating potential PTH resistance among *Aga2* OBs as well, and further affirming the adaptive offset of PTH. The PTH resistance may reflect the greater challenge of apoptosis suppression in severely stressed (apoptotic) OI-II cells. Low-dose intermittent administration of PTH is known to generate anabolic effects, whereas OBs continuously exposed to high amounts depict catabolic responses toward bone formation, raising important concerns about potential homeostatic PTH-mediated tissue loss in *Aga2* (18). Importantly, due to the unregulated hormonal profile in *Aga2*, multifactorial changes in plasticity, fate and behavior of progenitor and mature cells are expected, and likely influenced homeostatic bone remodeling and body composition development either directly or via actions of mediators. Also, other molecules which antagonize PTH (e.g. beta-arrestin 2) can modulate the final response (208). Elevated PTH and CT clearly played an influential part of the *Aga2* disease process, although whether any desirable therapeutic intervention is deemed beneficial remains to be determined.

Leptin is a hormone that plays a key role in regulating energy intake and expenditure. Recently, the involvement of the sympathetic nervous system (i.e. part of the autonomic branch involved in stress control towards homeostasis) in regulating bone formation has gained considerable attention (see review; (2)). The proportion of leptin is correlated with the amount of fat reserves in the body. *Aga2* animals have less fat composition, and presumably the leptin concentration was also reduced. Normally, when leptin activates cells in the hypothalamus (i.e. via transport and targeting of LepRb receptors on neurons), neurons secrete the currently unidentified hypothalamic OB inhibitory factor (HOBIF), which when released, lowers the matrix-making ability of OBs. As experimental studies have failed to identify leptin receptors on OBs, this implies a central, neuroendocrine regulation of bone metabolism. Furthermore, leptin can regulate bone remodeling by influencing the differentiation of OCs. Another part of this central control mechanism involves neural peptide Y (NPY) and its Y2 receptor, which presumably stimulates HOBIF release. Thus, a loss of either NPY or leptin would reduce HOBIF and increase OB productivity, as seen in *Aga2*. It is clear that *Aga2* animals have deficiencies in energy metabolism (see later), and whether circulating levels of leptin regulate energy and bone metabolism in *Aga2* remain to be determined.

4.1.6   ER stress and degradation within *Aga2* cells

Collagen turnover is critical for tissue homeostasis in establishing proper procollagen chain stoichiometry. Many disorders result from the cells inability to export mutated proteins and enzymes from the ER, including OI (62, 209). Depending on the nature of the mutation, incorrectly folded pro-α1/2(I) molecules are managed via multipartite highly regulated sorting pathways in order to retain ER homeostasis and to prevent the secretion of abnormal proteins. Studies have shown that certain mutated C-terminal pro-α1(I) chains are selectively degraded in the ER (112). BiP/Grp78 (binding protein/glucose-regulated protein 78) is a central regulator of ER function due to its transient roles in protein folding and assembly, targeting misfolded protein for degradation, and controlling the activation of transmembrane ER stress sensors. BiP chaperone was shown to bind to pro-α(I) chains derived from three cell strains which harbored unique C-propeptide mutations that inhibited chain association and inter-chain disulfide bonding (111), and mediated intracellular ER-degradation (112). Contrarily, mutations that inhibit folding in the triple helical domain of type I procollagen chains do not result in abnormal BiP binding or induction even though the aberrant molecules are retained within the ER (210). Despite these findings, the more downstream roles of the BiP-dependent ER stress responses are still unclear.

In *Aga2*/+, the presence of dilated ERs and accumulation of aberrant procollagens in the ER strongly support intracellular trafficking defects and degradation within the proximal region of the secretory pathway. We speculate that aberrant procollagen molecules aggregated into vesicular structures (Fig. S1B), which may have been part of the proteasome. Degradation did occur within more distal secretory compartments by the presence of lysosome-like structures (211), likely reflecting the fate of excessive unassociated pro-α2(I) chains, for example. In *Aga2*/+ OB cultures treated with ascorbate, BiP levels were upregulated, but not enhanced over time, implicating its constitutive involvement during ER stress. BiP was likely sequestered to the exposed or introduced interfaces of *Aga2* mutated chains which presumably triggered stress transducers. Heat-shock protein of 47 kDa (Hsp47) is an ER-resident molecular chaperone part of the 'quality control' system for procollagens under normal and stress conditions, and enhanced in certain OI cases (212). In our studies, the degree of Hsp47 induction was more prominent than BiP, but not greater than Gadd153 at later time points. Thus, in *Aga2*/+ both BiP and Hsp47 appeared to be distinctly regulated possibly due to differences in gene regulatory domains. Also, the side-effects of the

degradative process (e.g. feedback of N/C-propeptides) are unknown which may have developmental and growth consequences in *Aga2* (66).

Our findings were consistent with observations made by Willing et al. (213) which investigated a human OI family that harbored a partial *Aga2* homologous mutation in the 3' end of *COL1A1* (Fig. S6; (81)). Although the authors categorized the patients as having type I OI, surviving family members reflected mildly-to-severely affected cases suggesting clinical heterogeneity as in *Aga2*. The authors were unable to identify the aberrant pro-α1(I) chain, indicating that it was likely degraded via endogenous cellular pathways as also suggested in *Aga2*. Subsequently in a report by Fitzgerald et al. (110), the fate of mutated C-propeptide chains from the proband described by Willing et al. and another truncated C-terminal cell strain were tested, whereby the cytoplasmic proteasome was involved during intracellular degradation. These results suggest the potential activation of a similar proteasome-mediated degradative pathway within *Aga2* cells. Although cryptic mRNA transcripts from the mutated *Aga2* allele were available for translation, unstable mRNA decay, alternative splicing, and/or anomalies in transport from the nucleus to the cytoplasm due to secondary structure may have also mediated low-level translation of mutant chains (214). Although the mutation described in Willing et al. yielded steady-state levels of mutant *COL1A1* mRNA in both the nucleus and cytoplasm, interference of the intervening frameshifted region in *Aga2* with proper terminal translation cannot be excluded.

The cytoprotective unfolded protein response (UPR) involves the activation of complex regulatory ER stress signaling (ERSS) mechanisms which can either repress protein synthesis or upregulate ER-resident chaperons and other translation regulators (114). Under normal conditions, BiP is known to prevent transducer activation by binding directly to the sensors. Upon ER stress, BiP suppression of sensor activation is released by sequestration, and the sensors are then activated through oligomerization and translocation. The ATF6 (activation transcription factor 6) transducer is known to enhance transcription of ER chaperone genes (e.g. BiP). Importantly, activation of the PERK (PRKR-like ER kinase) transducer is known to upregulate the expression of ATF4, which in turn leads to transcription of pro-apoptotic Gadd153. Under prolonged ER stress, cell death ensues due to a switch from pro-survival to pro-apoptotic signaling events. Thus in *Aga2*/+ cells, it is presumed that BiP sequestration by aberrant procollagens led to the activation of individual sensor molecules, most notably PERK and ATF6, and likely facilitated retrotranslocation towards degradation. Although previous studies showed the increased synthesis of BiP in OI-II cells, it is unclear if BiP played a functional role in the terminal regulation of ER homeostasis (111). In our study

we demonstrate that both Hsp47 and BiP choreographed the intracellular regulation of mutant type I procollagens with concomitant induction of apoptosis.

4.1.7 *Ex vivo* and *in vivo* evidence for increased apoptosis in *Aga2*

Many diseases are associated with either inhibition or increase of apoptosis (215), but to date the active involvement of apoptosis during OI pathogenesis is inconclusive. Caspase-12 is a specific mediator of the ER stress-induced UPR within skeletal tissue (129). In primary *Aga2*/+ OBs, removal of the procaspase-12 adaptor protein-binding domain was evident, and the processing of procaspase-12 demonstrated the ER stress origin of mutated pro-α1(I) initiator signals. A reduction in maximal cell growth rate was observed only in ascorbate-stimulated *Aga2*/+ cultures attributed, in part, to decreased cell survival. The significant growth increase within unstimulated *Aga2*/+ cultures suggests the ability to efficiently clear mutated chains under resting states, thus bypassing cell loss. The presence of increased activated caspase-3 and TUNEL-positive OBs in *Aga2*/+ primary culture and periosteum implicated a greater tendency towards apoptosis commitment and cell death, respectively. The greater caspase-3 *versus* caspase-12 response suggests the convergence of alternative intrinsic and/or extrinsic initiator pathways independent of the ER (e.g. mitochondrial cytochrome c and Apaf-1, cytokine death receptors), either *Col1a1*[Aga2]-linked or unlinked. Likewise, the increased DNA fragmentation may have derived from caspase-independent mitochondrial pathways (216, 217).

Although several models have been proposed for the direct activation of caspase-12, possibly by calpain (129), the entire process has yet to be described. The Bcl2 (B cell leukemia 2) family of proteins are well-established components of the apoptotic machinery, some of which are associated with ER stress pathways. For example, Bim (Bcl2-interacting mediator of cell death) activates caspase-12 via translocating from the dynein-rich ER compartment upon stress, while Bcl-xL (Bcl2-like 1) couples to Bim and suppresses its translocation (126). BiP is known to inhibit caspase-mediated cell death by forming complexes with procaspases 7 and 12, and BiP disassociation facilitates procaspase activation (127). Gadd153/CHOP (growth arrest and DNA damage inducible gene/C-EBP homology protein) is a transcription factor key in the regulation of cell growth, differentiation and ER stress-induced apoptosis. Gadd153 induces death by promoting ER client protein load and oxidation via transcription of target genes which mediate apoptosis, presumably leading to caspase cascades (114). In our studies, Gadd153 was highly induced over time, and was

presumably triggered by mutated procollagens and the modulation of ERSS which activated, in part, the PERK-ATF4 pathway. Of interest, the anti-apoptotic component Bcl2 is down regulated during ER stress conditions attributed to Gadd153 upregulation, leading to enhanced oxidation and apoptosis (218). Thus, given the upregulation of Gadd153 within *Aga2*/+ OBs, Bcl2 was likely down regulated, exacerbating and contributing to cell death. From our primary culture studies, we propose the coexistence of both cytoprotected and apoptotic cells, although it is unclear to date whether the latter exclusively originated from the lethal cohorts. Despite the upregulation of BiP, the Gadd153-dependent apoptosis-inducing pathway dominated over time and provided, in part, the cellular conditions toward cell death in severely stressed *Aga2*/+ cells. Further studies are necessary to elucidate the pro and anti-apoptotic components that modulated the severe clinical outcome in *Aga2*/+ animals.

Although bone turnover rates and micro damage have been positively correlated with osteocytic apoptosis (219), empty lacunae were absent in *Aga2* possibly reflecting the altered topography and resistance within cortical bone. Whether the lack of cortical lesions in *Aga2* was correlated with the tissue regenerative capacity and access to progenitor pools remains unknown. Moreover, the lack of cortical perforations may have evolved from the production of anti-apoptotic signals from the dysregulated cortical cells themselves (220). Lastly, the selective death of incompatible OBs within the periosteum and the survival of robust cells only capable of maintaining and reasonably interacting with the defective ECM, may have generated these findings.

It is noteworthy to mention that the antagonizing intrinsic (e.g. pro-survival signals) and physiologically relevant extrinsic (e.g. prolonged PTH) effects on the life span of surviving or dying OBs are uncertain in *Aga2*. Likewise, the contribution of increased cell death on homeostatic bone turnover (i.e. progenitor replication) and adaptation of adjacent cells and afar, are unclear. To this end, it is conceivable that the elevated frequency of *Aga2* apoptosis may have directly influenced higher cell turnover rates in order to maintain the population doubling-time as was observed comparing two inbred mouse strains with unique OB apoptotic rates (221). Our findings suggest that an ER-dependent apoptotic mode of cell death contributed to the pathologic depreciation in nodular bone formation and network observed both in culture and *in vivo*.

4.1.8   Systemic effects

The cause of death in OI is debatable. For example, some clinical investigators suggest kyphoscoliosis as being the primary cause of death, as it presumably affects respiration and causes cardiac failure (222). The results obtained from the primary clinical screen of the GMC were analyzed and interpreted to help identify potential genotype-specific defects within multi-organ systems . The results obtained from the primary screen are only preliminary and offer insights into potential extraskeletal biological networks which may have been compromised during the *Aga2* pathological state. The syndromes induced by the *Aga2* mutation are holistically simple: Type I collagen is ubiquitously expressed and interacts with many molecular substrates which govern developmental, cellular, physiological and biomechanical maintenance of the entire body (29, 223). Given our findings, further experiments are needed in order to fully understand the etiology and consequences of the observed changes within *Aga2*.

4.1.8.1 Clinical chemical screen

Apart from the bone metabolism-related alterations discussed earlier, other changes were found implicative of either extraskeletal organ dysfunction and/or dietary deficiencies. First, total protein levels were slightly increased, suggestive of systemic tissue injury in *Aga2*. Hypocholesterolemia and lowered triglyceride levels were identified in *Aga2* plasma which are known to be risk factors for respiratory disease, hemorrhagic stroke and cancers (224-226). There was a weak link established between lipase activity and triglyceride levels in female *Aga2* mice. These decreases suggest either cell fate anomalies at the MSCs level (e.g. dominance of myoblast differentiation as type I collagen is known to regulate precursor differentiation) or increased energetic demands of *Aga2* mice (e.g. a secondary reduction of body fat deposits). Type I collagen is known to be expressed by muscle myoblasts, and OI patients are known to have laxed ligaments and poor muscle tone. *Aga2* male mice resulted in statistically significant creatinine and creatinine kinase levels suggestive of muscle atrophy or hypertrophy, although the results could reflect the handling of the mice, not myopathy. Kidney and liver parameters were normal, although a closer examination may result in fine differences undetected using the applied strategies (227). Although kidney contains very little type I collagen, secondary effects due to calcium disturbances, for example, may cause renal complications. All examined electrolytes were within the normal range in *Aga2*.

In *Aga2*, the lowered amylase activity is suggestive of digestive problems potentially due to zinc deficiency. Zinc is an important cofactor in many enzymes such as amylase and ALP, and skeletal fractures and tissue repair mechanisms sequester zinc for proper tissue homeostasis (228-231). Zinc deficiency is known to cause many connective tissue disorders such as mitral valve prolapse, striae, myopia, poor wound healing, scoliosis, and pectus excavatum. *Aga2* animals have an increased risk of fractures, therefore it is hypothesized there exists an increased zinc demand, thus leading to decreased amylase activity. OI patients are known to have reduced serum zinc levels (232), further supporting possible anomalies in zinc metabolism within *Aga2*.

From the hematological findings, *Aga2* animals had minor hypochromic anemia, which may be due to chronic inflammation and/or defects in iron-binding elements and globin synthesis (see later). Reduced hemoglobin synthesis in humans has been attributed to low zinc levels in blood (233). Also, hemoglobin deficiency may be regulated by blood loss or dilution due to (skeletal) injuries. Based on this finding, *Aga2* tissues may be hypoxic and sustain severe systemic effects over time. The increased white blood cell count suggests a clear immunological response to bone injury. The Immunology screen of the GMC also detected many altered parameters in lymphocytes, although the results are not within the scope of this dissertation (data not shown).

It is clear that inherited monogenic and multifactorial disorders such as OI and osteoporosis, respectively, are influenced by defective and combinations of genes, but environmental factors also affect the disease outcome. There are a number of (metabolic) disorders which are either subtly affected or treatable by dietary intervention (restriction/diversion/replacement), but this has to be considered in terms of the degree in which the respective pathologies are well understood (234). Environmental effects such as nutrition on connective tissue disorders have only been superficially considered in a handful of disorders such as OI (vitamin C), osteopenia/osteoporosis (vitamin C, K), Rickets (magnesium, vitamin D, calcium), mitral valve prolapse (magnesium) and Marfan and Ehlers-Danlos syndromes (PubMed Clinical Query; (231, 232)). The nature of connective disorders resulting from abnormalities in either the metabolism or function of collagen, for example, is specifically concerned with susceptibility to (systemic or skeletal) injury and complications governed partially by environmental interactions. One part of the environmental equation is nutrition, and the critical aspect that nutrition as a major contributor in the pathogenesis of diseases that were once regarded solely dependent on the gene defect alone, should now be considered. The aim in understanding the relationship between bone metabolism and

environmental interactions is to re-direct the current efforts toward musculoskeletal management to treatments that are less invasive, potentially more effective and less expensive than current modalities. All in all, the data obtained for the clinical chemical screen was suggestive of systemic tissue injury in *Aga2*. Furthermore, the data suggested that the inherited connective tissue disorder was influenced by environmental factors such as nutrition, and supplementation should be considered in the future.

4.1.8.2 Cardiology screen

Valve defects and cardiovascular disease have been observed in patients with OI (235, 236). Furthermore in human OI patients, general muscle strength is known to be reduced (237), further supporting muscle atrophy (see Clinical chemical screen) in the *Aga2* line. In *Aga2*, several ECG parameters were altered in a genotype- and sex-dependent manner, suggesting either morphological and/or conductive anomalies of the heart (Table 6). The observed tachycardia in *Aga2* may indicate increased sensitivity towards the anesthesia administered during the ECG recordings, particularly under the condition of anemia. No cardiac arrhythmias were observed in *Aga2* animals. The JT interval is a measurement of the transition form ventricular depolarization to ventricular repolarization, and was increased in *Aga2*. Thus, *Aga2* may have deficiencies in repolarization of the ventricle due to either ventricular defects and/or electrolyte disturbances. In *Aga2*, the QRS complex amplitude was increased suggesting morphological abnormalities such as hypertrophy (e.g. enlarged ventricle), and valve (e.g. mitrial stenosis) and conduction defects (e.g. blockage in the *his* bundle). Furthermore, electrolyte (e.g. subtle increase in $[Ca^{2+}]$) and tissue non-specific ALP disturbances in *Aga2* may have cause pathological mineralization of tissues (e.g. in vasculature) which may have affected the function of the heart among other organs (238, 239).

The myocardial collagen matrix of the interstitium (i.e. perimysial and endomysial locations) and the perivascular regions consists of a fibrillar network of types I and III interacting collagens which are intimately connected to myocytes in a parallel manner (240-242). The fibrillar collagens exhibit a high tensile strength due to extensive cross-linking that plays a crucial role in ventricle response during the cardiac cycle. In myocardial tissue, type I collagen represents approximately 80 % of the total collagen protein, while type III collagen is presented in lower amounts (11 %) synthesized by cardiac fibroblasts. The *oim/oim* mouse model was shown to contain less perimysial collagen and lowered passive uniaxial and

ventricular stiffness, all of which influences the mechanics of the ventricular myocardium (59). Furthermore, the transmural myofiber angle was increased with elevated residual stresses, which was assumed to be beneficial adaptive responses in *oim/oim* heart. Accordingly, the findings from the cardiology screen clearly reflected pathophysiological changes due to the connective tissue defect in *Aga2*, and warrant further investigations into potential cardiomyopathy and myocardial infarctions. Also, the consequences of the cardiovascular dysfunction on other organ systems have to be considered. Last, the functional consequences of potential altered collagen cross-linking in the heart should be further considered in the *Aga2* model given cross-linking anomalies found in dermal collagens.

4.1.8.3 Lung screen

Spontaneous breathing parameters were monitored via body plethysmography in *Aga2* mice during the lung screen. Sex differences in *Aga2* respiratory frequency during rest (i.e. lower in males) were observed. The rest to activity transition was nearly the same, potentially excluding muscle damage. There was an exception in the reduced mean expiratory flow rate, emphasizing possible atrophy to the lungs in *Aga2* animals. A closer investigation of the data showed that the weight to TV and MV plots was, for the most part, linear in both sexes in tested control animals (data not shown). On the other hand, *Aga2* animals depicted non-linear relationships under similar circumstances, implicating genotype-dependent effects on these two lung parameters irrespective of weight influences. Of note, simply normalizing TV and MV by weight provides little information given this non-linear relationship. Irrespective of potential interference from the chest wall, for example, the subtle anemia uncovered in *Aga2* would also suggest gas exchange anomalies potentially explaining the elevated parameters.

These data hinge toward mechanical or other defects affecting respiration in *Aga2*. The lung parenchyma and stroma networks contain type I collagen-secreting fibroblasts, suggesting possible primary defects in the lung (54). Nevertheless, the differences observed in *Aga2* must be considered in terms of: 1.) the severe weight deficient, and 2.) the deformity of the chest wall as a result of rib fractures and fragility, and spinal distortions. These considerations are known to affect the performance of the lungs (243). These changes affect the mechanical properties of the lung, compromising local ventilation and perfusion with a negative impact on gas exchange. Given these considerations, a more detailed analysis of the

parameter-weight relationships, histology, EM, and invasive lung volume and gas exchange measurements are necessary in order to differentiate the primary and secondary effects.

4.1.8.4 Survival, aging and metabolism

The *Aga2* line is a severe-to-lethal mouse model of human OI. Postnatal lethality in a subset of animals clearly indicated reduced survivability. Furthermore, surviving animals after weaning also succumbed to a reduced life span (Fig. 16). The reduced survival in *Aga*2 is related to the molecular nature of the type I collagen mutation, as *oim*/*oim* animals (i.e. affecting the α2(I) chain) and mildly affect human OI probands (i.e. affecting N-terminal regions) have normal life spans (59, 222). Weis et al. (2000) (59) alluded to the possibility of fiber alterations as a pro-survival adaptation towards normal cardiac function and lifespan of *oim*/*oim* animals. Furthermore, adaptation in *oim* may overcome subtle changes in kidney defects which nevertheless resulted in a normal life span observed in a different study (227). As this adaptive hypothesis may be correct, other organ systems besides the heart and kidney were likely affected which play a part in survivability. One argument against the data from the *Aga2* primary screen is that, in fact, all the observed changes due not suggest pathologic functioning of the tissue systems analyzed, but rather a positive adaptation of the genetic defect as was suggested in the myocardial studies on the *oim* line (59). In contrast, the fact that *Aga2* animals have altered parameters from the screens and combined reduced life span argue against long-term positive adaptation.

Bone quality in *Aga2* was affected, but it was not the underlying cause of mortality during OI. Data from both the *Aga2* and *oim* lines argue against spinal deformity, for example, as the sole cause of death in OI. The cause of death in *Aga2* was multifactorial and influenced by the quality of life. The simple fact that there existed a gradation and clinical heterogeneity, suggests other effects (e.g. epistatic, environmental, malignancy) which also contributed to mortality. Patients with milder forms of OI are known to have normal life spans (i.e. like the *oim* line) and presumably die due to 'un-related' illness such as malignancy (222). It is argued that malignancy may be directly linked to the type I collagen defects based on its function (see Introduction). In aged *Aga2* animals, the female cohort was malignant and developed tumors of unknown origin at a higher rate. The tumor incident in *Aga2* females (~66 %) was much higher than those reported in mildly affected OI patients, further suggesting malignancy as correlated with disease.

Glycation is a non-enzymatic process resulting in the binding of sugar molecules (e.g. fructose or glucose) to proteins or lipids either intracellular or extracellularly, and is implicated in many chronic diseases such as diabetes mellitus, cardiovascular disease, Alzheimer disease, cancer and blindness. Type I collagen contains ligand-binding sites for glycation proposed to be important in mediating diabetes and aging (244, 245). Metabolically-active cells known to synthesize type I collagen (e.g. OBs and fibroblasts) are at high risk for damage. Whether the altered cross-linking within *Aga2* fibrils influences the binding of advanced glycation end products, thus potentially resulting in chronic aliments, remains to be determined.

Increased metabolism was a risk factor for lowered survival rates in *Aga2*. To date there are no published reports on energy metabolic changes in OI murine models. From the primary screen, mutant females showed a higher energy uptake and metabolized energy demand compared to males. Based on ANCOVA analysis, the changes in E_{up} and E_{met} were most likely due to genotype-specific effects in *Aga2*. The cellular bases of the elevated metabolic demand in *Aga2* are unknown. The altered body composition in *Aga2* mice may have influenced the observed energetic demands. Furthermore, our *in vitro* and *in vivo* analysis depicted *Aga2* OBs as overly active, therefore one would expect energy demand was increased based only within this particular niche.

4.1.8.5 Expression profiling

From the microarray analysis, four known genes were found to be upregulated, while ten genes were down regulated in *Aga2* lung tissue. Hemoglobin is the most abundant iron-containing oxygen-transport metalloprotein in erythrocytes of blood. The hemoglobin molecule is constructed of four globular protein subunits, whereby each subunit is a globin chain tightly complexed with a non-protein heme group. The anemia identified in the clinical chemical screen was confirmed in the chip analysis, suggesting alterations in gas exchange/transport within *Aga2* alveoli as one cause of defective lung functioning. It is unclear whether the acute anemia identified in *Aga2* led to further organ damage and circulatory problems seen in hemoglobinopathies such as sickle-cell anemia and beta-thalassemia syndromes (246). Hemoglobin is synthesized in a complex series of reactions, whereby the heme group is produced in both the mitochondria and cytosol of immature erythrocytes, and by ribosomes in the cytosol for the globin protein. From the chip analysis, coupling results were observed by way of upregulated transcripts known to mediate the

hemoglobin complex. For example, biliverdin reductase A (Blvra), an enzyme which catalyses heme degradation (247), was found to be transcriptionally upregulated in *Aga2*, while protoporphyrinogen oxidase (Ppox), an enzyme crucial in the heme biosynthetic pathway generating protoporphyrin for iron binding (248), was also upregulated. Moreover, there was a nominal fold difference between Blvra and Ppox (Fig. 4), excluding dominance of one transcript change over the other. Collectively, these results suggest that both heme group and protoporphyrin catabolism and synthesis were dysregulated with concomitant down regulation of the hemoglobin alpha chains in *Aga2*.

Senp6 (SUMO/sentrin specific peptidase 6, also known as SUSP1) was upregulated in *Aga2* lung tissue. Small ubiquitin-related modifier (SUMO) processing is mediated by sentrin specific/ubiquitin-like proteases (Senp) involved in biological functions such as reproduction (249). SUMOs, unlike ubiquitin, do not target proteins for degradation, and the biological function of SUMO conjugation is clearly unknown, although potentially playing an indirect role in the function of proteins such as p53 and c-Jun (250). Senp6 is localized to the nucleoplasm and known to play a role in dismantling conjugated SUMO2/3 species, whereby the control of these species is key for upkeep of nuclear structures like promyleocytic leukemia bodies (251). Senp6 is known to contain zinc finger, peptidase C48, and heme peroxidase protein domains, suggesting a potential link to the hemoglobin dysregulation in *Aga2*. The transcriptional control of Senps is entirely unknown to date, thus making the interpretation difficult. Furthermore, other Senp proteases (e.g. Senp2) have been shown to mechanistically regulate c-Jun-dependent transcription, which in turn plays an important role in cell growth, differentiation, transformation and apoptosis. It is unclear how upregulation of Senp6 in *Aga2* affected cell-type specific c-Jun or other kinase activities, or downstream SUMO modifications which can use other transcription factors as substrates toward the final cellular outcome. Hypothetically, upregulation of Senp6 could suggest a change in the adaptive maintenance of the nuclear structures, whereby *Aga2* OBs, for example, are known to involve increased nuclear atrophy.

Mark3 (MAP/microtubule affinity-regulating kinase3) is also known as C-TAK1 (Cdc25C-associated kinase 1) or PAR1A, and was down regulated in *Aga2* lungs and has been implicated in cell cycle regulation (proliferation) and Ras signalling via its kinase activity and protein phosphorylation (252, 253). Mark3 interacts with two putative substrates: the Cdc25C (cell division cycle 25C) phosphatase and the MAPK (mitogen-activated protein kinase) scaffold KSR1 (kinase suppressor of Ras 1), thereby facilitating the phosphorylation reactions required for the activation of MAPK kinase (MEK) and MAPK. Despite available data on the

protein regulation of the different kinases, no data on the transcriptional regulatory mechanisms or conditions are available for Mark3 to date. Nevertheless in the context of *Aga2*, down regulation of Mark3 may have occurred due to growth factor autoregulatory changes known to regulate components of the cell cycle machinery on the transcriptional level (e.g. via EGF receptors). Growth curve analysis of both *Aga2* OBs and dermal fibroblast further support this hypothesis.

RhoB protein is especially enriched in lung tissue (GeneCard: GC02P020568) and constitutes one member of the Ras superfamily of small GTP hydrolases implicated in mediation of apoptosis in transformed cells, the cytoskeleton, intracellular proteins and vesicle trafficking during development, protection form UV-induced apoptosis, and cell motility, polarity, migration, survival and cycle progression during development (254, 255). Most Rho/Rac GTPases act as switches, for example when bound to GTP, whereby the activated GTPases bind to effector molecules (e.g. AKT) to induce a cellular response via signal transduction pathways. Recently, RhoB was shown to be necessary for stability and nuclear trafficking of prosurvival kinase AKT1/AKT, thus promoting longevity during (retinal) vascular development (255). In principle, loss of RhoB could lead to promotion of apoptosis, whereby RhoB is known to inhibit the induction of apoptosis in certain tumors and suppress malignant tumors (256). In *Aga2* lung tissue, RhoB was down regulated, suggesting a certain degree of influence on cell survival. Whether there is a link between down regulated RhoB and the prosurvival kinase AKT in the determination of *Aga2* cellular survivability remains unknown. Although speculative, repression of RhoB in *Aga2* may be manifold and specialized. For example, apart from subcellular localization, cell polarity and integrin mediated control of Rho/Rac proteins, reduced expression of RhoB mRNA in the context of *Aga2* may have occurred by external stimuli including growth factors and cytokines regulated by specific promoter elements (257, 258). This scenario is feasible in *Aga2* given the increased fracture rate and strong immunological response obtained from the primary findings from the Immunology screen (data not shown). Also, it is unclear why molecules and pathways which are known to be antagonistic to RhoB and Mark3 (e.g. RhoA and Ras; (256)) were not dysregulated in *Aga2*. One hypothesis is that RhoB was the only molecule in the Rho/Rac pathway that was differentially regulated large enough for detection using the cDNA chip technology. Nevertheless, within *Aga2* both the RhoB and Mark3 signal transduction pathways are worth further investigation.

Rlf (rearranged L-myc fusion sequence), a zinc finger protein, was found to be down regulated in *Aga2* lungs. Rlf is largely expressed in fetal and adult tissues, and may play a role

in general transcriptional regulation (259). Within the *Aga2* context, it is unclear whether the observed dysregulation reflected anomalies in zinc ion binding (as suggested during the Clinical chemical screen) or transforming abilities within the lung environment. Grrp1 (glycine/arginine rich protein 1) was transcriptionally down regulated in *Aga2*, although the biological relevance is unclear since there are no publications referencing this novel protein.

Tysnd1 (trypsin domain containing 1) is a recently characterized protein localized to the peroxisomes (260), and was down regulated in *Aga2* lung tissue. Peroxisomes are involved in a variety of anabolic and catabolic pathways (e.g. cholesterol biosynthesis, fatty acid oxidation, purine metabolism, hydrogen peroxide detoxification, bile acid synthesis, plasminogen synthesis, and amino acid metabolism). Two distinct peroxisomal signal targeting sequences (PTSs), the C-terminal PTS1 and the N-terminal PTS2, are known to be specifically present in peroxisome enzymes/proteins which are then transported to the membrane from the cytosol. Tysnd1 is known to remove the PTS2-containing leader peptide from prethiolase, and for the specific processing of all PTS1 proteins involved in the peroxisomal beta-oxidation pathway of fatty acids. These results suggest that Tysnd1 is specifically affected in *Aga2* cells, which may be part of the molecular cause of the observed lowered triglyceride and cholesterol levels detected in the Clinical chemical screen. The molecular mechanism for Tysnd1 down regulation requires further investigation.

Asporin is a novel member of the class I small leucine-rich repeat proteoglycan (SLRP) family containing an unique stretch of aspartate residues in the amino terminus (261). Asporin mRNA is primarily expressed in the skeleton and other specialized connective tissues like tendon, sclera, and fascia. Asporin mRNA is also expressed in the periosteum of long bones at 18.5 dpc, while biglycan (i.e. a homologous SLRP protein) is expressed later. Within the lung, asporin is presumably localized to the cartilage elements of the upper respiratory track. The down regulation of asporin in *Aga2* may have reflected the regionalized expression pattern of cartilage within lung. The majority of the SLRP proteins are proteoglycans, whereby one functional role may involve the modulation of collagen fibril assembly along with close homologue decorin, for example (39). Asporin has also been implicated during chondrogenesis, and its role in the pathogenesis of OA has also been suggested (262). During chondrogenesis, asporin is thought to act as a negative regulator of mineralization via potential modulation of BMP-2 (262). Therefore within the context of *Aga2*, it is feasible that down regulation of growth plate asporin may act to dysregulate proper mineralization at the osteogenic zone of the primary spongiosa during endochondral bone formation. Growth plate anomalies have been observed in *Aga2*, one of which included reduced ALP activity in

hypertrophic chondrocytes (Fig. S12). The similarities and dissimilarities in asporin mRNA expression patterns and tissue distribution during development with other homologous SLRP subfamily protein classes like decorin and biglycan may eventually explain the redundancy of each protein product. Although the functional role of asporin is unclear, i.e. much like other class I SLRP molecules, it may play both a structural and signaling function which was likely disrupted in *Aga2* (263). It would be interesting and important to therefore establish a role for asporin during OI pathogenesis. The conditions which caused asporin down regulation (e.g. via cytokine, stress fiber, cytoskeleton, growth factor) within *Aga2* are clearly unknown to date.

Tap1 (transporter 1, ATP-binding cassette, sub-family B) is an immunological protein which is involved in the transport of antigenic peptides from the cytosol to the ER, binding to newly synthesized major histocompatibility complex (MCH) class I molecules. Subsequently, peptide-bound complexes are expressed on the surface cell membrane and then recognized by antigen-specific CD8+ T cells. Homozygous deletion of the *Tap1* gene resulted in decreased cell membrane class I complexes leading to low levels of CD8+ T cells (264). In *Aga2* lung tissue, Tap1 transcript was down regulated. In *Aga2* peripheral blood, the Immunology screen identified a clear immunological phenotype (data not shown). *Aga2* peripheral blood contained increased T cell populations, but CD8+ cells were unchanged, thus conflicting the down regulation of Tap1 mRNA transcript seen in lung. Currently, both the interpretation of the results and transcriptional regulation of Tap1 are ambiguous.

Nucleoporin 155 (Nup155) is a component of the nuclear pore complex involved in mediating bidirectional trafficking of cellular molecules such as mRNAs and proteins between the nucleus and cytosol (265). In vertebrates, Nup154, also a major component of the nuclear pore complex (NPC), is essential for viability in Drosophila (266). Presumably, the down regulation of Nup155 in *Aga2*/+ animals should affect cell viability as well. Within the context of *Aga2* lung tissue, it is not obvious how Nup155 transcript levels were transcriptionally down regulated, although it may have been due to the consequences of increased rate of nuclear damage in *Aga2*.

All in all, more *in vitro* transcriptional and protein analyses are needed to help elucidate the findings from the Expression profiling screen. The multicellularity of the lung tissue led to difficulties in data interpretation. Lung is highly vascularized at the alveoli, further justifying the blood changes observed in the Clinical chemical screen. It is unclear if the transcriptional dysregulation occurred within a specific subset of lung cells and constituted only one member of a larger pathway. Importantly, it is unknown if the differentially

'regulated' genes reflected tissue loss, or 'real' transcriptional regulation. The results partially reflected skeletal damage and fracture repair, and the consequences of inflammation on transcriptional regulation of many cell types (68).

4.1.9   Clinical heterogeneity and osteoblast metabolism

There is no simple explanation for the genotype-phenotype relationship observed in OI, and the *Aga2* OI line will facilitate this understanding (188). Upon a rigorously controlled environment and a homozygous genetic background, the *Aga2* mutation caused clinical heterogeneity strongly suggesting that, for the most part, variability resulted from the inherent presence and associations of the mutated collagen gene. A maternal effect was also uncovered in *Aga2*, whereby maternally-derived wild-type littermates depicted a non-pathological, yet significant, 5 - 7 % reduction in BMD at adult stages when compared to baseline normal and reciprocal controls (data not shown). These features are important for genetic counseling of families with known C-terminal mutations, especially when the first child is perinatal lethal and mother is affected. This would implicate that although perinatal lethality occurred, the chance for a child to be moderately affected are possible, although the otherwise normal child would develop maternal defects. There is no general consensus based on mouse (145, 182, 267) and human (188) OI studies of a correlation between transgene and protein expression levels with disease severity. Instead, it is more conceivable that the divergent intrinsic nature and type of mutation (e.g. apoptosis-inducing), functional capacity (e.g. post-translational modifications, non-collagenous factors, cell adhesion, tissue-specificity), maternal effects and/or other uncharacterized stochastic events (e.g. nutrition, activity, environment) are key regulators of phenotype diversity in OI. The *Aga2* mutation may not only regulate the variable phenotypes via its influence on bone integrity, but also its pronounced systemic role within other tissue systems (see later).

In addition to its function as a mediator of collagen assembly in the secretory pathway, the C-propeptide of type I procollagen is known to act as a signaling molecule in the extracellular matrix affecting cell growth and differentiation, and it was hypothesized that the potential structural defects could interfere with this activity and contribute to, and complicate, the molecular pathogenesis of OI in *Aga2*. Therefore, it is unclear how structural changes caused by the *Aga2* C-propeptide mutation may have altered the communication with cells in the ECM reflective of the phenotype. The *Aga2* mouse line offers the unique opportunity to better identify potential targets which influence the range of phenotypes.

Recently, Forlino et al. (2007) (113) evaluated phenotype heterogeneity within the BrtlIV knock-in OI mouse line, and identified increased Gadd153 transcript and protein levels within calvaria of lethal animals, suggesting the involvement of 'bone-specific' apoptosis. Interestingly in non-lethal BrtlIV calvaria, the over expression of the anti-apoptotic heat shock protein αB crystalline was observed, implicating cytoprotection against ER stress. The matrix was found to contain both mutant and normal molecules similarly cross-linked with the same efficiency in both non-lethal and lethal Brtl animals, suggesting post-translational modifications do not modulate OI phenotypes in certain cases (268). In light of both our and the recent findings, questions arise as to whether variable OI outcomes are more influenced by aberrant interactions of mutant collagen molecules with other ECM components or anomalies in OB metabolism and function rather than to changes in structure or physical interactions among mutant collagen molecules. The molecular diversity of apoptosis in OI is unknown, and it is unclear if the apoptotic program is a phenomenon of type I procollagen mutations that severely affect chain assembly and retention caused by triple helical versus C-propeptide structural defects, or by both. In this study we isolated and characterized a unique mouse model for OI, and provided evidence that the *Aga2* C-propeptide α1(I) mutation induced ER-mediated osteoblast apoptosis that affected cellular function and metabolism, which we now suggest to be a key component, among others, that influenced disease severity in the disease.

4.1.10 Future perspectives and conclusion

Despite these findings, many detailed aspects regarding the assembly, processing and structure of type I procollagen molecules in *Aga2* cells remain unknown. The next phase would entail the monitoring of the extent of potential overmodification of α1(I) chains via mapping of cyanogen bromide fragments. Also, it would be important to study the kinetics of molecular assembly and secretion of collagenous molecules assayed via pulse labeling experiments. And lastly, the thermal stability of secreted collagens should be determined. It is hypothesized that in *Aga2* there is delayed trimer assembly and diminished secretion of type I procollagen molecules, and the total amount of procollagen produced may be reduced. It is also hypothesized that the melting temperature of secreted collagens from *Aga2* cells is the same as normal collagens (i.e. helix stability is not affected), despite the presumed delayed assembly and increased modification as judged by other C-propeptide α1(I) mutations (91) and preliminary results obtained before. It is assumed that in *Aga2* there exists a normal

relationship between adjacent chains in the trimer, as opposed to the effects of mutations that occur in the triple helical domain. Furthermore, it is unclear what changes occur in the *Aga2* triple helical molecule once procollagen is completely folded.

Apart from elucidating the procollagen defects, further characterization of the ER-stress response in *Aga2*, in particular the activation of the proteasomal and ubiquitination pathways toward aberrant chain degradation is necessary. Continued investigation into the regulation of molecular apoptotic pathways in both affected primary cells, and in cell lines or primary cells which over express the *Aga2* col1a1 mutation using the RNase protection assay is warranted. Specific long-term objectives related to the *Aga2* OI line may include: 1.) Understanding the relationship between bone cells and components of the (altered) bone matrix involving signaling pathways, and the effect of collagen deficiency or structural anomalies of collagen toward such relationships, 2.) detailed understanding of the actions of bisphosphonates and growth factor therapies, and 3.) development of inducible techniques for the genetic modification of tissue-specific cells for controlled expression of the *Aga2* dominant-negative gene product to better access the syndromic effects and responses to therapies. In regard to the systemic effects, secondary and tertiary experiments should be designed to investigate potential primary defects within the identified organ systems.

In conclusion, a unique murine line for type II/III/IV OI was isolated and characterized, and then the molecular understanding of contributing factors which regulate proper cellular phenotypes, and bone deterioration and cell death was broadened (45). Our findings suggest that the large clinical heterogeneity in *Aga2* was inherent to the *Col1a1*^{Aga2} allele. Furthermore, the molecular diversity of apoptosis in OI is speculative to date. For example, it is uncertain if the apoptotic program is cell type-specific, and a general phenomenon of C-terminal propeptide and/or triple helical type I procollagen mutations that severely affect chain assembly and association. In *Aga2*, intracellular accumulation of aberrant type I procollagens promoted ER stress-induced apoptosis preceded by the cytoprotective UPR cascade. Activation of caspases 12 and 3 revealed a previously unidentified role of ER stress signaling in inducing apoptosis during OI pathogenesis.

4.2   *Ali34*

Besides studying OI, the reserve of ENU mutants was additionally utilized to broaden the understanding of molecules which regulate skeletal biology by mapping and phenotyping the *Ali34* mouse line. This line was characterized as having severe ankylosis, calvarial agenesis,

and deviated intervertebral columns involving a causal gene defect codifying an integral membrane receptor protein known to mediate vascular patterning.

4.2.1   *Ali34* locus: the plexin D1 role in blood vessel guidance

Linkage analysis and candidate gene prediction were time-consuming during the positional cloning of *Ali34* due to severe genetic modifier effects and the lack of viable literature regarding the genes within the candidate region respectively. Eventually, a premature termination mutation affecting the cytoplasmic Rho GTPase activation domain was identified in the *Plxnd1* gene as the cause of disease (see the diploma thesis by Christian Cohrs for further details). During commencement of vasculogenesis, a primitive network of vessels develops from a condensation of locally proliferating endothelial cells. Thereafter during angiogenesis, vessels arborize side branches via delamination and migration of endothelial cells that group to the avascular areas in the embryo. Upon vascular remodeling, the original small vessels localize and expand, or instead truncate to form mature, larger vasculatures that ramify into smaller branches. Signals mediated by guidance molecules and surface receptors dictate the intricate patterning of both blood vessels and axons throughout the body and in the central nervous system (see review by Carmeliet and Tessier-Lavigne (269)). Endothelial cells must migrate, not as far as growth cones, and need specialized 'tip' cells at the fronts of meandering blood vessels for motility. The tip cells proliferate minimally, and extend and retract filopodias to search the environment, while the stalk cells proliferate frequently. Importantly, growth factors are known to direct angiogenic arborization and axonal branching in a highly regulated manner.

Semaphorins and the plexin family of receptors, as examples, are crucial in the navigation and branching of blood vessels and axons to their targets acting, in general, as repulsive and attractant cues respectively. Currently, it is known that blood vessel guidance is regulated by direct binding of Sema3E to Plxnd1 receptors expressed on endothelial cells. Axonal growth cone guidance is dependent on Sema3A binding to neuropilin1 receptors that induced signaling via plexin co-receptors. Contrarily, it is unknown whether the Sema3A-neuropilin1-plexin receptor complex influences vessel navigation. Disruption of *Plxnd1* in mice and zebra fish resulted in the failure of intersomitic vessels to target the correct branching sites along the dorsal aorta and are misrouted along the antero-posterior somite boundaries (270). Intersomitic vessels express Plxnd1, while the deep layers of the somites express Sema3A1 and Sema3A2, preventing the vessels from entering the intersomitic

corridors. Due to Plexin D1-mediated changes in developmental vessel patterning, axial skeletal anomalies were recently reported in mice (180), although no skeletal defects were reported in zebra fish (271). The phenotypic differences in zebra fish may be due to the evolutionary duplication of the zebra fish genome (272), i.e. the duplication of human and murine orthologues of genes via the existence of paralogues *Plxnd1A* and *1B*. Also, the difference in phenotypes could simply be due to non-reporting of the skeletal phenotypes by the authors. To date no conclusive proof that vasculature in *Ali34* was haphazardly organized in a Plxnd1-dependent fashion has been presented (see later), as was reported in the transgenic mice and zebra fish lines, and owes for further investigation. In *Ali34*, one could imagine neovascularization defects that caused alterations in the balance between cellular inhibition and promotion as a result of changes in nutrient (e.g. growth factors) flow causing both bone loss and overgrowth, and chondrocytic anomalies within Plxnd1-dependent vascularized tissues. More detailed anatomical and immunohistochemical comparisons using specific markers of vasculature are needed.

4.2.2   Human case correlation

Hereditary congenital facial paresis (HCFP; OMIM 601471) entails dysfunction of the facial cranial nerve VII, and the susceptibility human locus *HCFP1* was mapped to chromosome 3q21 in the affected family that is syntenic for the mouse *Ali34* chromosomal region (Fig. 35; (273)). Blood vessels and nerve fibers travel throughout the body in a mutual pattern alongside each other. Blood vessels are known to generate signals (e.g. artemin and neurotrophin 3) that attract axons to migrate alongside the guiding vessels. As both mouse and human Plxnd1 receptors are known to regulate signaling among blood vessels and growth cones, it is possible that the HCFP clinical phenotype results from a mutation in the *PLXND1* gene (274). Seven human candidate genes (i.e. *KLF15*, *CCDC37*, *PODXL2*, *TMCC1*, *PLXNA1*, and *GATA2*) including *PLXND1* were sequenced in the affected family, but no causative mutation was found. Although no causative mutation was identified, regulatory and intronic non-coding regions were not excluded as potential mutational sites. More in-depth analysis is required in making this potential human association.

4.2.3 *Ali34* connective tissue phenotypes

Chondrogenesis and cartilage maintenance is mediated by cellular interactions with the surrounding matrix, growth and differentiation factors, and other environmental signals that trigger or inhibit cellular signalling pathways and transcription of specific genes in a spatial-temporal fashion. Perichondrial mesenchymal cells are bi-potential toward either OBs or chondrocytes. Thus, chondrogenesis and osteogenesis, although disorganized in *Ali34*, were destined fates for the perichondrial and connective tissue progenitors that lead to ectopic formation and metaplasia. Adaptive remodeling of cartilage is considered a normally active process, and in *Ali34* the altered transition from chondrogenesis to osteogenesis may also signal for increased repair and replenishment from the mesenchyme pool. Nonetheless, it is unclear if *Ali34* chondrocytes were rapidly turned over, in a more undifferentiated resting state and simply enlarged, or in a terminal hypertrophic state due to the presumed vascular defect. Of note, it is unknown if *Ali34* tissues featured acromegaly as an increased proliferation response to ECM damage or fibrillation commonly seen in human OA cases.

The dysmorphological observations witnessed in *Ali34* reflect differential mediation and types of tissue growth. It is proposed that interstitial growth (i.e. limb lengthening) was reduced due to loss of regulated epiphysial isogenicity. For example, it is unclear if the proliferation of chondrocytes in *Ali34* was reduced and substituted by increased distinctly enlarged resting cells. Potentially in *Ali34*, there may exist a delay in chondrocyte differentiation as was seen in a chondrodysplasic knock-in model harbouring disruption of the key cartilage matrix protein matrilin 3 (115). Appositional growth in *Ali34* was increased due to elevated number of cells adjacent to the cartilage proper as seen in other chondrodysplasic models (275). These cells were stellate in shape and proposed to be mis-guided and undifferentiated MSCs. It is speculated that the large pool of progenitor MSCs represented an avascular regions where the cells were fixed in an early state. With time, the increased appositional growth, in part, added various protuberances such as ectopic cartilage that was eventually replaced by sclerotic bone. It is further speculated that the overabundance of MSCs within these regions secondarily affected adjacent tissues via secretable factors (e.g. morphogens like BMP family members), thus compromising the overall phenotype. It is further proposed that the ablation and differential types of tissue formation reflected the abnormal, haphazard guidance and branching of vasculature at those regions.

In *Ali34*/+ adult animals, the synovial joint was severely affected (Fig. 30). The joint articular space and surface were infiltrated with ectopic cartilage and mineralized

components. The specificity of the phenotypes may reside in the detailed anatomical and developmental (bone formation) particularities of the tissue dependency on Plexin D1-mediated vascularisation when compared to non-affected regions. In essence, each joint-type (diarthroses, synarthroses, and amphiarthroses) is constructed uniquely and entails a complex mechanism involving vascularisation. The specific layers of the joint (e.g. fibrous, synovial, and articular layers) constitute individual cell types which require proper activation for differentiation. Thus, the anomalies in *Ali34* could originate from any of the fibrous zones within and around the joint capsule. If vascularisation was indeed mis-guided in the knee joint region of *Ali34*, growth factor changes could affect regional cell fate and differentiation status, which then could feed back and have paracrine effects via secreted *de novo* factors by the altered population of cells. Of note, despite the presence of mineralized tissue in articular spaces of *Ali34*, it is still unclear if this represented ossification (i.e. the presence of OBs and then osteocytes) regardless of positive fluorescent labeling versus ectopic mineralization (i.e. fibrocartilage ECM mineralization).

Cartilage is a hypovascular tissue that exhibits powerful angiogenic resistance, implying the presence of tissue-type specific inhibitors of angiogenesis. Vasculature expresses specific guidance molecules involved in proper targeting of channels for nutrient delivery. Chondromodulin-I (ChM-I) is a tissue-specific inhibitor of angiogenesis in cartilage. ChM-I is specifically expressed in the avascular regions of the growth plate and cartilaginous bone rudiments. Also, tenomodulin (another angiogenesis inhibitor) is expressed specifically in other hypovascular structures in the mesenchyme including the epimysium, tendon, and ligaments. These anti-angiogenic molecules are expressed in cell-stage specific zones during tissue development, and modulate blood vessel endothelial cell proliferation and tube formation *in vitro* and *in vivo* (276). In the *Ali34* epiphysial plate, ChM-I expression was ectopic, unorganized and circumvented a larger area, suggesting loss of proper chondrocytic arrangement and differentiation, and vascular assembly. Factors brought by vascularisation are necessary for concomitant terminal differentiation of chondrocytes that counter the anti-angiogenic molecules in the avascular-vascular zones (15, 147). Also given the changes in the ChM-I expression pattern, it is reasonable to assume that VEGF (vascular endothelial growth factor) was affected in *Ali34* growth plates as well. VEGF is specifically expressed in growth plate hypertrophic chondrocytes, a hypoxic zone which is disorganized and compromised in *Ali34*, and is an important molecule that triggers vascularisation. Furthermore, VEGF can induce secondary effects on a number of other cell types besides the vascular endothelium (e.g. monocyte/macrophage migration, neurons, cancer cells, and kidney epithelial cells).

The head develops from complex and immense transitions of mesenchymal cells derived from the mesoderm and neural crest. These cells interact with one another and the craniofacial epithelia to generate the intricate structures of the face, skull, teeth, and jaw. It is unclear if specification, emigration (delamination) and migration, proliferation, fate determination and/or survival of mesenchyme cells played an important role in the pathology of *Ali34*. The caudal portion of the skull consists of bone plates which are derived via intramembranous ossification. Intramembranous ossification occurs through a process devoid of any cartilage model, therefore bone ossification and the reliance on vascularisation occur earlier and more dependent compared to endochondral bone formation respectively. For example, in *Ali34/Ali34* embryos, the calvarial agenesis occurred prior to any condylar mandible damage, which relies on endochondral bone formation for development. The alveolar process, a less dense vascular (spongy) portion of the mandible that contains teeth, was not affected, suggesting Plxnd1's independency in this region. Furthermore there were no gross joint changes in *Ali34/Ali34* embryos, suggesting the embryos died due to the open-brain phenotype before the manifestation of any potential limb phenotypes. Thus, it is hypothesized that the presumed defect in calvarial vascularisation (i.e. occurring at the dura matter and internal/external periosteums) had more drastic early effects during intramembranous ossification compared to tissues which ossify via the cartilage model. Of note, homozygotes had no cleft palate defects, which would hint toward proper cranial neural crest cell migration and fate in *Ali34*. Furthermore, the vertebral columns were temporally less affected compared to the calvaria since they ossify via endochondral bone formation. Guidance signals or cues derived from the somites and tissue boundaries (e.g. SemA3, VEGF, ephrinB2, netrin) interact with cognate receptors (e.g. Plxnd1, Npn1, EphB3/B4, Unc5b) in intersomitic vessels. In the absence of such cues and receptors, the intersomitic vessels are misrouted, nutrients are not delivered, and bone formation and tissue morphology is compromised. For example, defects in VEGF in mouse show similar skeletal phenotypes (e.g. skull and growth plate dysplasia) as in *Ali34* (277). Nonetheless, it is still entirely unclear from our data and literature the precise role of Plxnd1 during the integrated developmental and genetic pathways which regulate proper calvarial and spinal column development.

Neoangiogenesis in cartilage growth plate plays a fundamental role in endochondral ossification. *Ali34/+* animals depict reduced trabecular bone formation (Fig. 29). In most studies depicting anomalies during chondrocytic differentiation, the downstream endochondral bone formation was delayed or defective as seen in *Ali34* (15, 276). It is unclear if the local reduction in bone formation was influenced by cell autonomous defects within the

OBs which affect activity or by a decrease in the vascular-dependent recruitment and proliferation of OBs, and/or essential nutrients to the osteogenic zone for proper bone metabolism. Tentatively, our results suggest altered localized OB activity, while bone resorption and mineralization were unchanged. Furthermore, it is entirely unclear if the mineral apposition rate was affected (i.e. predicted to be unchanged), which would give hints to any defects in OB differentiation, matrix integrity and resorptive balance in *Ali34*. Currently, it is unknown why *Ali34* results in a thicker diaphysis, perhaps due to compensatory regulation for decreased endochondral bone formation as seen in cases of dwarfism.

The transition from tendon through fibrocartilage to bone is poorly understood and may involve tendon fibroblasts capable of undergoing transformation directly to OBs. Tendons may or may not be surrounded by a fibrous synovial sheath. The sheath has both parietal and visceral layers, whereby the former is invaded by blood vessels in order to obtain nutrients for diffusion. In *Ali34*, intratendinous cartilage (predominantly at Sharpey's fibers) was excessive and deep within the muscle (Fig. 33, S19), and the DXA analysis confirmed the metaplastic consequences on whole body composition (Fig. 34). Presumably, this represented the metaplasia of tenocytes to chondrocytes, and then in some instances chondrocytes toward OBs, although entirely unclear. Tendon metaplasia in *Ali34* may have been mediated either by direct migration through a disruptive basement membrane and/or premature tenocyte transformation to fibrocartilage caused by changes in diffusible factors, for example. Lastly in *Ali34*, it is unclear if the elevated fibrocartilagenous processes of weight-bearing tendon regions were influenced by adaptive compression, trauma or ageing, altered angle of insertion (6), and/or production of ectopic neocartilage elsewhere. Further studies will help elucidate to what degree the *Ali34* morphological changes were under adaptive control, and primarily affected due to the *Plxnd1* gene defect.

4.2.4 Osteoarthritic and disease correlation

Osteoarthritis (OA) is the most common minimal inflammatory joint disease in ageing and elderly humans, and has many risk factors (OMIM: 165720; (278)). OA can occur via an early or late-onset manner due to primary or secondary causes. The main symptoms of OA include chronic pain, loss of mobility and stiffness, thus representing a clinical heterogeneity (26). These symptoms are caused by a range of biomechanical, biochemical, metabolic, hormonal and genetic factors that lead to dysregulation, degeneration and progressive loss of cartilage in

one or more joints, whereby increased apoptosis may contribute to the disease process (Fig. S1; (279)). Inflammation of the cartilage can also stimulate new bone outgrowths (spurs) around the joints. Progressive cartilage degeneration at the knee joints can lead to deformity and outward curvature of the knees (i.e. bow legs). Since there are many bases for the localized and systemic insufficiencies of cartilage proper in OA, there exists no one animal model which fully mimics all the clinical outcomes. Currently, mutations of only a few human genes (e.g. the cartilage-specific ECM proteins) have been shown to evoke OA symptoms. Several transgenic mouse lines have been established which mimic elements of OA such as early-onset pathogenesis, mild chondrodysplasia, tendon mineralization, gait impairment, and cartilage degradation (Fig. S1; (280)). *Ali34* tissues depict certain features of OA, and alternative mouse models that propose different mechanisms toward pathology are beneficial for OA research. It is proposed that the OA phenotypes depicted in *Ali34* (e.g. the degradation of cartilage ECM) was due to a secondary effect of the chondrodysplasia elicited by the vascular defect. Other mouse models also propose similar secondary OA effects (115). Other *Ali34* phenotypes were featured in OMIM entries and include: Epiphysial dysplasia (132400), osteochondromatosis (166000; i.e. benign cartilage tumors of bone), spondyloepimetaphyseal dysplasia (184250; i.e. sclerotic changes in the metaphysis of long bones), multiple epiphysial dysplasia (607078) and metaphysial acroscyphodysplasia (250215). Although several mutations and/or polymorphisms have been attributed to the above clinical conditions (e.g. PTHr1, Col2a1, Col9a2, Matn3), mutations affecting *Plxnd1* may potentially cause related phenotypes in cases where the causative gene mutations are unknown due to clinical heterogeneity, for example.

4.2.5 Implications and future perspectives

It is proposed that the skeletal phenotypes observed in *Ali34* are secondary effects due to the Plxnd1 defect, as proper vessel arborisation is known to be crucial for proper cartilage and bone formation. It is hypothesized that metaplastic and ectopic regions were either 'reintroduced' or starved of blood serum factors which promoted abnormal transformation and damage in *Ali34* tissues. Moreover, as the development of the limb bud proceeds, positional information is regulated via signalling organization centres (i.e. the apical ectodermal ridge and the zone of polarizing activity) through diffusible agents that promote the formation of the cartilaginous anlage along proximal-distal and anterior-posterior axes. These early organization centres are thought to be avascular; therefore the Plxnd1 defect in *Ali34* most

likely did not affect innate patterning of early mesenchymal condensations of mesodermal or neural crest origin. The defects in limbs were most likely attributed to the ensuing vascular-dependent local maintenance phase with regard to the spatial-temporal relationship of type of bone formation which existed.

Also, whether other key factors, in particular morphogens like Hedgehogs, BMPs and Wnts that can influence not only vessel morphogenesis, but also cartilage and bone development, were dysregulated in *Ali34* remains unknown. It is known that active components of bone matrix, for example the BMPs, can act upon tissues whose development was not stabilized to augment the genesis of cartilage. Furthermore, the use of bone matrix (degraded) components and active substances have shown that differentiation is not irreversible. In another words, BMPs for example, are capable of stimulating the re-differentiation of skeletal muscle into cartilage. Thus, secondary effects of mesenchymal-derived factors, which are presumed to be increased in *Ali34*, can have systemic effects such as metaplasia. Unfortunately, it is too premature to establish a working model for the osteochondrodysplasia observed in *Ali34* with respect to the Plexin D1 defect. It is still unclear which inhibitors and pro-angiogenesis markers contributed to the chondrodysplasia. Furthermore, it is unclear if the growth plate chondrocytes were resting, proliferating, pre-hypertrophic, intermediate-hypertrophic, late-stage hypertrophic, or apoptotic. That is to say, it is unknown if the chondrocytic cell cycle was reprogrammed, and if so, to what cell stage did the chondrocytes re-enter. Whether such mechanism exists in *Ali34* remains to be determined.

It is questionable why the *Ali34* heterozygous status depicted stronger, hypermorphic bone-related phenotypes compared to the published *Plxnd1* transgenic lines. Differences in phenotypes may have been due to cell autonomous anomalies based on the mutations (i.e. extracellular versus intracellular domains of Plxnd1), or the nature of the targeting vector used in the construction of the *Plxnd1* transgenic line (e.g. targeting of exon 1, alternative transcripts, neo cassette, random insertion, and epistatic effects). These differences in technologies and mutations could have also relayed plieotrophic effects (e.g. growth hormone signaling) that were particular to each animal line. Furthermore, it was unclear if the observed phenotypes were influenced entirely by the intracellular versus extracellular defects of the mutated molecule in *Ali34*. For example, it was possible that the mutation induced ERSS and then compromised the cell's ability to survive and properly differentiate, thus altering cellular metabolism. Moreover, whether secretable matrix factors were altered in *Ali34* remain unknown. Lastly, the physiological differences between the inbred mouse strains most likely

affected the penetrance of the disorder, thus complicating the direct phenotype comparisons between the *Plxnd1* lines.

In the future, more detailed investigations are necessary to determine how midline seam/fusion abnormalities led to complete calvaria agenesis in homozygous animals. Further investigations into the vascular dependencies of inductive interactions that specified the number and positioning of the calvarial bones, including earlier mediations and exclusions between the neuroepithelium and cranial mesenchyme are necessary (21). It was unclear if calvarial agenesis in *Ali34* was due to migratory sutural defects, altered proliferation (i.e. classical craniosynostosis), or accelerated degeneration of relevant cells. A number of animal models have been developed which show (partial) calvaria agenesis, and include signaling molecules in conserved sutural pathways apart from the proposed mechanism in *Ali34* (e.g. Msx1/2, FGFR2/4/9, BMP2/4, Shh, lmx1b, TGFß and Ptc; (22, 23, 24)). For example during skull development, conserved TGFß receptors play crucial roles in regulating the fate of cranial neural crest cells during palatogenesis. Furthermore, during skull development and formation, TGFß signaling mediates cell proliferation, not migration, in the dura matter, consequentially leading to calvarial damage.

Lastly, the misrouting of blood vessels and potential neovascularization defects in *Ali34* tissues have to be clearly characterized. It is necessary to check the overlapping expression pattern of Plxnd1 with the observed tissue phenotypes. Furthermore, potential systemic phenotypes in *Ali34* are worth investigating, for example in the Eye screen of the GMC for possible retinal vascularisation and neovascularization defects after oxygen-induced retinopathy. In this report, it is proposed that the disruption of the repellent receptor Plxnd1 in *Ali34* allowed blood vessels to travel a distance, but missed their targets for proper connective tissue organization and maintenance.

5.   Supplement

Figure S1. Developmental and homeostatic control of chondrogenesis
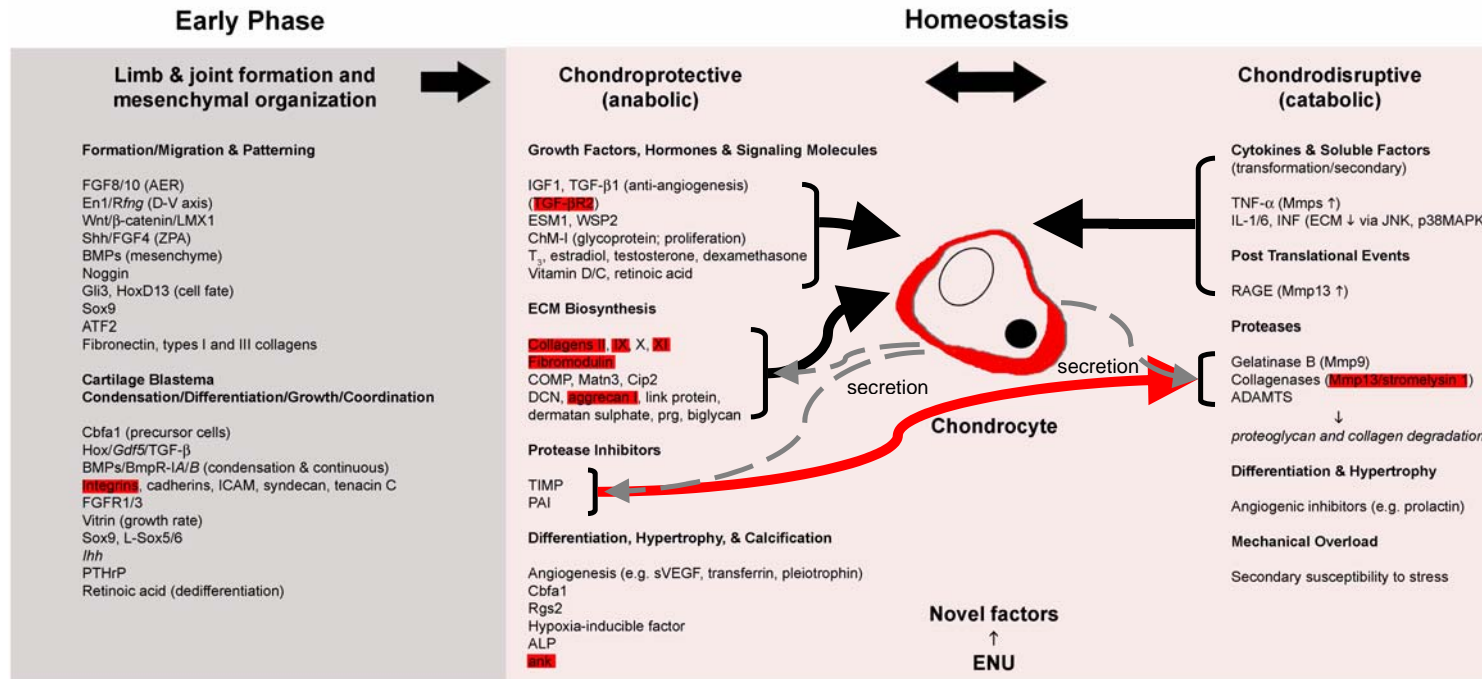
(Fig. S1) Receptor for advanced glycation end products (RAGE), EN (engrailed), rfng (radical fringe), LMX (Lim-homeobox protein), Wnt (wingless and int), ZPA (zone of polarizing activity), Shh (sonic hedgehog), BMP (bone morphogenetic proteins), Gli3 (GLI-Kruppel family member 3; Greig cephalopolysyndactyly syndrome), Hox (homeobox), Sox9 (SRY-related high mobility group-Box gene 9), ATF (activating transcription factor), ICAM (intercellular adhesion molecule), Cbfa1 (core binding factor 1), ChM-1 (chondromodulin 1), ESM1 (endothelial cell specific molecule-1), COMP (cartilage oligomeric matrix protein), matn3 (matrilin-3), cip2 (COOH-terminal interactor protein 2), DCN (decorin), ALP (alkaline phosphatase), Ank (ankylosis), Rgs2 (regulator of G protein signaling 2), VEGF (vascular endothelial growth factor), Timp (tissue inhibitors of metalloproteinase), PAI (plasminogen activator inhibitor), ADAMTs (a disintegrin and metalloprotease with thrombospondin motifs), MAPK (mitogen-activated protein kinases), JNK (c-Jun amino-terminal kinase), INF (interferon), ENU (ethylnitrosourea)

Figure S2. Overview of collagen synthesis

1. Synthesis of *col1a1* mRNA

2. Translation

3. Hydroxylation

4. Glycosylation

5. Removal of N-terminal signal peptide

6. Release of completed α-chains

7. Formation of disulfide cross-links

8. Formation of triple helix

9. Translocation and vesicle formation

10. Extrusion of molecule and removal of non-helical extensions

Sequence is collagen type specific

Inter-chain disulfide bonds not obligatory for triple helix formation

Figure S3. Synthetic triple helical secondary structure of type I collagen
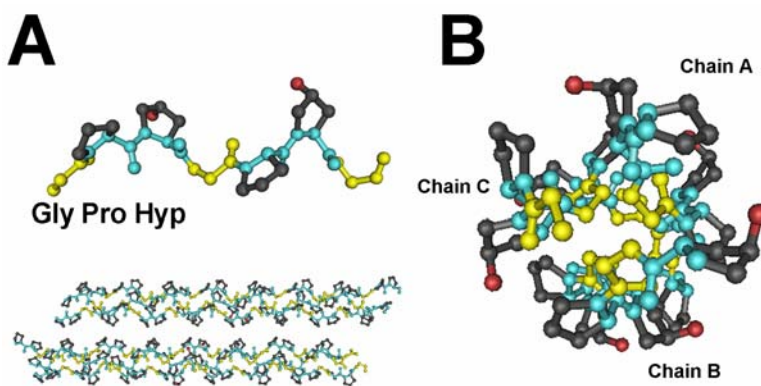
(Fig. S3) In *A*, longitudinal view of a single α-chain triple helical domain with Gly-Pro-Hyp (hydroxyprolyine)-Gly-Pro-Hyp-Gly sequence is shown, whereby the protein backbone is highlighted in blue, oxygen in red, aliphatic imino side chains of proline in dark gray, and glycine residues in yellow throughout. Two α1(I) and one α2(I) chains intercalate to form a collagen molecule, and subsequently during fibrillogenesis multiple tropocollagen molecules, held together by hydrogen bonds, assemble into fibrils (*A*, lower) and lastly into fiber bundles. The type I collagen molecule is a triple helix composed of three left-handed polyproline helices intertwined in a right-handed manner. In *B*, the end-on view of the hydrophobic central core is shown harboring glycine residues within a collagen molecule. In a space-filling model of *B*, backbone atoms tightly fill the center of the helix (not shown). All 3-dimensional ball-and-stick structures were derived using the crystal structural data from Okuyama et al. (2004) (281) using the Cn3D v. 4.1 software provided by NCBI (National Center for Biotechnology Information, NIH). Backbone hydrogen bonds are not shown.

Figure S4. Mouse *col1a1* gene sequence (from exon 47 only shown)

```
                              Exon47
3481 GGCCCCCGGGGGTCCCCCTGGCTCTGCTGGTTCTCCTGGCAAAGACGGACTCAACGGTCTC
1128 -G--P--R--G--P--P--G--S--A--G--S--P--G--K--D--G--L--N--G--L-

                                                      Exon48
3541 CCTGGCCCCATTGGTCCCCCTGGTCCTCGAGGTCGCACTGGTGACAGCGGCCCTGCTGGT
1148 -P--G--P--I--G--P--P--G--P--R--G--R--T--G--D--S--G--P--A--G-
                                              end α-chain (1181)
3601 CCCCCCGGCCCTCCTGGACCCCCTGGCCCTCCTGGACCTCCCAGTGGCGGTTATGACTTC
1168 -P--P--G--P--P--G--P--P--G--P--P--G--P--P--S--G--G--Y--D--F-

3661 AGCTTCCTGCCTCAGCCACCTCAAGAGAAGTCTCAAGATGGTGGCCGCTACTACCGGGCC
1188 -S--F--L--P--Q--P--P--Q--E--K--S--Q--D--G--G--R--Y--Y--R--A-

3721 GATGATGCTAACGTGGTTCGTGACCGTGACCTTGAGGTGGACACCACCCTCAAGAGCCTG
1208 -D--D--A--N--V--V--R--D--R--D--L--E--V--D--T--T--L--K--S--L-

3781 AGTCAGCAGATTGAGAACATCCGCAGCCCCGAAGGCAGCCGCAAGAACCCTGCCCGCACA
1228 -S--Q--Q--I--E--N--I--R--S--P--E--G--S--R--K--N--P--A--R--T-
                                     Exon49
3841 TGCCGCGACCTCAAGATGTGCCACTCTGACTGGAAGAGCGGAGAGTACTGGATCGACCCT
1248 -C--R--D--L--K--M--C--H--S--D--W--K--S--G--E--Y--W--I--D--P-

3901 AACCAAGGCTGCAACCTGGACGCCATCAAGGTCTACTGCAACATGGAGACAGGTCAGACC
1268 -N--Q--G--C--N--L--D--A--I--K--V--Y--C--N--M--E--T--G--Q--T-

3961 TGTGTGTTCCCTACTCAGCCGTCTGTGCCTCAGAAGAACTGGTACATCAGCCCGAACCCC
1288 -C--V--F--P--T--Q--P--S--V--P--Q--K--N--W--Y--I--S--P--N--P-
                                                 Exon50
4021 AAGGAAAAGAAGCACGTCTGGTTTGGAGAGAGCATGACCGATGGATTCCCGTTCGAGTAC
1308 -K--E--K--K--H--V--W--F--G--E--S--M--T--D--G--F--P--F--E--Y-

4081 GGAAGCGAGGGCTCCGACCCCGCCGATGTCGCTATCCAGCTGACCTTCCTGCGCCTAATG
1328 -G--S--E--G--S--D--P--A--D--V--A--I--Q--L--T--F--L--R--L--M-

4141 TCCACCGAGGCCTCCCAGAACATCACCTATCACTGCAAGAACAGCGTAGCCTACATGGAC
1348 -S--T--E--A--S--Q--N--I--T--Y--H--C--K--N--S--V--A--Y--M--D-

4201 CAGCAGACTGGCAACCTCAAGAAGGCCCTGCTCCTCCAGGGATCCAACGAGATCGAGCTC
1368 -Q--Q--T--G--N--L--K--K--A--L--L--L--Q--G--S--N--E--I--E--L-
                                                  Exon51
4261 AGAGGCGAAGGCAACAGTCGCTTCACCTACAGCACCCTTGTGGACGGCTGCACGAGTCAC
1388 -R--G--E--G--N--S--R--F--T--Y--S--T--L--V--D--G--C--T--S--H-

4321 ACCGGAACTTGGGGCAAGACAGTCATCGAATACAAAACCACCAAGACCTCCCGCCTGCCC
1408 -T--G--T--W--G--K--T--V--I--E--Y--K--T--T--K--T--S--R--L--P-

4381 ATCATCGATGTGGCTCCCTTGGACATTGGTGCCCCAGACCAGGAATTCGGACTAGACATT
1428 -I--I--D--V--A--P--L--D--I--G--A--P--D--Q--E--F--G--L--D--I-

4441 GGCCCTGCCTGCTTCGTGTAAACTCCCTCCACCCCAATCTGGTTCCCTCCCACCCAGCCC
1448 -G--P--A--C--F--V--*-.......................................

4501 ACTTTTCCCCAACCCTGGAAACAGACGAACAACCCAAACTCAATTTCCCCCAAAAGCCAA
     ...........................................................

4561 AAATATGGGAGATAATTTCACATGGACTTTGGAAAACATTTTTTTTCCTTTGCATTCACC
     ...........................................................

4621 TTTCAAACTTAGTTTTTACCTTTGACCAACTGAACGTGACCAAAAACCAAAAGTGCATTC
     ...........................................................

4681 AACCTTACCAAAAAAGAAAAAAAAAAAAAGA
```

(Fig. S4) The critical cystine residues involved in internal disulphide bonds in the C-propeptide region have been highlighted in red (■), while cystine residues involved in inter-chain disulphide bonds are highlighted in cyan (■). In the mouse pro-α1(I) chain, the C-propeptide cystines are termed C41, C47, C64, C73, C81, C172, C217, and C244. The entire C-propeptide region (highlighted in black, ■) is 246 residues long. Of note, the α-chain end position has been denoted. Full transcript length: 4,711 bps, and full translation length: 1,453 residues. For other key features of the col1a1 protein sequence, refer to Table S4. Untranslated region is highlighted in yellow, and exons alternate in text colors

Figure S5. F$_1$ dominant musculoskeletal screen

(Fig. S5) Double plots of DXA-derived *mineralization traits* versus *trait-weight* adjusted values of ~500 mutagenized F$_1$ male progeny at 16 weeks of age. Phenodeviants were identified as having opposed reciprocal adjusted and unadjusted measurements beyond the 3 SD range. Borderline cases may also be phenodeviants. The measured F$_1$ mean BMD and adjusted BMD values (in *A*) were 0.069 ± 0.008 and 1.002 ± 0.0001 g/cm^2 respectively, while the mean BMC and adjusted BMC values (in *B*) were 1.189 ± 0.009 and 1.745 ± 0.0219 grams respectively. Body weight-trait adjustments were calculated based on Srivastava et al (142). □ *Aga2*/+, ◆ mean, ■ Screen (*n* = 501)

Figure S6. *Aga2* C-terminal frameshift sequence

(Fig. S6) Prediction of the elongated C-terminal end of *Col1a1*^{Aga2}. Highlighted in yellow is the 16 bp cryptic acceptor splice nucleotide sequence. The red box signifies the start of the human frameshift mutation described in Willing et al (213). The frameshifted cysteine residue (C244) in both *Aga2* and the human case is underlined in black. Newly introduced cysteines are underlined in blue, while the potential *N*-linked oligosaccharide (*CHO*) attachment site is boxed in blue.

111

Figure S7. Hydrophobicity plot of the C-propeptide α(I) domain (window size 9; (282))

Control (compare from position 199 onward; consult Fig. S3)
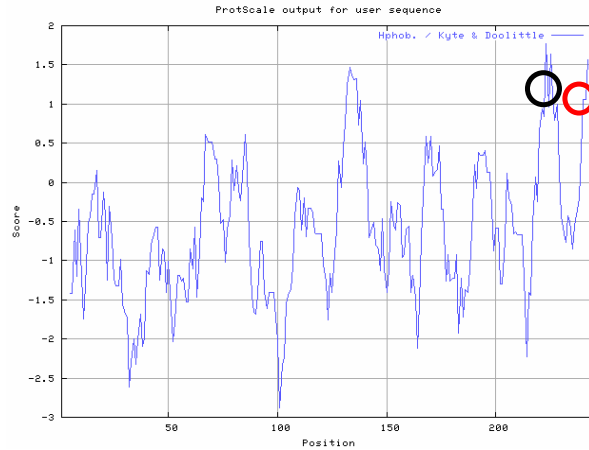
Aga2 (position 199 is the start of the frameshift)
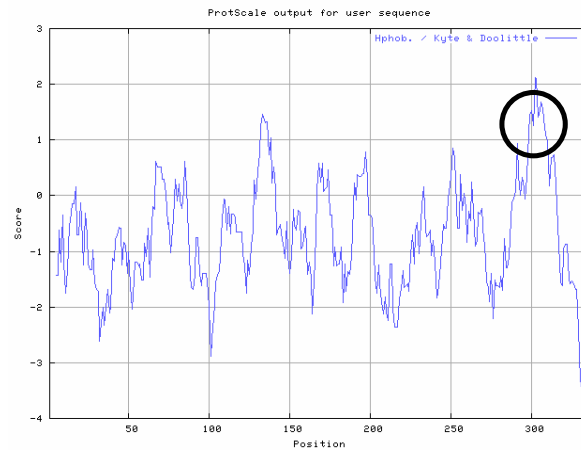
(Fig. S7) The *Aga2* frameshift removed the predicted terminal hydrophobic domain (black circle, control), and introduced a broader terminal hydrophobic domain (black circle, *Aga2*). The frameshift altered the hydrophobicity of a short loop formed by the last intrachain disulphide bond (red circle, control). Protein analyzed using ProtScale (http://www.expasy.org/cgi-bin/protscale.pl).

Figure S8. Beta-sheet prediction of the C-propeptide α(I) (window size 9)

Control (compare from position 199 onward)
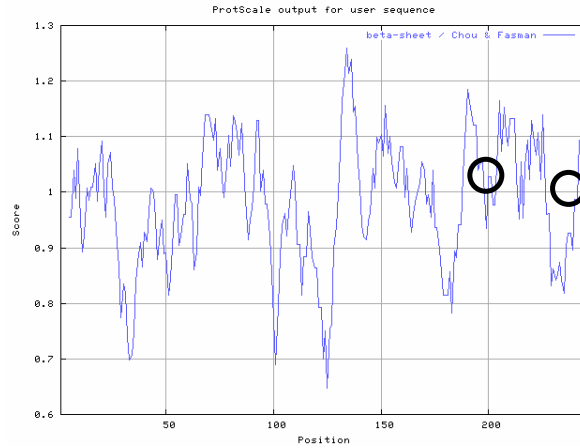
Aga2 (position 199 is the start of the frameshift)
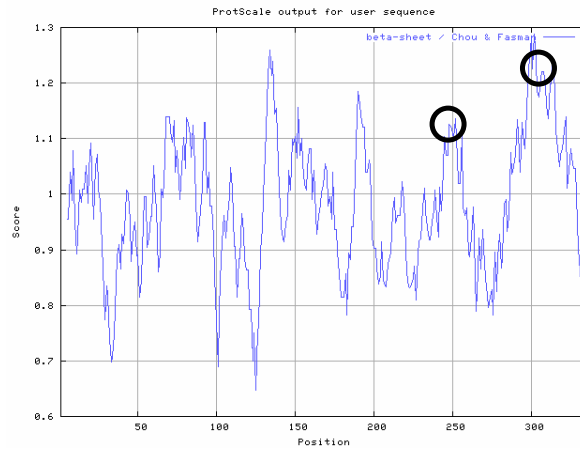
(Fig. S8) Removal of two endogenous beta sheets (black circles, control). Removal caused loss of the beta loop associated with the disulphide bridge. Introduction of new beta sheets in *Aga2* (black circles, *Aga2*).

113

Figure S9. Beta-turn prediction of the C-propeptide region of procollagen I

Control (compare from position 199 onwards)

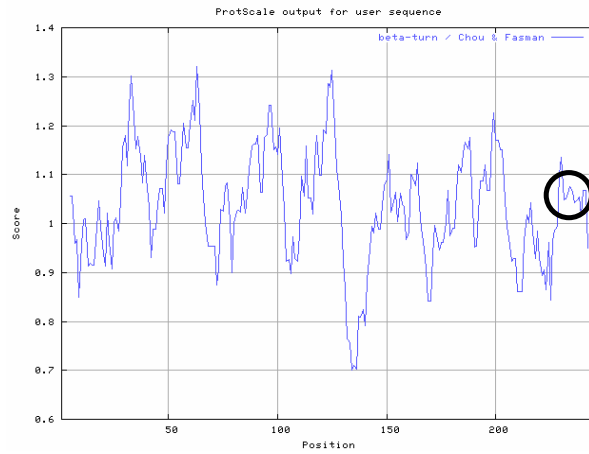*Aga2* (position 199 is the start of the frameshift)
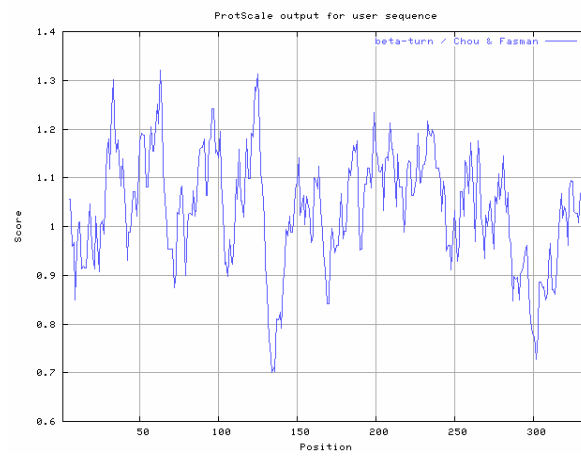
(Fig. S9) Removal of the endogenous beta turn at the very terminal end (black circle, control) resulted in alterations in the globular structure of the procollagen molecule (201, 283). No addition of any new beta turns in *Aga2*.

Figure S10. Micro CT analysis
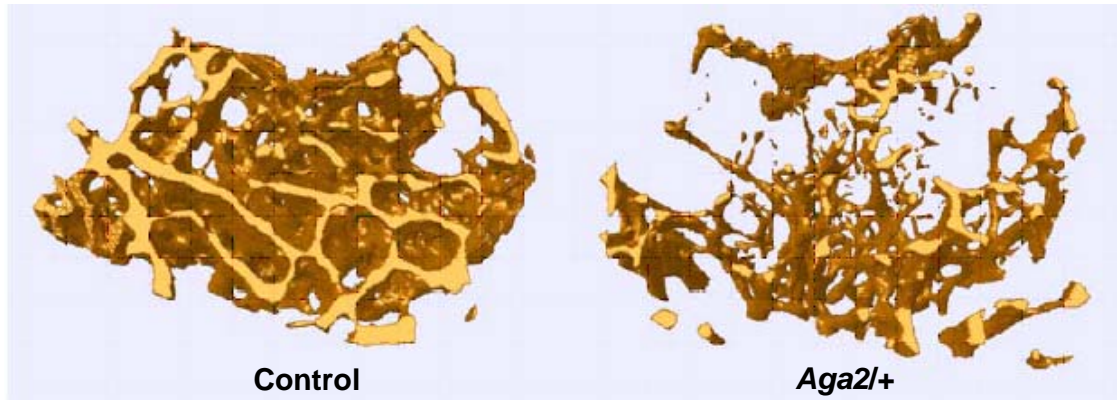
(Fig. S10) Confirmation of reduced trabeculae in *Aga2*/+ mice. Micro CT showed reduced femoral trabeculae in 12-week-old male *Aga2* mice. Trabecular number and thickness were reduced, while trabecular spacing was increased. vBMD and vBMC were both decreased in *Aga2*. Preliminary CT images and analysis performed by Dr. Phil Salmon (Skyscan Inc.).

Figure S11. Increased osteoblasts in *Aga2*
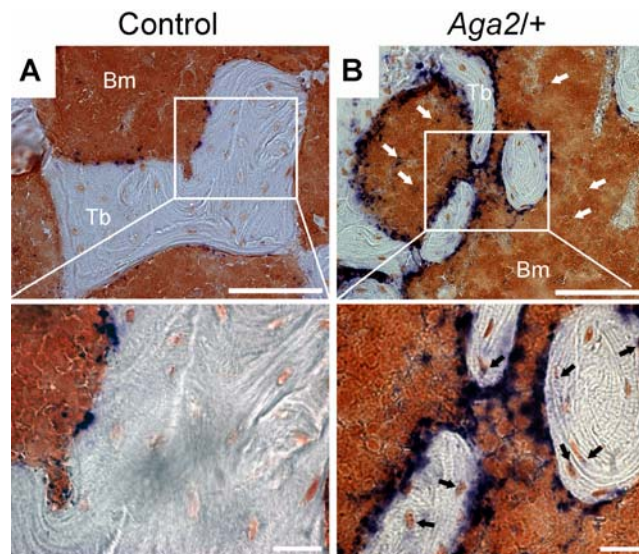
(Fig. S11) Bone micrographs depicting increased OBs in 12-week-old male mice. In *A*, demonstration of endogenous ALP activity (violet) within metaphysial secondary trabeculae (Tb) in control samples. In *B*, *Aga2* samples show elevated numbers of ALP-positive cells at the trabecular surface and periphery, and also deep within the bone marrow (Bm; white arrows). Residual ALP activity was also detected among cells embedded anew within trabecular bone in *Aga2* samples (*B*; expanded box, black arrows). *Bars*, 100 μm for main, and 20 μm for expanded boxes in *A* and *B* combined. Decalcified frozen sections were counter stained with neutral red solution.

Figure S12. Altered epiphysial plate in *Aga2*
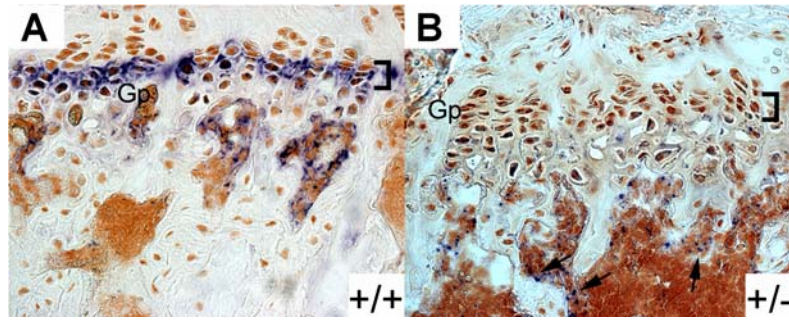
(Fig. S12) Anomalies in ALP expression among pre/hypertrophic *Aga2* chondrocytes. In *A*, frozen decalcified sections of wild-type tibial growth plate (Gp) depict normal expression of ALP within pre/hypertrophic chondrocytes (bracket) in 13-week-old female mice. In *B*, age-matched *Aga2* female mice depict reduced ALP expression within the hypertrophic zone, while OBs were clearly stained at the osteogenic zone (black arrows). Of note, other areas of normal ALP expression in hypertrophic chondrocytes were also detected in *Aga2* samples.

Figure S13. *Aga2* response to bisphosphonate treatment
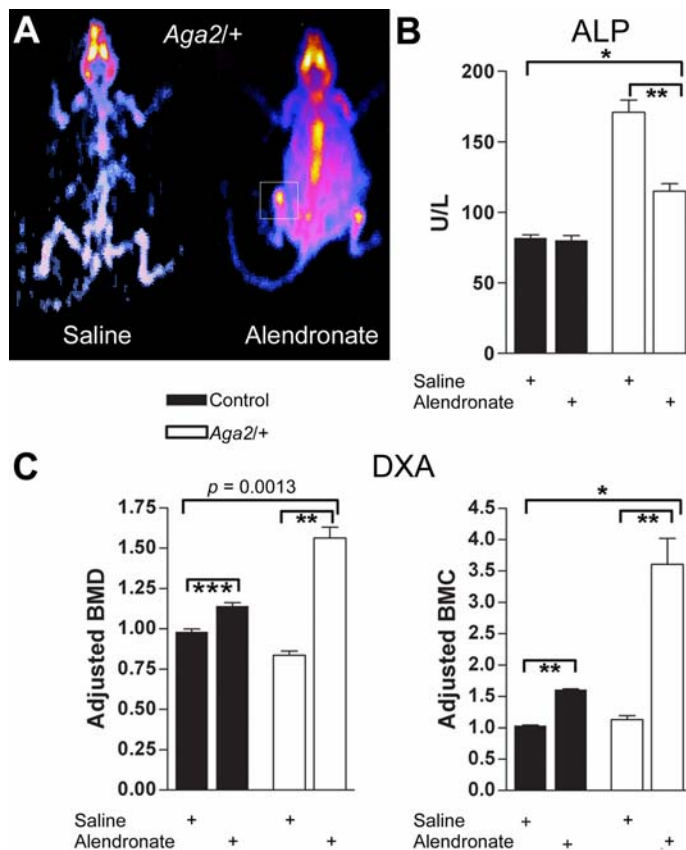
(Fig. S13) Anabolic effects of alendronate (ALD) on 21-week-old male mice. In *A*, representative DXA scans of *Aga2*/+ mice. The boxed region depicts the large increase in bone parameters potentially affecting length and growth plate morphology. In *B*, serum ALP measurements at 21 weeks. In *C*, quantification of the positive bone effects of ALD treatment. Error bars represent mean ± SEM, where $n = 8$ animals (samples) per treatment group. *$p < 0.0001$ ANOVA, and **$p < 0.001$ and ***$p < 0.05$ *post hoc* test. All unadjusted bone parameters depicted similar trends.

Figure S14. Silver stain analysis
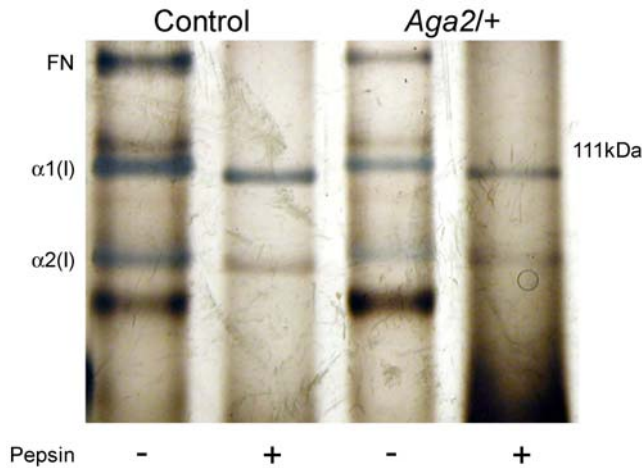
(Fig. S14) Gel analysis of secreted type I collagen from dermal fibroblasts. Both control and *Aga2/+* cells secrete normal ratios (2:1) of α1(I):α2(I) chains into the media. Type I collagen chains appeared unmodified in *Aga2*. Samples were run on a 5 % SDS-PAGE gel under reducing conditions. Samples were pepsin digested accordingly. Fibronectin (FN)

Figure S15. Anti-sera specificity
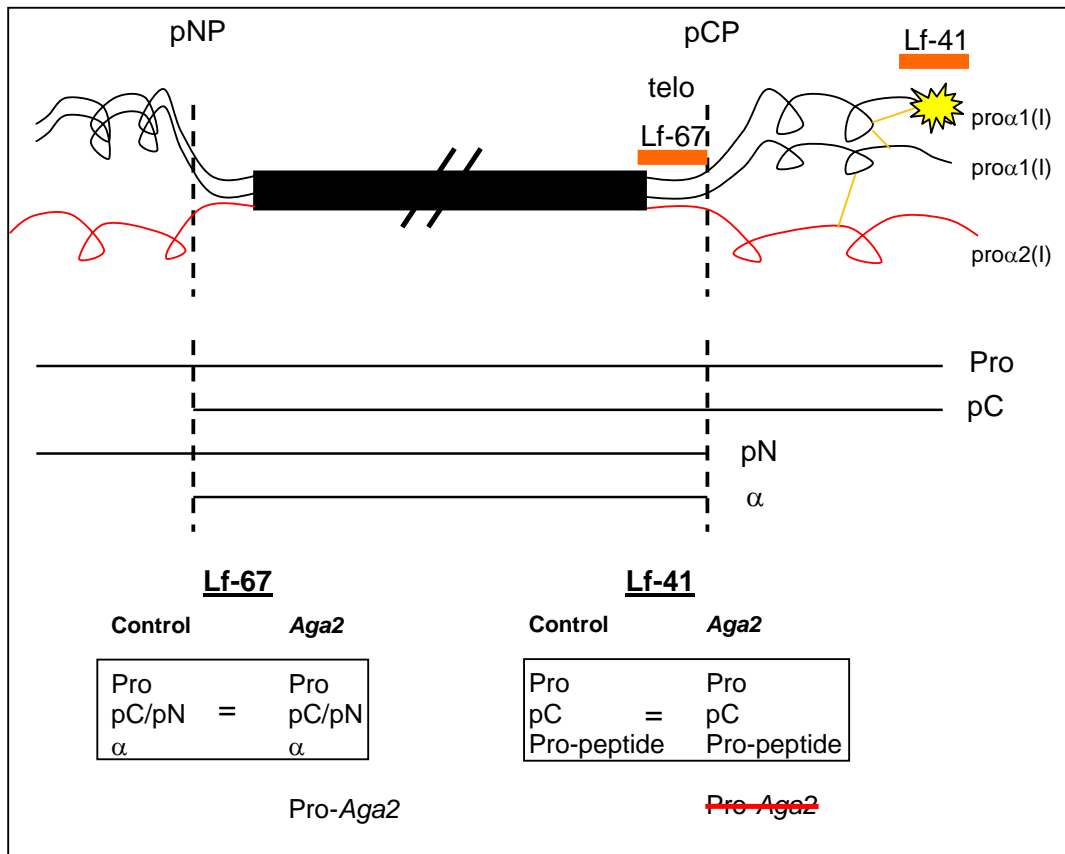
(Fig. S15) LF-41 and LF-67 specificity. Various procollagen I isoforms are displayed upon proteinase processing of the full length procollagen I molecule (Pro). LF-41 can not discriminate the *Aga2* frameshifted product. pNP (N-proteinase), pCP (C-proteinase), telo (telopeptide region)

Figure S16. Pro-α1(I) retention and ER localization
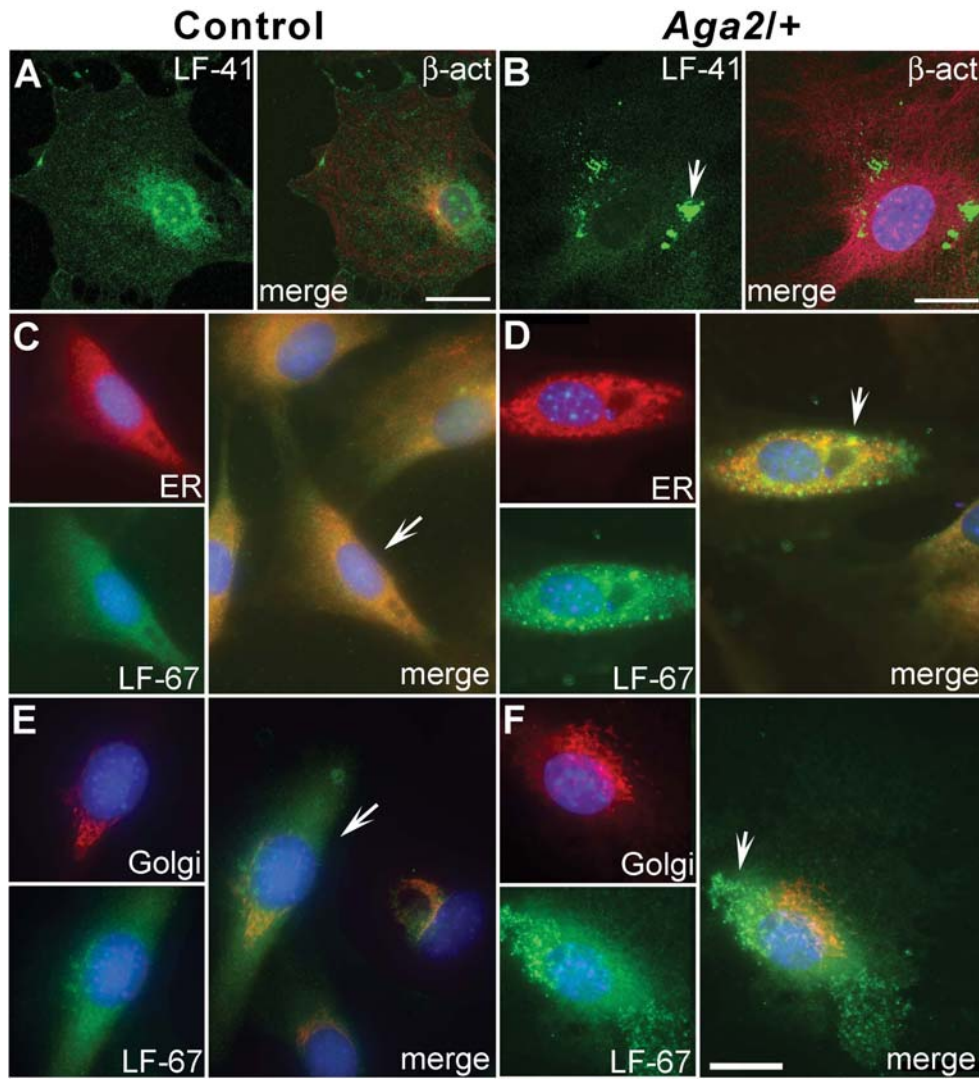
(Fig. S16) Assessment of pro-α1(I) *de novo* chain synthesis and trafficking using dual immunofluorescence (IF) microscopy in primary dermal fibroblasts. *A*, control fibroblasts depict dynamic intracellular trafficking of procollagens and chain isoforms using antiserum LF-41 which recognized the terminal C-propeptide of pro-α1(I). LF-41 recognizes the wild-type-overlapping segment within the *Aga2* frameshifted region (Fig. 12 and S14). In contrast, *Aga2* fibroblasts retained (wild type) procollagen molecules and its isoforms despite detection with LF-41 (*B*, arrow). Additionally, the degree of surface staining in both wild-type and *Aga2* cells was limited regardless of the genotype given that the LF-41 antiserum could not discriminate mature type I collagen in the ECM. The combined panels *D* and *F* (arrows) clearly show pro-α1(I) chain retention within the ER, not in the *cis*-Golgi respectively, when compared to controls (*C* and *E*, respectively). The type I telo-propeptide antiserum LF-67 was utilized due to its ability to discriminate between both wild-type and mutated chains, and other monomers. Of note, wild-type cells exhibited greater surface staining compared to *Aga2* cells, given that the LF-67 antiserum was able to differentiate between the triple helix domain isoform which was predominantly expressed in the ECM in wild-type samples. Also, vesicular structures reasoned to be proteasomes can bee seen in *Aga2*/+ cells (merge, green dots). Roughly 3.1 ± 0.7 % of control versus 20.8 ± 2.0 % of total *Aga2* fibroblasts ($p < 0.0001$ Student t test) acquired aberrant procollagen molecules. And a larger proportion of analyzed cells featured the above relationship (data not shown). Protein disulphide isomerase (PDI) and golgi phosphoprotein 4 (GOLPH4) antibodies (Abcam, UK) were used for ER and *cis*-Golgi apparatus detection, respectively. Alexa Fluor 488 (green) and 546 (red) conjugated secondary antibodies were applied accordingly (Invitrogen, Germany). Nuclei were counterstained with DAPI. Cytoskeleton was counterstained using a ß-actin antibody (Abcam). *Bar*, 25 mm

Figure S17. *In vitro* growth curve analysis
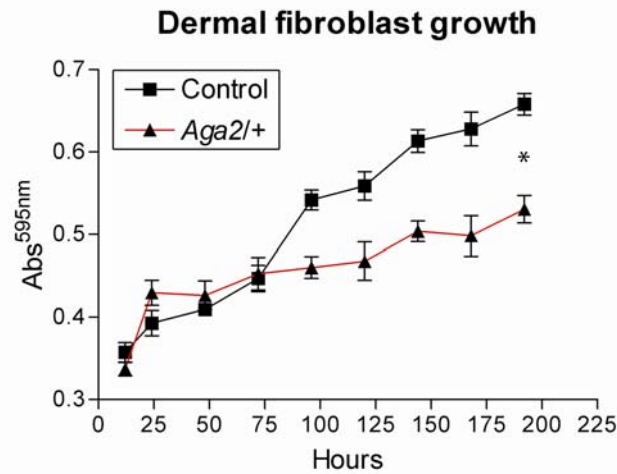
(Fig. S17) *Aga2* dermal fibroblast growth. Primary fibroblasts derived from *Aga2*/+ dermis revealed limited cell saturation and viability compared to control samples (*$p < 0.001$ Student t test). Total cell number was quantified upon the crystal violet nuclei staining method. Plots represents mean ± SEM as error bars ($n = 4$).

Figure S18. *In situ* TUNEL detection in femoral periosteum
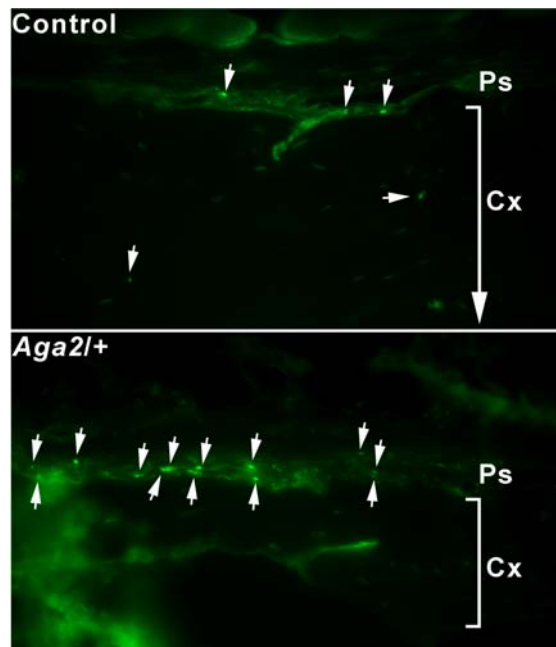
(Fig. S18) DNA fragmentation in 12-week-old male mice. *Aga2*/+ periosteum contained increased numbers of TUNEL-positive OBs when compared to control, corroborating the caspase-3 results. No differences were observed within cortical bones. TUNEL was detected using a fluorescein kit according to the manufacture's protocol. Periosteum (Ps), cortex (Cx)

Figure S19. Mouse ECG trace
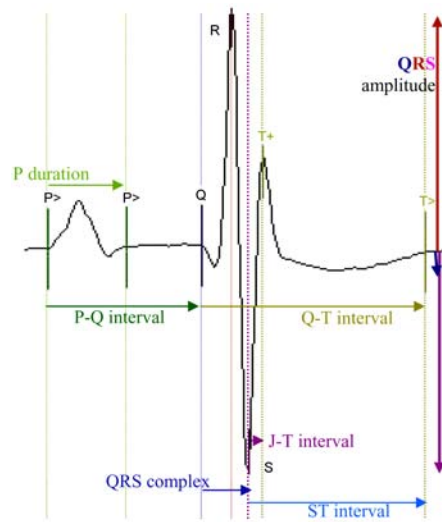
(Fig. S19) Example of electrocardiogram trace with analyzed parameters.

Figure S20. Synovial joint
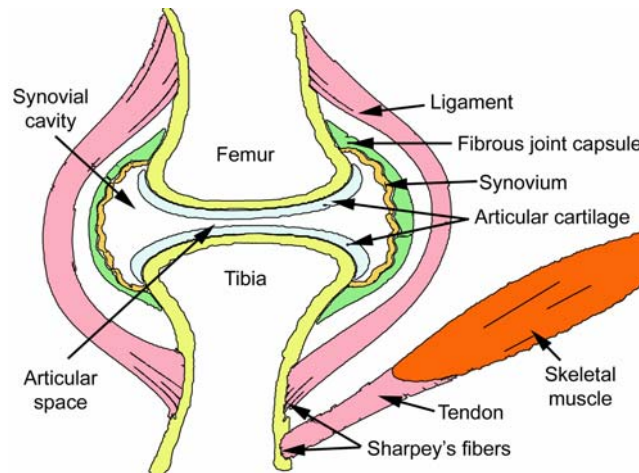
(Fig. S20) Simplified scheme of the connective tissues of the synovial joint. Patella not shown.

Figure S21. *Ali34* mapping strategy
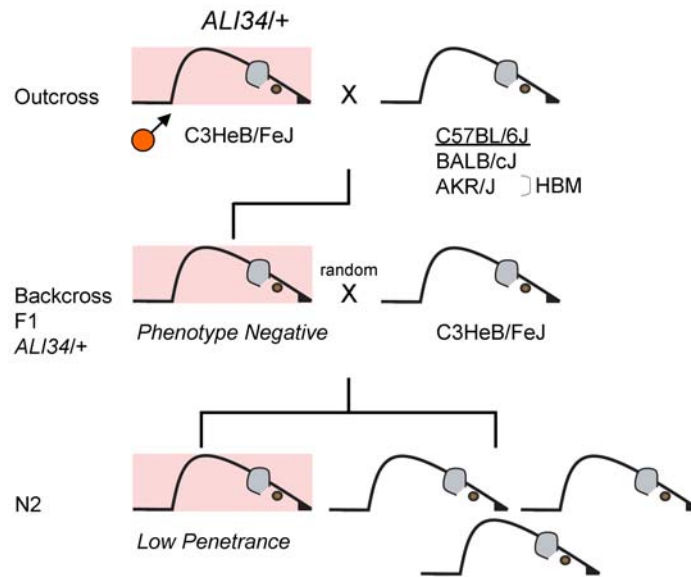
(Fig. S21) Linkage analysis using an outcross-backcross (F_1 X P) strategy due to severe modifier effects of the outcrossed strains. Three outcross strains were tested, including a known high bone mass (HBM) strain. P (parental), orange (ENU-induced *Ali34* mutant)

Figure S22. SNP analysis
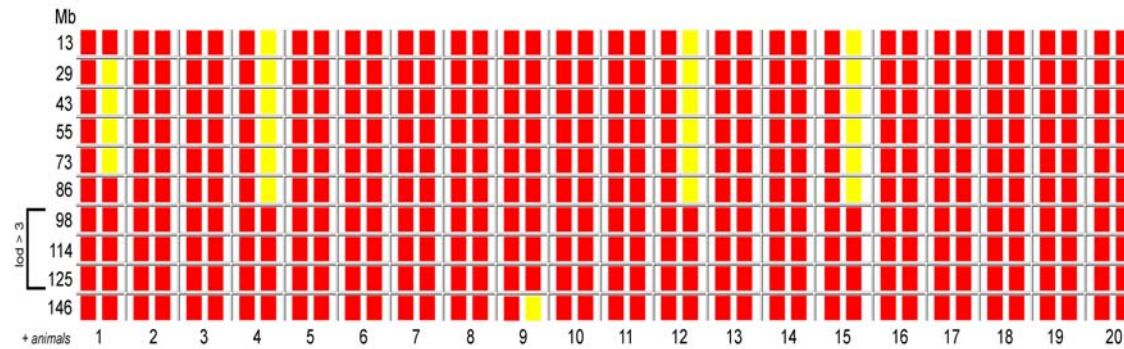
(Fig. S22) Whole-genome SNP linkage analysis was performed on phenotype-positive N_2 offspring. Linkage was observed at the mid-to-distal portion of mouse chromosome 6. Red box (C3HeB/FeJ), yellow box (C57BL/6J)

Table S1. Osteoblast and osteoclast regulation

A.   BMU (Bone multicellular unit) remodeling sequence

Phase	Stimulatory Factors	Inhibitory Factors
1. Origination	PTH, IGF, IL-1, IL-6, PGE2, Vit D, TNF	estrogen
2. Osteoclast recruitment	M-CSF, RANKL, TNF	osteoprotegerin
3. Resorption	RANKL, integrins, interleukins, acidosis, Vit A	estrogen, calcitonin, interferon, TGF
4. Osteoblast recruitment	TGFß, BMPs, IGF, FGFs, PDGFs, CSF, PTH, vit D, Cbfa1, LIF	leptin
5. Osteoid formation	TGFß, BMPs, IGF	FGFs, PDGFs, glucocorticoids
6. Mineralization	calcium, phosphate	pyrophosphate
7. Mineral maturation	Other ions	
8. Quiescence		

B.   Factors regulating RANK ligand (RANKL) and osteoprotegerin (OPG) expression

RANKL inducers	RANKL inhibitors	OPG inducers	OPG inhibitors
Vit D, PTH, TNFα, glucocorticoids, IL-1, IL-11, T4/T3, PGE2, LPS, FGF-2, histamine, IGF-1, low gravity	estrogen, TGFβ, Vit K2	TGFβ	Vit D, PTH, glucocorticoids, PGE2, IL-11, low gravity

C.   Aging effects upon bone

1.   Decreased sex steroid stimulation

2.   Men have greater periosteal apposition than women, therefore less net bone loss

3.   Increased adipogenesis with decreased osteoblastogenesis

4.   Increased cytokine stimulation

5.   Increased apoptosis of OBs

6.   Decreased OC apoptosis

7.   Altered responsiveness to growth factors and hormones

D.   Factors influencing bone remodeling and/or healing

1.   Systemic: age, hormones, functional activity, nerve function, nutrition, drugs (NSAIDs)
2.   Local: degree of trauma, extent of bone loss, vascular injury, type of bone fractured, degree of immobilization, infection, local pathological condition

E.   Role of growth factors/cytokines in fracture repair

Growth Factor	Source	Function
TGFß	Platelets, bone extracellular matrix, cartilage matrix	Stimulates undifferentiated mesenchyme cell proliferation
BMP	Osteoprogenitor cells, OBs, bone extracellular matrix	Promotes differentiation of mesenchyme cells into chondrocytes and OBs and osteoprogenitors into OBs, influences skeletal pattern formation
Fibroblast growth factors (FGF)	Macrophages, mesenchyme cells, chondrocytes, OBs	Mitogenic for mesenchyme cells, chondrocytes, and OBs
Insulin-like growth factors (IGF)	Bone matrix, OBs, chondrocytes	Promotes proliferation and differentiation of osteoprogenitor cells
Platelet-derived growth factor (PDGF)	Platelets, OBs	Mitogen for mesenchymal cells and OBs; macrophage chemotaxis

F.   Prospects for regenerative biology of bone

1.   Biological: bone grafting, stem cell transplant, osteoinductive matrices (ceramics, collagen scaffold, biodegradable polymers), growth factors (BMP, FGF, TGF, IGF)
2.   Regional gene therapy: viral vectors (*in vivo, ex vivo*), DNA injection into fracture site with gene activated matrix

(Table S3) Source: Seeman E. 2003 (284). PGE2 (prostaglandin E2), M-CSF (macrophage colony-stimulating factor), CTSK (cathepsin K), leukemia inhibitory factor (LIF), lipopolysaccharide (LPS), non-steroidal anti-inflammatory drug (NSAID)

Table S2. Major ECM proteins of bone

Classification	Protein
Collagens	Types I, III, V, XI
Proteoglycans	Versican, syndecan, CS-decorin, CS-biglycan, KS-osteoadherin, lumican
Phosphoproteins	Bone sialoprotein (BSP; integrin binding sialoprotein), osteopontin (OPN or Spp1), osteonectin (SPARC), BAG-75
Gamma carboxy glutamate containing proteins	Osteocalcin, matrix gla protein
Serum proteins	Albumin, fetuin, IgE, IgG
Others	Thrombospondin-1/2, fibromodulin, proteolipids, TGFβ, IL-2

(Table S2) CS (chondroitin sulphate), KS (keratan sulphate), BAG (bone acidic glycoprotein)

Table S3. Examples of the major collagens

Type	Molecule Composition	Structural Features	Tissue
Fibrillar Collagens			
I	$[\alpha1(I)]_2[\alpha2(I)]$	300-nm-long fibrils	Skin, tendon, bone, ligaments, dentin, interstitial tissues
II	$[\alpha1(II)]_3$	300-nm-long fibrils	Cartilage (remnant), vitreous humor
III	$[\alpha1(III)]_3$	300-nm-long fibrils; often with type I	Skin, muscle, blood vessels
V	$[\alpha1(V)]_3$	390-nm-long fibrils with globular N-terminal domain; often with type I	Similar to type I; also cell cultures, fetal tissues
XI	$[\alpha1(XI)][\alpha2(XI)][\alpha3(XI)]$	Homologous to type V	Cartilage, vitreous body
Fibril-Associated Collagens			
VI	$[\alpha1(VI)][\alpha_2(VI)]$	Lateral association with type I; periodic globular domains	Most interstitial tissues
IX (FACIT)	$[\alpha1(IX)][\alpha2(IX)][\alpha3(IX)]$	Lateral association with type II; N-terminal globular domain; bound glycosaminoglycan	Cartilage, vitreous humor
Sheet-Forming Collagens			
IV	$[\alpha1(IV)]_2[\alpha2(IV)]$	Two-dimensional network	All basal laminaes
Transmembrane Collagens			
XIII	$[\alpha1(XIII)]_3$	Transmembrane NC4 domain	Epidermis, hair follicle, lung, chondrocytes, liver

(Table S3) Source: Pollard et al. 2002 (285)
Of note: Currently there are 28 known collagen types within the family of proteins, and each collagen type interacts with other collagens.

Table S4. *Mus musculus* col1a1 protein/transcript features

Key	From	To	Length	Description
SIGNAL	1	22	22	
PROPEP	23	151	129	N-terminal propeptide
CHAIN	152	1207	1056	Collagen alpha-1(I) chain
PROPEP	1208	1453	246	C-terminal propeptide
DOMAIN	29	87	59	VWFC
REGION	152	167	16	Non-helical region (N-terminal)
REGION	168	1181	1014	Triple-helical region
REGION	1182	1207	26	Non-helical region (C-terminal)
MOTIF	734	736	3	Cell attachment site (Potential)
MOTIF	1082	1084	3	Cell attachment site (Potential)
MOD_RES	152	152	1	Pyrrolidone carboxylic acid
MOD_RES	160	160	1	Allysine (By similarity)
MOD_RES	254	254	1	5-hydroxylysine (By similarity)
MOD_RES	1153	1153	1	3-hydroxyproline (By similarity)
CARBOHYD	56	56	1	N-linked (GlcNAc) (Potential)
CARBOHYD	254	254	1	O-linked (Gal) (By similarity)
CARBOHYD	1354	1354	1	N-linked (GlcNAc) (By similarity)

MOD_RES: post-translational modification of a residue
CARBOHYD: glycosylation site
VWFC: von Willebrand Factor C

(Table S4) Assembled from UniProtKB/Swiss-Prot (Accession Nr. P11087; http://expasy.org/uniprot). 1,453 amino acids in the unprocessed collagen α-1(I) chain precursor.

Table S5. *Aga2* embryonic lethality

Mating *Aga2*/+ X *Aga2*/+	Breeding Pairs	Total Embryos	Genotype			χ^2 p; df = 2
Embryonic Stage			wt	het	hom	
E8-8.5	4	30	5	19	6	1.48; NS
E9.5-10	4	24	6	16	2	3.10; NS
E11-13	4	20	4	16	0	7.12; 0.03

Not significant (NS)

Table S6. Dysmorphology

Age[1]	Feature		Control (A) Male	Control (A) Female	Aga2/+ (B) Male	Aga2/+ (B) Female	Fisher's test or pairwise A-B Male	Fisher's test or pairwise A-B Female	ANOVA Genotype	ANOVA Sex	ANOVA Interaction
9wks			*n* = 15		*n* = 15						
	Abnormal gait		0	0	15	15	***	***	-	-	-
	Abnormal body[2]		0	0	15	15	***	***	-	-	-
	Pigmented skin		0	1	1	3	NS	NS	-	-	-
	Absent/altered incisors		0	0	0	3	NS	NS	-	-	-
	Fractured femur[3]		0	0	2	0	NS	NS	-	-	-
	Fractured tibia		0	0	13	13	***	***	-	-	-
	Deformed fibula		0	0	7	6	**	*	-	-	-
	Fractured humerus		0	0	6	9	*	***	-	-	-
	Fractured ulna		0	0	10	9	***	***	-	-	-
	Fractured radius		0	0	5	7	*	**	-	-	-
	Kyphosis/scoliosis		0	0	15	15	***	***	-	-	-
	Pelvis[4]		0	0	15	15	***	***	-	-	-
16wks			*n* = 10		*n* = 10						
	Body mass [g]		32.14 ± 0.33	32.73 ± 0.96	21.28 ± 0.65	19.89 ± 0.54	***	***	***	NS	NS
	Body length[5] [cm]		9.95 ± 0.05	10.05 ± 0.08	8.95 ± 0.09	8.90 ± 0.07	***	***	***	NS	NS
	Subcutaneous fat span [mm]		4.79 ± 0.12	5.41 ± 0.31	2.71 ± 0.12	3.03 ± 0.30	***	***	***	NS	NS
	Vertebrae height[6] [mm]		3.39 ± 0.05	3.51 ± 0.05	2.94 ± 0.07	3.09 ± 0.07	***	***	***	NS	NS
	pDXA	BMD [mg/cm^2]	57 ± 1.0	60 ± 2.0	42 ± 1.0	42 ± 1.0	***	***	***	NS	NS
		BMC [mg]	928 ± 17	945 ± 46	307 ± 20	310 ± 13	***	***	***	NS	NS
		Fat content [units x 100/g]	30.75 ± 1.4	34.17 ± 2.8	0.63 ± 0.6	0.84 ± 0.8	***	***	***	NS	NS
		Lean content [units x 100/g]	58.19 ± 1.3	53.48 ± 2.9	93.90 ± 1.4	91.89 ± 1.7	***	***	***	NS	NS
21wks	Femur length[7] [mm]		15.25 ± 0.17	15.31 ± 0.09	14.61 ± 0.12	14.77 ± 0.15	**	**	***	NS	NS
	Mediolateral shaft diameter [mm]		1.80 ± 0.03	1.75 ± 0.04	1.40 ± 0.03	1.49 ± 0.03	***	***	***	NS	**

[1] Data collected from the German Mouse Clinic dysmorphology primary screen; direction of breeding was paternal
[2] Slender
[3] Healed fractures
[4] Ischium and pubis region deteriorated

[5] Nostril to base of tail
[6] Third lumbar (compression)
[7] Femur length was measured as the *ex vivo* proximal (tip of greater trochanter) to distal (intercondylar fossa) distance. Measurements were made using calipers

p values based on Fisher's exact test for the contingency table values, and ANOVA for the continuous variables. Data represents mean ± SEM. $*p < 0.05$, $**p < 0.01$, $***p < 0.001$

Not significant (NS), dual-energy X-ray absorptiometry (DXA), BMD (bone mineral density, w/o head), BMC (bone mineral content)

Table S7. Histomorphometry

Indices	Structure	Control ($n = 6$)	*Aga2*/+ ($n = 6$)	Significance
BS/TA (%)	Df (M)	34.3 ± 4.2	15.9 ± 2.3	0.018
Cx.Wi (µm)	F (Md)	183.4 ± 5.1	107.0 ± 8.0	0.0013
Tb.N (/mm)	Df (M)	4.6 ± 0.2	3.2 ± 0.2	<0.0001
Tb.Th (µm)	Df (M)	80.0 ± 7.8	38.5 ± 4.7	<0.0001
Tb.Sp (µm)	Df (M)	145.4 ± 10.0	281.5 ± 27.5	0.0001

(Table S7) Histomorphometric analysis of femora from 12-week-old male mice. Values represent mean ± SEM, where averaged measurements using four nonconsecutive sections from six animals ($n = 6$) were investigated. *p* values were derived from the Student t test. Bone surface area (BS/TA), cortical thickness (Cx.Wi), trabecular number (Tb.N), trabecular thickness (Tb.Th), trabecular separation (Tb.Sp), distal femur (Df), femur (F), metaphysis (M), mid-diaphysis (Md)

Table S8. Primer description

Gene	Sequence	Length [bp]	Annealing temperature [°C]
Twist1	For: 5'-CGGACAAGCTGAGCAAGATT-3' Rev: 5'-ACAATGACATCTAGGTCTCCGG-3'	241	60
Osx	For: 5'-CTACCCAGCTCCCTTCTCAA-3' Rev: 5'-CTTGTACCACGAGCCATAGG-3'	213	60
Col1a1	For: 5'-CCGGAAGAATACGTATCACCA-3' Rev: 5'-GAAGCAAAGTTTCCTCCAAGG-3'	194	59
ALP2	For: 5'-TTGTGCCAGAGAAAGAGAGAGAC-3' Rev: 5'-TTGGTGTTATATGTCTTGGAGAGG-3'	259	60
BSP	For: 5'-ACCTGTGCACATGCATTTTT-3' Rev: 5'-CAGTGACTGTGCCCTCCTTAG-3'	227	59
Oc	For: 5'-GACCTCACAGATGCCAAGC-3' Rev: 5'-GACTGAGGCTCCAAGGTAGC-3'	111	59
CD44	For: 5'-AAAATCGACCCAAGACTGTCA-3' Rev: 5'-GGGGGTCTCTGAAAAATCAA-3'	214	59
BiP	For: 5'-CTGGGTACATTTGATCTGACTGG-3' Rev: 5'-GCATCCTGGTGGCTTTCCAGCCATTC-3'	398	60
Actb	For: 5'-GCCACCAGTTCGCCAT-3' Rev: 5'-CATCACACCCTGGTGCCTA-3'	146	59

(Table S8) Twist1 (homolog 1 of drosophila), Osx (osterix), col1a1 (procollagen type I, alpha 1), ALP2 (alkaline phosphatase 2), BSP (bone sialoprotein II or integrin binding sialoprotein), Oc (osteocalcin or bone gamma carboxyglutamate protein 1), CD44 (hyaluronate receptor), BiP (binding protein precursor or Grp78), Actb (beta-actin)

6.   References

1.   Karsenty G (2003) *Nature* **423,** 316-318.
2.   Cohen MM, Jr. (2006) *Am J Med Genet A* **140,** 2646-2706.
3.   Grueneberg H (1963) *The pathology of development: A study of inherited skeletal disorders in animals* (Blackwell Scientific New York).
4.   Herrmann BG, Labeit S, Poustka A, King TR, & Lehrach H (1990) *Nature* **343,** 617-622.
5.   Herrmann BG & Kispert A (1994) *Trends Genet* **10,** 280-286.
6.   Showell C, Binder O, & Conlon FL (2004) *Dev Dyn* **229,** 201-218.
7.   Tada M & Smith JC (2001) *Dev Growth Differ* **43,** 1-11.
8.   White PH & Chapman DL (2005) *Genesis* **42,** 193-202.
9.   Hofmann M, Schuster-Gossler K, Watabe-Rudolph M, Aulehla A, Herrmann BG, & Gossler A (2004) *Genes Dev* **18,** 2712-2717.
10.   Ralston SH & de Crombrugghe B (2006) *Genes Dev* **20,** 2492-2506.
11.   Mariani FV & Martin GR (2003) *Nature* **423,** 319-325.
12.   Karsenty G & Wagner EF (2002) *Dev Cell* **2,** 389-406.
13.   Horton WA (2003) *Lancet* **362,** 560-569.
14.   Hartmann C (2006) *Trends Cell Biol* **16,** 151-158.
15.   Goldring MB, Tsuchimochi K, & Ijiri K (2006) *J Cell Biochem* **97,** 33-44.
16.   Vignery A (2005) *J Exp Med* **202,** 337-340.
17.   Stein GS, Lian JB, Stein JL, Van Wijnen AJ, & Montecino M (1996) *Physiol Rev* **76,** 593-629.
18.   Huang W, Yang S, Shao J, & Li YP (2007) *Front Biosci* **12,** 3068-3092.
19.   Patton JT & Kaufman MH (1995) *J Anat* **186 (Pt 1),** 175-185.
20.   Wolff J (1892) *Das Gesetz der Transformation der Knochen.* (A. Hirchwild, Berlin).
21.   Boskey AL, Wright TM, & Blank RD (1999) *J Bone Miner Res* **14,** 330-335.
22.   Boyce BF & Xing L (2006) *Nat Med* **12,** 1356-1358.
23.   Lee SH, Rho J, Jeong D, Sul JY, Kim T, Kim N, Kang JS, Miyamoto T, Suda T, Lee SK*, et al.* (2006) *Nat Med* **12,** 1403-1409.
24.   Carter PH & Schipani E (2006) *Endocr Metab Immune Disord Drug Targets* **6,** 59-76.
25.   Zaidi M, Moonga BS, & Abe E (2002) *J Clin Invest* **110,** 1769-1771.
26.   Prockop DJ & Kivirikko KI (1995) *Annu Rev Biochem* **64,** 403-434.
27.   Myllyharju J & Kivirikko KI (2001) *Ann Med* **33,** 7-21.
28.   Myllyharju J & Kivirikko KI (2004) *Trends Genet* **20,** 33-43.
29.   Di Lullo GA, Sweeney SM, Korkko J, Ala-Kokko L, & San Antonio JD (2002) *J Biol Chem* **277,** 4223-4231.
30.   Kielty CM & Grant ME (2002) in *Connective Tissue and its Heritable Disorders*, eds. Royce P & Steinmann B (Wiley-Liss Inc, New York), pp. 159-221.
31.   Gelse K, Poschl E, & Aigner T (2003) *Adv Drug Deliv Rev* **55,** 1531-1546.
32.   Boot-Handford RP & Tuckwell DS (2003) *Bioessays* **25,** 142-151.
33.   Canty EG & Kadler KE (2005) *J Cell Sci* **118,** 1341-1353.
34.   Donzelli E, Salvade A, Mimo P, Vigano M, Morrone M, Papagna R, Carini F, Zaopo A, Miloso M, Baldoni M*, et al.* (2007) *Arch Oral Biol* **52,** 64-73.
35.   Khoshnoodi J, Cartailler JP, Alvares K, Veis A, & Hudson BG (2006) *J Biol Chem* **281,** 38117-38121.
36.   Lee JE, Kang CS, Guan XY, Kim BT, Kim SH, Lee YM, Moon WS, & Kim DK (2007) *Biochem Biophys Res Commun* **352,** 244-250.

37. Veit G, Kobbe B, Keene DR, Paulsson M, Koch M, & Wagener R (2006) *J Biol Chem* **281,** 3494-3504.
38. von der Mark K (1999) in *Dynamics of bone and cartilage metabolism*, eds. Seibel M, Robins S, & Bilezikian J (Academic Press, London), pp. 3-29.
39. Alford AI & Hankenson KD (2006) *Bone* **38,** 749-757.
40. Filla MS, Woods A, Kaufman PL, & Peters DM (2006) *Invest Ophthalmol Vis Sci* **47,** 1956-1967.
41. Fuja TJ, Ostrem EM, Probst-Fuja MN, & Titze IR (2006) *Matrix Biol* **25,** 240-251.
42. Kirsch T (2006) *Curr Opin Rheumatol* **18,** 174-180.
43. Feng H, Danfelter M, Stromqvist B, & Heinegard D (2006) *J Bone Joint Surg Am* **88 Suppl 2,** 25-29.
44. Ishikawa J, Kario K, Matsui Y, Shibasaki S, Morinari M, Kaneda R, Hoshide S, Eguchi K, Hojo Y, & Shimada K (2005) *Hypertens Res* **28,** 995-1001.
45. Lynch MP, Stein JL, Stein GS, & Lian JB (1995) *Exp Cell Res* **216,** 35-45.
46. Serini G, Valdembri D, & Bussolino F (2006) *Exp Cell Res* **312,** 651-658.
47. Oswald J, Steudel C, Salchert K, Joergensen B, Thiede C, Ehninger G, Werner C, & Bornhauser M (2006) *Stem Cells* **24,** 494-500.
48. Sengupta P, Xu Y, Wang L, Widom R, & Smith BD (2005) *J Biol Chem* **280,** 21004-21014.
49. Grzesiak JJ, Smith KC, Chalberg C, Burton DW, Deftos LJ, & Bouvet M (2005) *Int J Gastrointest Cancer* **36,** 131-146.
50. Grzesik WJ, Frazier CR, Shapiro JR, Sponseller PD, Robey PG, & Fedarko NS (2002) *J Biol Chem* **277,** 43638-43647.
51. Koenig A, Mueller C, Hasel C, Adler G, & Menke A (2006) *Cancer Res* **66,** 4662-4671.
52. Ju H & Dixon IM (1996) *Can J Cardiol* **12,** 1259-1267.
53. Rossert J & Crombrugghe B (1999) in *Dynamics of bone and cartilage metabolism*, eds. Seibel M, Robins S, & Bilezikian J (Academic Press, London), pp. 127-142.
54. Dunsmore SE & Rannels DE (1996) *Am J Physiol* **270,** L3-27.
55. Hance AJ, Bradley K, & Crystal RG (1976) *J Clin Invest* **57,** 102-111.
56. Bou-Gharios G, Garrett LA, Rossert J, Niederreither K, Eberspaecher H, Smith C, Black C, & Crombrugghe B (1996) *J Cell Biol* **134,** 1333-1344.
57. Chichester CO, Fernandez M, & Minguell JJ (1993) *Cell Adhes Commun* **1,** 93-99.
58. Thomas DP, Zimmerman SD, Hansen TR, Martin DT, & McCormick RJ (2000) *J Appl Physiol* **89,** 1462-1468.
59. Weis SM, Emery JL, Becker KD, McBride DJ, Jr., Omens JH, & McCulloch AD (2000) *Circ Res* **87,** 663-669.
60. Pyagay P, Heroult M, Wang Q, Lehnert W, Belden J, Liaw L, Friesel RE, & Lindner V (2005) *Circ Res* **96,** 261-268.
61. Chan D, Lamande SR, McQuillan DJ, & Bateman JF (1997) *J Biochem Biophys Methods* **36,** 11-29.
62. Lamande SR & Bateman JF (1999) *Semin Cell Dev Biol* **10,** 455-464.
63. Bulleid NJ, Dalley JA, & Lees JF (1997) *Embo J* **16,** 6694-6701.
64. Kramer RZ, Bella J, Brodsky B, & Berman HM (2001) *J Mol Biol* **311,** 131-147.
65. Bruckner P & Prockop DJ (1981) *Anal Biochem* **110,** 360-368.
66. Oganesian A, Au S, Horst JA, Holzhausen LC, Macy AJ, Pace JM, & Bornstein P (2006) *J Biol Chem* **281,** 38507-38518.
67. Dodig M, Kronenberg MS, Bedalov A, Kream BE, Gronowicz G, Clark SH, Mack K, Liu YH, Maxon R, Pan ZZ*, et al.* (1996) *J Biol Chem* **271,** 16422-16429.
68. Ghosh AK (2002) *Exp Biol Med (Maywood)* **227,** 301-314.

69. Garcia-Giralt N, Nogues X, Enjuanes A, Puig J, Mellibovsky L, Bay-Jensen A, Carreras R, Balcells S, Diez-Perez A, & Grinberg D (2002) *J Bone Miner Res* **17,** 384-393.

70. Bank RA, Robins SP, Wijmenga C, Breslau-Siderius LJ, Bardoel AF, van der Sluijs HA, Pruijs HE, & TeKoppele JM (1999) *Proc Natl Acad Sci U S A* **96,** 1054-1058.

71. Lucero HA & Kagan HM (2006) *Cell Mol Life Sci* **63,** 2304-2316.

72. Fietzek PP, Allmann H, Rauterberg J, & Wachter E (1977) *Proc Natl Acad Sci U S A* **74,** 84-86.

73. Zhou L, Isenberg JS, Cao Z, & Roberts DD (2006) *Oncogene* **25,** 536-545.

74. Pentikainen MO, Oorni K, Lassila R, & Kovanen PT (1997) *J Biol Chem* **272,** 7633-7638.

75. Douglas T, Heinemann S, Bierbaum S, Scharnweber D, & Worch H (2006) *Biomacromolecules* **7,** 2388-2393.

76. Zhang J, Niu C, Ye L, Huang H, He X, Tong WG, Ross J, Haug J, Johnson T, Feng JQ*, et al.* (2003) *Nature* **425,** 836-841.

77. Aguila HL & Rowe DW (2005) *Immunol Rev* **208,** 7-18.

78. Xu Y, Gurusiddappa S, Rich RL, Owens RT, Keene DR, Mayne R, Hook A, & Hook M (2000) *J Biol Chem* **275,** 38981-38989.

79. Nho RS, Xia H, Diebold D, Kahm J, Kleidon J, White E, & Henke CA (2006) *J Biol Chem* **281,** 33291-33301.

80. Langford JK, Yang Y, Kieber-Emmons T, & Sanderson RD (2005) *J Biol Chem* **280,** 3467-3473.

81. Leitinger B & Hohenester E (2007) *Matrix Biol* **26,** 146-155.

82. Bornstein P (2002) *Matrix Biol* **21,** 217-226.

83. Lees JF, Tasab M, & Bulleid NJ (1997) *Embo J* **16,** 908-916.

84. Mizuno M, Fujisawa R, & Kuboki Y (2000) *FEBS Lett* **479,** 123-126.

85. Katayama K, Armendariz-Borunda J, Raghow R, Kang AH, & Seyer JM (1993) *J Biol Chem* **268,** 9941-9944.

86. Palmieri D, Poggi S, Ulivi V, Casartelli G, & Manduca P (2003) *J Biol Chem* **278,** 3639-3647.

87. Engelholm LH, List K, Netzel-Arnett S, Cukierman E, Mitola DJ, Aaronson H, Kjoller L, Larsen JK, Yamada KM, Strickland DK*, et al.* (2003) *J Cell Biol* **160,** 1009-1015.

88. Kjoller L, Engelholm LH, Hoyer-Hansen M, Dano K, Bugge TH, & Behrendt N (2004) *Exp Cell Res* **293,** 106-116.

89. Thomas EK, Nakamura M, Wienke D, Isacke CM, Pozzi A, & Liang P (2005) *J Biol Chem* **280,** 22596-22605.

90. Marini JC, Forlino A, Cabral WA, Barnes AM, San Antonio JD, Milgrom S, Hyland JC, Korkko J, Prockop DJ, De Paepe A*, et al.* (2007) *Hum Mutat* **28,** 209-221.

91. Pace JM, Chitayat D, Atkinson M, Wilcox WR, Schwarze U, & Byers PH (2002) *J Med Genet* **39,** 23-29.

92. Dalgleish R (1998) *Nucleic Acids Res* **26,** 253-255.

93. Prockop DJ, Constantinou CD, Dombrowski KE, Hojima Y, Kadler KE, Kuivaniemi H, Tromp G, & Vogel BE (1989) *Am J Med Genet* **34,** 60-67.

94. Gensure RC, Makitie O, Barclay C, Chan C, Depalma SR, Bastepe M, Abuzahra H, Couper R, Mundlos S, Sillence D*, et al.* (2005) *J Clin Invest* **115,** 1250-1257.

95. Pollitt R, McMahon R, Nunn J, Bamford R, Afifi A, Bishop N, & Dalton A (2006) *Hum Mutat* **27,** 716.

96. Cabral WA, Makareeva E, Colige A, Letocha AD, Ty JM, Yeowell HN, Pals G, Leikin S, & Marini JC (2005) *J Biol Chem* **280,** 19259-19269.

97. Sillence DO, Senn A, & Danks DM (1979) *J Med Genet* **16,** 101-116.

98. Rauch F & Glorieux FH (2004) *Lancet* **363,** 1377-1385.

99. Venturi G, Tedeschi E, Mottes M, Valli M, Camilot M, Viglio S, Antoniazzi F, & Tato L (2006) *Clin Genet* **70,** 131-139.
100. Niyibizi C, Wang S, Mi Z, & Robbins PD (2004) *Gene Ther* **11,** 408-416.
101. Byers P & Cole W (2002) in *Connective tissue and its heritable disorders: molecular, genetic and medical aspects*, eds. Royce P & Steinmann B (Wiley-Liss, New York), pp. 385–430.
102. Tsuneyoshi T, Westerhausen A, Constantinou CD, & Prockop DJ (1991) *J Biol Chem* **266,** 15608-15613.
103. Yang W, Chan VC, Kirkpatrick A, Ramshaw JA, & Brodsky B (1997) *J Biol Chem* **272,** 28837-28840.
104. Aubin I, Adams CP, Opsahl S, Septier D, Bishop CE, Auge N, Salvayre R, Negre-Salvayre A, Goldberg M, Guenet JL*, et al.* (2005) *Nat Genet* **37,** 803-805.
105. Sidden CR, Filly RA, Norton ME, & Kostiner DR (2001) *J Ultrasound Med* **20,** 699-703.
106. Ward LM, Rauch F, Travers R, Chabot G, Azouz EM, Lalic L, Roughley PJ, & Glorieux FH (2002) *Bone* **31,** 12-18.
107. Cabral WA, Chang W, Barnes AM, Weis M, Scott MA, Leikin S, Makareeva E, Kuznetsova NV, Rosenbaum KN, Tifft CJ*, et al.* (2007) *Nat Genet*.
108. Cole WG & Dalgleish R (1995) *J Med Genet* **32,** 284-289.
109. Barsh GS & Byers PH (1981) *Proc Natl Acad Sci U S A* **78,** 5142-5146.
110. Fitzgerald J, Lamande SR, & Bateman JF (1999) *J Biol Chem* **274,** 27392-27398.
111. Chessler SD & Byers PH (1993) *J Biol Chem* **268,** 18226-18233.
112. Lamande SR, Chessler SD, Golub SB, Byers PH, Chan D, Cole WG, Sillence DO, & Bateman JF (1995) *J Biol Chem* **270,** 8642-8649.
113. Forlino A, Tani C, Rossi A, Lupi A, Campari E, Gualeni B, Bianchi L, Armini A, Cetta G, Bini L*, et al.* (2007) *Proteomics* **7,** 1877-1891.
114. Yoshida H (2007) *Febs J* **274,** 630-658.
115. Leighton MP, Nundlall S, Starborg T, Meadows RS, Suleman F, Knowles L, Wagener R, Thornton DJ, Kadler KE, Boot-Handford RP*, et al.* (2007) *Hum Mol Genet* **16,** 1728-1741.
116. Schroder M (2006) *Mol Biotechnol* **34,** 279-290.
117. Pearse BR & Hebert DN (2006) *Mol Cell* **23,** 773-775.
118. Kouroku Y, Fujita E, Jimbo A, Kikuchi T, Yamagata T, Momoi MY, Kominami E, Kuida K, Sakamaki K, Yonehara S*, et al.* (2002) *Hum Mol Genet* **11,** 1505-1515.
119. Paschen W (2000) *Brain Res Bull* **53,** 409-413.
120. Mattson MP (2000) *Nat Rev Mol Cell Biol* **1,** 120-129.
121. Laybutt DR, Preston AM, Akerfeldt MC, Kench JG, Busch AK, Biankin AV, & Biden TJ (2007) *Diabetologia*.
122. Szegezdi E, Logue SE, Gorman AM, & Samali A (2006) *EMBO Rep* **7,** 880-885.
123. Breckenridge DG, Germain M, Mathai JP, Nguyen M, & Shore GC (2003) *Oncogene* **22,** 8608-8618.
124. Oyadomari S & Mori M (2004) *Cell Death Differ* **11,** 381-389.
125. Rao RV, Ellerby HM, & Bredesen DE (2004) *Cell Death Differ* **11,** 372-380.
126. Morishima N, Nakanishi K, Tsuchiya K, Shibata T, & Seiwa E (2004) *J Biol Chem* **279,** 50375-50381.
127. Rao RV, Peel A, Logvinova A, del Rio G, Hermel E, Yokota T, Goldsmith PC, Ellerby LM, Ellerby HM, & Bredesen DE (2002) *FEBS Lett* **514,** 122-128.
128. Manolagas SC (2000) *Endocr Rev* **21,** 115-137.
129. Nakagawa T & Yuan J (2000) *J Cell Biol* **150,** 887-894.

130. Van de Craen M, Vandenabeele P, Declercq W, Van den Brande I, Van Loo G, Molemans F, Schotte P, Van Criekinge W, Beyaert R, & Fiers W (1997) *FEBS Lett* **403,** 61-69.

131. Nakagawa T, Zhu H, Morishima N, Li E, Xu J, Yankner BA, & Yuan J (2000) *Nature* **403,** 98-103.

132. Shum L, Coleman CM, Hatakeyama Y, & Tuan RS (2003) *Birth Defects Res C Embryo Today* **69,** 102-122.

133. Superti-Furga A, Bonafe L, & Rimoin DL (2001) *Am J Med Genet* **106,** 282-293.

134. Kispert A & Herrmann BG (1993) *Embo J* **12,** 3211-3220.

135. Zhang Y, Proenca R, Maffei M, Barone M, Leopold L, & Friedman JM (1994) *Nature* **372,** 425-432.

136. King DP, Zhao Y, Sangoram AM, Wilsbacher LD, Tanaka M, Antoch MP, Steeves TD, Vitaterna MH, Kornhauser JM, Lowrey PL*, et al.* (1997) *Cell* **89,** 641-653.

137. Kusumi K, Sun ES, Kerrebrock AW, Bronson RT, Chi DC, Bulotsky MS, Spencer JB, Birren BW, Frankel WN, & Lander ES (1998) *Nat Genet* **19,** 274-278.

138. Sidow A, Bulotsky MS, Kerrebrock AW, Bronson RT, Daly MJ, Reeve MP, Hawkins TL, Birren BW, Jaenisch R, & Lander ES (1997) *Nature* **389,** 722-725.

139. Botstein D & Risch N (2003) *Nat Genet* **33 Suppl,** 228-237.

140. Hrabe de Angelis MH, Flaswinkel H, Fuchs H, Rathkolb B, Soewarto D, Marschall S, Heffner S, Pargent W, Wuensch K, Jung M*, et al.* (2000) *Nat Genet* **25,** 444-447.

141. Wilkie AO & Morriss-Kay GM (2001) *Nat Rev Genet* **2,** 458-468.

142. Srivastava AK, Mohan S, Wergedal JE, & Baylink DJ (2003) *Bone* **33,** 179-191.

143. Balling R (2001) *Annu Rev Genomics Hum Genet* **2,** 463-492.

144. Beier DR & Herron BJ (2004) *Genetica* **122,** 65-69.

145. Forlino A, Porter FD, Lee EJ, Westphal H, & Marini JC (1999) *J Biol Chem* **274,** 37923-37931.

146. Bernstein EF, Chen YQ, Kopp JB, Fisher L, Brown DB, Hahn PJ, Robey FA, Lakkakorpi J, & Uitto J (1996) *J Am Acad Dermatol* **34,** 209-218.

147. Shukunami C, Oshima Y, & Hiraki Y (2005) *Biochem Biophys Res Commun* **333,** 299-307.

148. Gailus-Durner V, Fuchs H, Becker L, Bolle I, Brielmeier M, Calzada-Wack J, Elvert R, Ehrhardt N, Dalke C, Franz TJ*, et al.* (2005) *Nat Methods* **2,** 403-404.

149. Rathkolb B, Tran TV, Klempt M, Hrabe de Angelis M, Wanke R, Wolf E, & Aigner B (2005) *Nephron Exp Nephrol* **100,** e143-149.

150. Klaften M & Hrabe de Angelis M (2005) *Nucleic Acids Res* **33,** W496-500.

151. Runkel F, Klaften M, Koch K, Bohnert V, Bussow H, Fuchs H, Franz T, & Hrabe de Angelis M (2006) *Mamm Genome* **17,** 1172-1182.

152. Ye S, Dhillon S, Ke X, Collins AR, & Day IN (2001) *Nucleic Acids Res* **29,** E88-88.

153. Fuchs H, Lisse T, Abe K, & Hrabe de Angelis M (2006) in *Standards of mouse model phenotyping*, eds. Hrabe de Angelis M, Chambon P, & Brown S (Wiley-VCH Verlag GmbH & Co, Weinheim), pp. 35-86.

154. Abe K, Fuchs H, Lisse T, Hans W, & Hrabe de Angelis M (2006) *Mamm Genome* **17,** 915-926.

155. Tjellesen L, Nielsen PK, & Staun M (1998) *Scand J Gastroenterol* **33,** 956-960.

156. van't Hof RJ, Macphee J, Libouban H, Helfrich MH, & Ralston SH (2004) *Endocrinology* **145,** 5068-5074.

157. Miao D & Scutt A (2002) *J Histochem Cytochem* **50,** 333-340.

158. Parfitt AM, Drezner MK, Glorieux FH, Kanis JA, Malluche H, Meunier PJ, Ott SM, & Recker RR (1987) *J Bone Miner Res* **2,** 595-610.

159. Peters DD, Marschall S, Mahabir E, Boersma A, Heinzmann U, Schmidt J, & Hrabe de Angelis M (2006) *Biol Reprod* **74,** 246-252.

160. Rodriguez N, Fend F, Jennen L, Schiemann M, Wantia N, Prazeres da Costa CU, Durr S, Heinzmann U, Wagner H, & Miethke T (2005) *J Immunol* **174,** 4836-4844.

161. Rathkolb B, Fuchs E, Kolb HJ, Renner-Muller I, Krebs O, Balling R, Hrabe de Angelis M, & Wolf E (2000) *Exp Physiol* **85,** 635-644.

162. Klempt M, Rathkolb B, Fuchs E, de Angelis MH, Wolf E, & Aigner B (2006) *Mamm Genome* **17,** 93-102.

163. Chipman SD, Sweet HO, McBride DJ, Jr., Davisson MT, Marks SC, Jr., Shuldiner AR, Wenstrup RJ, Rowe DW, & Shapiro JR (1993) *Proc Natl Acad Sci U S A* **90,** 1701-1705.

164. Nicholson DW (1999) *Cell Death Differ* **6,** 1028-1042.

165. Gerber I & ap Gwynn I (2001) *Eur Cell Mater* **2,** 10-20.

166. Westergren-Thorsson G, Onnervik PO, Fransson LA, & Malmstrom A (1991) *J Cell Physiol* **147,** 523-530.

167. Machka C, Kersten M, Zobawa M, Harder A, Horsch M, Halder T, Lottspeich F, Hrabe de Angelis M, & Beckers J (2005) *Gene Expr Patterns* **6,** 94-101.

168. Bustin SA, Benes V, Nolan T, & Pfaffl MW (2005) *J Mol Endocrinol* **34,** 597-601.

169. Pfaffl MW (2001) *Nucleic Acids Res* **29,** e45.

170. Fleige S, Walf V, Huch S, Prgomet C, Sehm J, & Pfaffl MW (2006) *Biotechnol Lett* **28,** 1601-1613.

171. Drozdz A & Weiner J (1975) *Pol Ecol Stud* **1,** 85–101.

172. Seltmann M, Horsch M, Drobyshev A, Chen Y, de Angelis MH, & Beckers J (2005) *Mamm Genome* **16,** 1-10.

173. Hegde P, Qi R, Abernathy K, Gay C, Dharap S, Gaspard R, Hughes JE, Snesrud E, Lee N, & Quackenbush J (2000) *Biotechniques* **29,** 548-550, 552-544, 556 passim.

174. Saeed AI, Sharov V, White J, Li J, Liang W, Bhagabati N, Braisted J, Klapa M, Currier T, Thiagarajan M*, et al.* (2003) *Biotechniques* **34,** 374-378.

175. Quackenbush J (2002) *Nat Genet* **32 Suppl,** 496-501.

176. Yang YH, Dudoit S, Luu P, Lin DM, Peng V, Ngai J, & Speed TP (2002) *Nucleic Acids Res* **30,** e15.

177. Tusher VG, Tibshirani R, & Chu G (2001) *Proc Natl Acad Sci U S A* **98,** 5116-5121.

178. Chapman JA (1974) *Connect Tissue Res* **2,** 137-150.

179. Forlino A, Piazza R, Tiveron C, Della Torre S, Tatangelo L, Bonafe L, Gualeni B, Romano A, Pecora F, Superti-Furga A*, et al.* (2005) *Hum Mol Genet* **14,** 859-871.

180. Kanda T, Yoshida Y, Izu Y, Nifuji A, Ezura Y, Nakashima K, & Noda M (2007) *J Cell Biochem*.

181. Stacey A, Bateman J, Choi T, Mascara T, Cole W, & Jaenisch R (1988) *Nature* **332,** 131-136.

182. Khillan JS, Olsen AS, Kontusaari S, Sokolov B, & Prockop DJ (1991) *J Biol Chem* **266,** 23373-23379.

183. Millington-Ward S, McMahon HP, & Farrar GJ (2005) *Trends Mol Med* **11,** 299-305.

184. Kratochwil K, Dziadek M, Lohler J, Harbers K, & Jaenisch R (1986) *Dev Biol* **117,** 596-606.

185. Kalajzic I, Terzic J, Rumboldt Z, Mack K, Naprta A, Ledgard F, Gronowicz G, Clark SH, & Rowe DW (2002) *Endocrinology* **143,** 1594-1601.

186. Tsang KY, Chan D, Cheslett D, Chan WC, So CL, Melhado IG, Chan TW, Kwan KM, Hunziker EB, Yamada Y*, et al.* (2007) *PLoS Biol* **5,** e44.

187. Fedarko NS, Vetter UK, Weinstein S, & Robey PG (1992) *J Cell Physiol* **151,** 215-227.

188. Whyte M (1999) in *Dynamics of bone and cartilage metabolism*, eds. Seibel M, Robins S, & Bilezikian J (Academic Press, London), pp. 127-142.

189. Rauch F, Travers R, Parfitt AM, & Glorieux FH (2000) *Bone* **26,** 581-589.

190. Hazenberg JG, Taylor D, & Lee TC (2007) *Osteoporos Int* **18,** 1-8.
191. Teitelbaum SL (2007) *Am J Pathol* **170,** 427-435.
192. Corsi A, Xu T, Chen XD, Boyde A, Liang J, Mankani M, Sommer B, Iozzo RV, Eichstetter I, Robey PG*, et al.* (2002) *J Bone Miner Res* **17,** 1180-1189.
193. Glorieux FH (2007) *Pediatrics* **119 Suppl 2,** S163-165.
194. Misof BM, Roschger P, Baldini T, Raggio CL, Zraick V, Root L, Boskey AL, Klaushofer K, Fratzl P, & Camacho NP (2005) *Bone* **36,** 150-158.
195. von Knoch F, Jaquiery C, Kowalsky M, Schaeren S, Alabre C, Martin I, Rubash HE, & Shanbhag AS (2005) *Biomaterials* **26,** 6941-6949.
196. Plotkin LI, Weinstein RS, Parfitt AM, Roberson PK, Manolagas SC, & Bellido T (1999) *J Clin Invest* **104,** 1363-1374.
197. Kirsch T, Nah HD, Demuth DR, Harrison G, Golub EE, Adams SL, & Pacifici M (1997) *Biochemistry* **36,** 3359-3367.
198. de Crombrugghe B, Lefebvre V, & Nakashima K (2001) *Curr Opin Cell Biol* **13,** 721-727.
199. Guo J, Chung UI, Yang D, Karsenty G, Bringhurst FR, & Kronenberg HM (2006) *Dev Biol* **292,** 116-128.
200. Bateman JF, Lamande SR, Dahl HH, Chan D, Mascara T, & Cole WG (1989) *J Biol Chem* **264,** 10960-10964.
201. Chessler SD, Wallis GA, & Byers PH (1993) *J Biol Chem* **268,** 18218-18225.
202. Pace JM, Kuslich CD, Willing MC, & Byers PH (2001) *J Med Genet* **38,** 443-449.
203. Bateman JF, Chan D, Mascara T, Rogers JG, & Cole WG (1986) *Biochem J* **240,** 699-708.
204. Malone JP, Alvares K, & Veis A (2005) *Biochemistry* **44,** 15269-15279.
205. Prockop DJ (1984) *Am J Hum Genet* **36,** 499-505.
206. Morike M, Schulz M, Brenner RE, Bushart GB, Teller WM, & Vetter U (1993) *J Cell Physiol* **157,** 439-444.
207. Jilka RL, Weinstein RS, Bellido T, Roberson P, Parfitt AM, & Manolagas SC (1999) *J Clin Invest* **104,** 439-446.
208. Pi M, Oakley RH, Gesty-Palmer D, Cruickshank RD, Spurney RF, Luttrell LM, & Quarles LD (2005) *Mol Endocrinol* **19,** 1078-1087.
209. Delahunty M & Bonifacino JS (1995) *Connect Tissue Res* **31,** 283-286.
210. Flynn GC, Pohl J, Flocco MT, & Rothman JE (1991) *Nature* **353,** 726-730.
211. Ripley CR & Bienkowski RS (1997) *Exp Cell Res* **236,** 147-154.
212. Kojima T, Miyaishi O, Saga S, Ishiguro N, Tsutsui Y, & Iwata H (1998) *J Pathol* **184,** 212-218.
213. Willing MC, Cohn DH, & Byers PH (1990) *J Clin Invest* **85,** 282-290.
214. Garneau NL, Wilusz J, & Wilusz CJ (2007) *Nat Rev Mol Cell Biol* **8,** 113-126.
215. Schafer ZT & Kornbluth S (2006) *Dev Cell* **10,** 549-561.
216. Krantic S, Mechawar N, Reix S, & Quirion R (2007) *Prog Neurobiol* **81,** 179-196.
217. Rathmell JC & Kornbluth S (2007) *Cell* **129,** 861-863.
218. McCullough KD, Martindale JL, Klotz LO, Aw TY, & Holbrook NJ (2001) *Mol Cell Biol* **21,** 1249-1259.
219. Noble B (2005) *Eur J Morphol* **42,** 91-98.
220. Zhao W, Byrne MH, Wang Y, & Krane SM (2000) *J Clin Invest* **106,** 941-949.
221. Sheng MH, Lau KH, Mohan S, Baylink DJ, & Wergedal JE (2006) *Calcif Tissue Int* **78,** 293-301.
222. McAllion SJ & Paterson CR (1996) *J Clin Pathol* **49,** 627-630.
223. Plotkin H (2004) *BMC Pediatr* **4,** 16.
224. Perez-Guzman C & Vargas MH (2006) *Med Hypotheses* **66,** 1227-1230.

225. Woo D, Kissela BM, Khoury JC, Sauerbeck LR, Haverbusch MA, Szaflarski JP, Gebel JM, Pancioli AM, Jauch EC, Schneider A, *et al.* (2004) *Stroke* **35,** 1360-1364.
226. Waterham HR (2002) *Clin Genet* **61,** 393-403.
227. Phillips CL, Pfeiffer BJ, Luger AM, & Franklin CL (2002) *Kidney Int* **62,** 383-391.
228. Yamaguchi M & Yamaguchi R (1986) *Biochem Pharmacol* **35,** 773-777.
229. Yamaguchi M & Ehara Y (1995) *Calcif Tissue Int* **57,** 218-223.
230. Lai YL & Yamaguchi M (2005) *Biol Pharm Bull* **28,** 2296-2301.
231. Prasad AS, Mantzoros CS, Beck FW, Hess JW, & Brewer GJ (1996) *Nutrition* **12,** 344-348.
232. Kurz D & Eyring EJ (1974) *Pediatrics* **54,** 56-61.
233. Smith JC, Makdani D, Hegar A, Rao D, & Douglass LW (1999) *J Am Coll Nutr* **18,** 213-222.
234. Treacy EP, Akerman BR, Chow LM, Youil R, Bibeau C, Lin J, Bruce AG, Knight M, Danks DM, Cashman JR, *et al.* (1998) *Hum Mol Genet* **7,** 839-845.
235. Vetter U, Maierhofer B, Muller M, Lang D, Teller WM, Brenner R, Frohneberg D, & Worsdorfer O (1989) *Eur J Pediatr* **149,** 184-187.
236. Wong RS, Follis FM, Shively BK, & Wernly JA (1995) *Ann Thorac Surg* **60,** 1439-1443.
237. Takken T, Terlingen HC, Helders PJ, Pruijs H, Van der Ent CK, & Engelbert RH (2004) *J Pediatr* **145,** 813-818.
238. Shroff RC & Shanahan CM (2007) *Semin Dial* **20,** 103-109.
239. Hui M & Tenenbaum HC (1998) *Anat Rec* **253,** 91-94.
240. de Souza RR (2002) *Biogerontology* **3,** 325-335.
241. Diez J, Gonzalez A, Lopez B, & Querejeta R (2005) *Nat Clin Pract Cardiovasc Med* **2,** 209-216.
242. McCormick RJ & Thomas DP (1998) *Basic Appl. Myol.* **8,** 143-150.
243. Widmann RF, Bitan FD, Laplaza FJ, Burke SW, DiMaio MF, & Schneider R (1999) *Spine* **24,** 1673-1678.
244. Reiser KM, Amigable MA, & Last JA (1992) *J Biol Chem* **267,** 24207-24216.
245. Hadley JC, Meek KM, & Malik NS (1998) *Glycoconj J* **15,** 835-840.
246. Aessopos A, Farmakis D, & Loukopoulos D (2002) *Blood* **99,** 30-35.
247. Whitby FG, Phillips JD, Hill CP, McCoubrey W, & Maines MD (2002) *J Mol Biol* **319,** 1199-1210.
248. Dailey TA, McManus JF, & Dailey HA (2002) *Cell Mol Biol (Noisy-le-grand)* **48,** 61-69.
249. Kim KI, Baek SH, Jeon YJ, Nishimori S, Suzuki T, Uchida S, Shimbara N, Saitoh H, Tanaka K, & Chung CH (2000) *J Biol Chem* **275,** 14102-14106.
250. Bailey D & O'Hare P (2004) *J Biol Chem* **279,** 692-703.
251. Mukhopadhyay D, Ayaydin F, Kolli N, Tan SH, Anan T, Kametaka A, Azuma Y, Wilkinson KD, & Dasso M (2006) *J Cell Biol* **174,** 939-949.
252. Muller J, Ritt DA, Copeland TD, & Morrison DK (2003) *Embo J* **22,** 4431-4442.
253. Goransson O, Deak M, Wullschleger S, Morrice NA, Prescott AR, & Alessi DR (2006) *J Cell Sci* **119,** 4059-4070.
254. Bustelo XR, Sauzeau V, & Berenjeno IM (2007) *Bioessays* **29,** 356-370.
255. Adini I, Rabinovitz I, Sun JF, Prendergast GC, & Benjamin LE (2003) *Genes Dev* **17,** 2721-2732.
256. Wang DA & Sebti SM (2005) *J Biol Chem* **280,** 19243-19249.
257. Jahner D & Hunter T (1991) *Mol Cell Biol* **11,** 3682-3690.
258. Fritz G & Kaina B (1997) *J Biol Chem* **272,** 30637-30644.
259. Makela TP, Hellsten E, Vesa J, Hirvonen H, Palotie A, Peltonen L, & Alitalo K (1995) *Oncogene* **11,** 2699-2704.

260. Kurochkin IV, Mizuno Y, Konagaya A, Sakaki Y, Schonbach C, & Okazaki Y (2007) *Embo J* **26,** 835-845.
261. Henry SP, Takanosu M, Boyd TC, Mayne PM, Eberspaecher H, Zhou W, de Crombrugghe B, Hook M, & Mayne R (2001) *J Biol Chem* **276,** 12212-12221.
262. Yamada S, Tomoeda M, Ozawa Y, Yoneda S, Terashima Y, Ikezawa K, Ikegawa S, Saito M, Toyosawa S, & Murakami S (2007) *J Biol Chem*.
263. Yamada S, Ozawa Y, Tomoeda M, Matoba R, Matsubara K, & Murakami S (2006) *J Dent Res* **85,** 447-451.
264. Plewnia G, Schulze K, Hunte C, Tampe R, & Koch J (2007) *J Mol Biol* **369,** 95-107.
265. Franz C, Askjaer P, Antonin W, Iglesias CL, Haselmann U, Schelder M, de Marco A, Wilm M, Antony C, & Mattaj IW (2005) *Embo J* **24,** 3519-3531.
266. Kiger AA, Gigliotti S, & Fuller MT (1999) *Genetics* **153,** 799-812.
267. Pereira R, Halford K, Sokolov BP, Khillan JS, & Prockop DJ (1994) *J Clin Invest* **93,** 1765-1769.
268. Kuznetsova NV, Forlino A, Cabral WA, Marini JC, & Leikin S (2004) *Matrix Biol* **23,** 101-112.
269. Carmeliet P & Tessier-Lavigne M (2005) *Nature* **436,** 193-200.
270. Gitler AD, Lu MM, & Epstein JA (2004) *Dev Cell* **7,** 107-116.
271. Torres-Vazquez J, Gitler AD, Fraser SD, Berk JD, Van NP, Fishman MC, Childs S, Epstein JA, & Weinstein BM (2004) *Dev Cell* **7,** 117-123.
272. Postlethwait JH (2006) *J Exp Zoolog B Mol Dev Evol*.
273. Michielse CB, Bhat M, Brady A, Jafrid H, van den Hurk JA, Raashid Y, Brunner HG, van Bokhoven H, & Padberg GW (2006) *Eur J Hum Genet* **14,** 1306-1312.
274. Huber AB, Kolodkin AL, Ginty DD, & Cloutier JF (2003) *Annu Rev Neurosci* **26,** 509-563.
275. Hilton MJ, Tu X, Cook J, Hu H, & Long F (2005) *Development* **132,** 4339-4351.
276. Docheva D, Hunziker EB, Fassler R, & Brandau O (2005) *Mol Cell Biol* **25,** 699-705.
277. Zelzer E, Mamluk R, Ferrara N, Johnson RS, Schipani E, & Olsen BR (2004) *Development* **131,** 2161-2171.
278. Sharif M, Whitehouse A, Sharman P, Perry M, & Adams M (2004) *Arthritis Rheum* **50,** 507-515.
279. Spector TD, Cicuttini F, Baker J, Loughlin J, & Hart D (1996) *Bmj* **312,** 940-943.
280. Helminen HJ, Saamanen AM, Salminen H, & Hyttinen MM (2002) *Rheumatology (Oxford)* **41,** 848-856.
281. Okuyama K, Hongo C, Fukushima R, Wu G, Narita H, Noguchi K, Tanaka Y, & Nishino N (2004) *Biopolymers* **76,** 367-377.
282. Kyte J & Doolittle RF (1982) *J Mol Biol* **157,** 105-132.
283. Hulmes DJ (2002) *J Struct Biol* **137,** 2-10.
284. Seeman E (2003) *J Appl Physiol* **95,** 2142-2151.
285. Pollard TD & Earnshaw WC (2002) *Cell biology* (W.B. Saunders Company).

7.   Lebenslauf

Thomas Stephen Lisse

19. Juni 1974	geboren in New York City, New York USA als Sohn von Stephen D. Lisse und Keiko Lisse, geb. Himeno
1988 –1992	Abitur an der Falls Church High School in Falls Church, Virginia USA
1992 – 1996	Studium der Biologie an der Purdue Universität, West Lafayette, Indiana USA
1997 – 2001	Wissenschaftliche Assistenzstelle am Institut für Neurodegenerative Krankheiten in der Neuropathologie der University of California San Francisco (UCSF), USA
2002 – 2004	Diplomarbeit am Institut für Zellbiologie und Immunologie der Universität Stuttgart zum Thema „Neuroprotektive Signale durch TNF in NMDAR vermittelter Excitotoxizität" unter Betreuung von Professor Dr. Klaus Pfizenmaier und Dr. Ulrich Eisel
2004 – 2007	Doktorarbeit am Institut für Experimentelle Genetik im GSF Forschungszentrum für Umwelt und Gesundheit in der Helmholtz-Gemeinschaft München-Neuherberg zum Thema „Identifizierung, Genkartierung, und Charakterisierung von ENU-induzierten mutanten Mauslinien für Knochenkrankheiten des Menschen" unter Betreuung von Professor Dr. Martin Hrabé de Angelis.
2008	Doktorprüfung an der Universität Stuttgart durch die Professoren Dr. Georg Sprenger, Dr. Klaus Pfizenmaier und Dr. Martin Hrabé de Angelis (Neuherberg).